

ABSTRACT

Title of dissertation: Characterization of Linear Electro-Optic Effect of Poled Organic Thin Films

Dong Hun Park
Doctor of Philosophy, 2008

Dissertation directed by: Professor Chi H. Lee
Department of Electrical and
Computer Engineering

The goal of this thesis is to re-evaluate both Teng-Man and attenuated total reflection (ATR) methods for measuring the linear electro-optic (EO) coefficients of poled organic thin films based on a multilayer structure containing a transparent conducting oxide (TCO) layer.

The linear EO properties are often characterized using the Teng-Man reflection method. However, it has been reported that experimental error can result from ignoring multiple reflections and that an accurate determination of the EO effect could be achieved only by a numerical calculation that applies anisotropic Fresnel equations to the multilayer structure. We present new closed-form expressions for analysis of Teng-Man measurements of the EO coefficients of poled polymer thin films. These expressions account for multiple reflection effects using a rigorous analysis of the multilayered structure for varying angles of incidence. The analysis based on plane waves is applicable to both transparent and absorptive films and takes into account the properties of the TCO electrode layer and buffer layers. Methods

for fitting data are presented and the error introduced by ignoring the TCO layer and multiple reflections is discussed. We also discuss the effect of Gaussian beam optics and the suitability of a thick z -cut LiNbO_3 crystal as a reference to validate the Teng-Man measurement.

Simply taking the metal electrode off the Teng-Man sample makes it feasible to use the ATR method using a metal-coated prism. This technique has the capability of measuring anisotropic indices of refraction along with film thicknesses. In addition, it enables measurement of r_{13} and r_{33} separately without an assumption for the ratio of r_{13} to r_{33} as required in the Teng-Man method. We have found that the ATR analysis based on a three-layer waveguide structure (air/film/substrate) can produce a large error especially when the film supports a single guided mode and the ATR analysis based on a multilayer structure containing a TCO layer gives you a more reliable estimation. We discuss the error introduced by using the three-layer waveguide structure and compare to using the multilayer structure.

Finally, we discuss the characterization of the optical property of TCO's using ellipsometric analysis, which is required for both the rigorous Teng-Man and ATR analysis. Representative experimental results showing that the result from the ATR method based on the multilayer structure shows a good agreement with that from the rigorous Teng-Man analysis are presented. We have measured a very high linear electro-optic coefficient ($r_{33} = 350 \text{ pm/V}$) from a NLO film (AJ-TTE-II, synthesized by Alex Jen's group at University of Washington) at 1310 nm wavelength, which is ~ 12 times higher than the best inorganic electro-optic crystal LiNbO_3 .

Characterization of Linear Electro-Optic Effect
of Poled Organic Thin Films

by

Dong Hun Park

Dissertation submitted to the Faculty of the Graduate School of the
University of Maryland, College Park in partial fulfillment
of the requirements for the degree of
Doctor of Philosophy
2008

Advisory Committee:
Professor Chi H. Lee, Chair/Advisor
Doctor Warren N. Herman, Co-advisor
Professor Julius Goldhar
Professor Martin Peckerar
Professor James R. Anderson

© Copyright by
Dong Hun Park
2008

DEDICATION

to my loving Soohyun,

Sora, Jena,

and parents.

ACKNOWLEDGMENTS

First of all, I would like to thank my advisor, Professor Emeritus Chi H. Lee for giving me a chance to join the Polymer Photonics Group at the Laboratory for Physical Sciences (LPS), where I stepped into the field of nonlinear optics for the first time in my life. I feel highly honored to work with him during my Ph.D. program. It has been a great pleasure to perform my research under his guidance while doing research.

The group leader of Polymer Photonic Group at LPS, Dr. Warren N. Herman is not only my co-advisor, but also a collaborator. I'm considerably indebted to him for giving me an invaluable opportunity to work on challenging and extremely interesting research projects over the past five years. He has also given me numerous ideas and corrected my thought process. Without his theoretical and experimental expertise, this thesis would not have been possible. As a project leader and researcher, he always strives to achieve his best. I am really eager to pursue his example, though I am sure I will not be able to catch up. I can say without a doubt that I have the best advisor it is possible to have!

Also, I'd like to thank Professor Julius Goldhar for agreeing to be one of the committee members in both the proposal examination and the thesis defense. His class ENEE790 was really helpful. Professors Martin Peckerar and James Anderson also accepted my request to serve on the committee with good grace. I cordially

appreciate their acceptance.

I'd like to thank Dr. Danilo Romero for answering my questions. He has always made himself available for helping others and giving a piece of advice. Whenever I've knocked on his door, he has always given me time although he looked busy doing something. It has been a pleasure to work with him and learn from such an extraordinary individual.

I'm indebted to Victor Yun for helping me with the best experimental setup and giving me a lot of ideas in making apparatus. The conversations with him were always witty and humorous. Through the conversations, I learned more American culture and history that I had never known. Also, I'd like to thank Dr. Yongzhang Leng for all the advices he gave about my research.

I have had the pleasure to work with Prof. Lee's group members: Dr. Weilou Cao, Dr. Junghwan Kim, Min Du, Yi-Hsing Peng. It has been a great time to work with LPS polymer group members: Profs. P.-T. Ho and John Fourkas, Dr. Mihaela Ballarotto, Tie Nan Ding, Dr. Wien Chen, Linjie Li, and Dr. George Kumi.

Many colleagues at LPS have enriched my graduate study and life in many ways. Arthur Liu was quite willing to do any favors that I asked. Ricardo Pizarro nicknamed me "Papa-Dong". Dyan Ali had heavy metal music on whenever I stopped by his lab. Konrad Aschenbach readily talked with me and corrected my English. Dr. Hanhee Baik liked to introduce me to her acquaintances around. Dr. Jonghee Lee always conversed with me outside while he was smoking (Please don't do that in winter!). Zaeill Kim had been handling a gigantic amount of experimental data (even until now), Dr. Taesoon Kwon helped me wash my car for free at her

cousin's car wash shop. Dr. Timothy Corrigan conversed freely with me, and David Park helped me make an experimental setup. I'd like to thank all of them.

I have been able to spend a wonderful time during my Ph.D study because of members of Korean Graduates in ECE and other departments : Dr. Junhyuck Yoo, Dr. Seung-Jong, Dr. Younggu Kim, Dr. Kejong Kim, Dr. Woocheol Jun, Subum Lee, Sangchul Song, Jusub Kim, Seokjin Kim, Jookyung Lee, Hojin Kee, Insuk Choi, Kwangsik Choi, Kyungjin Yoo, Minkyung Cho, Kwangho Park's and Dr. Wonsuk Jang's family, and so on. I will not forget all the extra activities such as tennis, baseball, hiking, picnic, potluck parties, sometimes drinking, small talk at Starbucks, and so on. They provided me with indispensable vitamins which made me keep up the studying.

I couldn't imagine myself beginning graduate study without Sam Kim, my high school alumnus. Five years ago, I retired from an IT company in LA and drove to Maryland with my wife for four days without a break (except three nights sleep) to start my graduate study. Initially, he provided a place to stay until I found a permanent place to stay. I know it burdened him and his wife very much. However they gave me a warm reception. I'd like to express my gratitude to him for his friendship and support.

I'd also like to acknowledge help and support from some of the staff members in ECE and LPS. Greg Latini for computer hardware support, Lisa Lucas for the cleanroom training and Vivian Lu for the financial services.

I'd like to acknowledge financial support from the Defense Advanced Research Projects Agency (DARPA), Army Research Lab (ARL), and Laboratory for Phys-

ical Sciences (LPS). I'd like to acknowledge research collaboration with Dr. G. A. Lindsay's group at Naval Air Warfare Center Weapons Division, Prof. Mike Hayden's group at University of Maryland, Baltimore County, and Prof. Alex Jen's group at University of Washington, for all the works related to this thesis.

Most of all, I am deeply indebted to my family; parents, parents-in-law, brothers, and sisters, for their countless love and support over the past five years. I would like to give a special thanks to my loving Soohyun for her moral support and unceasing sacrifice.

Thank God.

Dong Hun Park, 2008

Table of Contents

List of Tables	x
List of Figures	xi
List of Abbreviations	xix
1 Introduction	1
1.1 Motivation and contributions	1
1.2 Review of second-order nonlinear polymers	5
1.2.1 Linear susceptibility and second-order nonlinearity	5
1.2.2 Optical processes in orientationally ordered materials	12
1.2.3 Polymer systems	19
1.2.4 Chromophore orientation techniques	22
1.2.5 Applications of second-order nonlinear polymers	24
1.2.6 Characterization methods	27
1.3 Convention	28
1.4 Scope of thesis	30
2 Teng-Man Method	33
2.1 Introduction	33
2.1.1 Characterization methods	33
2.1.2 Teng-Man method	34
2.1.3 Outline of this chapter	36
2.2 Theory and analysis	38
2.2.1 Expression for variation of index of refraction	38
2.2.2 General expressions	40
2.2.3 Simple model	47

2.2.4	Rigorous model	51
2.2.5	Data analysis	53
2.2.6	Uncertainty and sensitivity	55
2.2.7	Results	56
2.3	Thick z -cut LiNbO ₃ crystal for validation of Teng-Man method	70
2.3.1	Rigorous analysis	70
2.3.2	Results	72
2.4	Gaussian beam optics	75
2.4.1	Theory	75
2.4.2	Results	76
3	Attenuated Total Reflection Method	79
3.1	Introduction	79
3.1.1	Prism coupling technique	79
3.1.2	ATR for EO measurement	80
3.1.3	Outline of the chapter	81
3.2	Theory and analysis	83
3.2.1	Principle of ATR	83
3.2.2	Asymmetric and anisotropic slab waveguides	88
3.2.3	Data analysis	97
3.2.4	Results	98
4	Measurement	110
4.1	Introduction	110
4.1.1	Measurement procedures	110
4.1.2	Outline of the chapter	111
4.2	Characterization of transparent conducting oxides	112
4.2.1	Transparent conducting oxides	112

4.2.2	Spectroscopic ellipsometry for characterization of TCO	114
4.3	Experimental setup	127
4.3.1	Electrode contact poling setup	127
4.3.2	Teng-Man and ATR setup	129
4.4	EO measurements	131
4.4.1	AJ302	131
4.4.2	AJ404L	136
4.4.3	AJLS102	145
4.4.4	AJ-TTE-II	153
5	Conclusions	155
5.1	Summary	155
5.2	Research directions	159
A	$\delta\beta$ and H Functions in Teng-Man Method	161
A.1	Variation of the propagation constants inside the NLO film	161
A.2	H functions in the rigorous model	162
B	Error Estimator	165
B.1	Teng-Man error estimator in MATLAB TM	165
B.2	Java Teng-Man error estimator	169
	Bibliography	171

List of Tables

4.1	Summary of EO coefficients of AJLS102 NLO film.	153
5.1	Summary of EO coefficients of four NLO films and LiNbO ₃ at 1310 nm.	158

List of Figures

1.1	The j , k , and l axes represent the laboratory coordinates, while the J , K , and L the molecular system coordinates.	14
1.2	Simplified schematics of chemical structures of (a) guest host, (b) side chain, (c) main chain, and (d) crosslinked polymer system.	20
1.3	Schematics of (a) Corona and (b) electrode contact poling.	23
1.4	Schematic of (a) Mach-Zehnder electro-optic modulator and (b) quasi phase matching second harmonic generation.	26
1.5	The trajectory of the electric field in the plane wave propagating in the z -direction represents the right-handed circularly polarized (RCP) light.	29
2.1	Schematic of the experimental Teng-Man setup. L is laser, P polarizer, A aperture, S slit, SBC Soleil-Babinet Compensator, and PD photodetector.	41
2.2	The optical bias curve and modulated intensity obtained as a function of SBC retardation setting x for a representative set of experimental data on a film. Points 1, 2, 3, and 4 correspond to compensator settings such that $\Psi_{sp} + \Omega = \pi/2, 3\pi/2, 0$, and π , respectively.	44
2.3	Multilayered structures in a simple model (a) and a rigorous model (b). For simplicity, subscripts s and p in the reflection coefficients are omitted in (b).	49

2.4 Error percentage plot for varying film thickness when the refractive indices of film and TCO are matched with glass ($n = 1.5$) at $1.3 \mu\text{m}$ wavelength. The positive and negative envelopes are proportional to $\pm 1/d_4$ with a negative offset. 59

2.5 Optical properties ($n + i\kappa$) of (solid) a representative ITO (Abrisa[®]) measured by ellipsometry and (dashed) a representative polymer film selected for the simulation. (real part : black, imaginary part : red). . 61

2.6 Error plots by varying the thickness of the film for fixed indices of refraction of ITO and the film and two thicknesses of ITO, 100 nm (a-d) and 50 nm (e-h) at various wavelengths and 45° angle of incidence under assumption of $\gamma = 1/3$. For plots (a) and (e), $s_{33}/r_{33} = 1$ (black solid), and $s_{33}/r_{33} = 2$ (red dashed). For the wavelengths other than $0.8 \mu\text{m}$, values of s_{33}/r_{33} between 0 and 0.1 produce curves that are indistinguishable on this scale. For (a) and (e), the errors approach -107% and -110%, respectively. For (b), (f), (c), (g), (d), and (h), the error extremes are -18% to 12%, -15% to 10%, -86% to 38%, -40% to 25%, -80% to 350%, and -37% to 63%, respectively. 62

2.7 Error contour plots at (a) $\lambda = 0.8 \mu\text{m}$ and $s_{33}/r_{33} = 1$ (b) $\lambda = 1.3 \mu\text{m}$ and $s_{33}/r_{33} = 0.1$ with thickness of ITO = 100 nm, 45° angle of incidence, and $\gamma = 1/3$. Each contour plot (a) and (b) shows asymptotic and cyclic behaviors with thickness of film irrespective of index of refraction of film, respectively. 64

2.8	EO coefficients r_{33} calculated by the simple model at various wavelengths and angles of incidence using thickness of film and ITO, 1.4 μm and 100 nm, respectively. EO coefficient $r_{33} = 100 \text{ pm/V}$ was used for the simulation. The ratios s_{33}/r_{33} are 2 at 0.8 μm and 0.1 μm at the other wavelength. Insets in (a) and (b) show the optical properties of ITO selected for the simulation. The crossover points of n and κ of ITO are around 1.54 and 1.92 μm in (a) and (b), respectively.	65
2.9	(a) $\delta\Psi_{sp}$ and (b) $\delta B/B$ versus angle of incidence at wavelengths 1.3 and 1.55 μm . The ratio $s_{33}/r_{33} = 0.1$ and film thickness = 1.4 μm were used at both wavelengths for the ITO properties shown in Fig. 2.5.	66
2.10	Representative error profiles in anisotropic case using 150 nm thick ITO at 1.3 μm wavelength. Red, green, and blue lines are for the birefringence $\Delta n \equiv n_e - n_o$ of 0, 0.03, 0.06, and 0.09, respectively.	67
2.11	Representative error percentage in anisotropic case at 1.3 μm wavelength. The error shows a beating behavior unlike asymptotic one as shown in the isotropic case.	68
2.12	Representative $\delta\Psi_{sp}$ with three different film thicknesses at 1.3 μm wavelength. Red, green, and blue lines are for the film thickness of 1, 10, 50 μm , respectively.	69
2.13	Smith's technique is applied to air/TCO/LiNbO ₃ interface which can be considered as a single interface.	70
2.14	Solid and dashed lines are the ratios of $ \text{Im}(\delta C/C) $ to $ 2(\delta\beta_{3s} - \delta\beta_{3p})d_3 $ when the LiNbO ₃ is 0.5 mm and 1 μm thick, respectively.	72
2.15	Simplified multilayer structure using a virtual interface.	76

2.16	Calculated reflectances of the s (red)- and p (blue)- wave of a Gaussian beam versus beam width at 45° angle of incidence.	77
3.1	The prism coupling technique for coupling light in and out.	80
3.2	Schematic of the experimental ATR setup.	84
3.3	Reflectivity versus N . A DC voltage V generates a slight shift of reflectivity curve.	86
3.4	Schematic of the three-layer slab waveguide.	88
3.5	Schematic of the multilayer slab waveguide.	95
3.6	Flow chart showing the procedures to calculate the relative errors of r_{13} and r_{33} from both three-layer and four-layer waveguide models. . .	99
3.7	Plots of error and $\partial N^p/\partial n_e$ by varying the film thickness for selected index of refraction of TCO and the film and two TCO thickness, 45 nm (a-d) and 150 nm (e-h) at wavelength of 1310 nm. For plots (a) and (e), black and red lines show errors in the estimation of n_o for the three- and the four-layer waveguide model, respectively. Green dashed and solid lines show errors in the estimation of d_f from the three- and the four-layer waveguide model, respectively. In (b) and (f), $\partial N^p/\partial n_e$ is plotted. For plots (c) and (g), dashed line shows error in the estimation of r_{13} from the three-layer waveguide model and solid lines from the four-layer waveguide model. For plots (d) and (h), dashed line shows error in the estimation of r_{33} from the three-layer waveguide model and solid lines from the four-layer waveguide model.	102

3.8 Plots of error and $\partial N^p/\partial n_e$ by varying the film thickness for selected index of refraction of TCO and the film and two TCO thickness, 45 nm (a-d) and 150 nm (e-h) at wavelength of 1550 nm. For plots (a) and (e), black and red lines show errors in the estimation of n_o for the three- and the four-layer waveguide model, respectively. Green dashed and solid lines show errors in the estimation of d_f from the three- and the four-layer waveguide model, respectively. In (b) and (f), $\partial N^p/\partial n_e$ is plotted. For plots (c) and (g), dashed line shows error in the estimation of r_{13} from the three-layer waveguide model and solid lines from the four-layer waveguide model. For plots (d) and (h), dashed line shows error in the estimation of r_{33} from the three-layer waveguide model and solid lines from the four-layer waveguide model. 103

3.9 Error percentages from the ATR based on the three-layer and four-layer waveguide models and the simple Teng-Man method at 45° . Plots of error by varying the film thickness for selected index of refraction of TCO and the film and two TCO thickness, 45 nm (a,b) and 150 nm (c,d) at wavelength of 1310 nm (a,c) and 1550 nm (b,d). Red dashed line shows error in the estimation of r_{33} from the three-layer waveguide model and red solid lines from the four-layer waveguide model. Black solid line shows error from the simple Teng-Man method. Shaded region represents a single mode film. 106

3.10	Plots of $\partial N^p/\partial n_e$ by varying the film thickness for selected indices of refraction and thickness of TCO and the film at wavelength of 1310 nm. Solid and dashed lines are $\partial N^p/\partial n_e$'s calculated by using four-layer and three-layer waveguide models, respectively. A, B, C and D represent the regions of film thickness where the film supports single, two, three, and four or more than four guided mode/modes, respectively.	109
4.1	A representative optical property of ITO manufactured by Abrisa®. The inset shows the transmission data (red) at normal incidence. It is well matched with projected transmission curve (black).	117
4.2	A representative optical property of ITO manufactured by Thin Film Devices™. A graded layer model was used to obtain a complex refractive index. The n and κ of top and bottom layers are shown. . .	119
4.3	Graded indices of refraction at 1310 nm. The solid line is the real part n and the dotted one the imaginary part κ of the complex index of refraction.	121
4.4	Transmittance at normal incidence. The Red line was obtained by UV-VIS spectroscopic scan by Varian® and the black one is a projected transmittance.	123
4.5	Optical property ($n + i\kappa$) of a ZnO measured by spectroscopic ellipsometry. Black solid and red dotted lines are the real and imaginary parts of the complex refractive index, respectively. Inset shows UV-VIS-NIR transmission spectrum. Black and red lines are projected and experimental transmission, respectively.	125

4.6	Electrode contact poling setup.	128
4.7	(a) Schematic of multi-angle Teng-Man setup and (b) commercial Metricon TM prism coupler 2010.	129
4.8	Molecular structures of AJC168 and AJC146.	132
4.9	Fits (dashed lines) to the rigorous model of $\delta\Psi_{sp}$, $\delta B/B$, $\tan \Phi$, and Ψ_{sp} extracted by curve fitting to Eqs. 2.9 and 2.15. In (a), both possible values of $\tan \Phi$ resulting from A/B using Eq. 2.14 are shown.	134
4.10	Complex index of refraction of six ITO's on glass substrate measured by ellipsometric technique.	138
4.11	Experimental data (triangle, square) of (a), (b), (c), and (d) show good agreement with numerical fits (solid, dashed) at 1310 nm and 1550 nm, respectively.	140
4.12	The r_{33} calculated by simple Teng-Man analysis at each angle of in- cidence at 1310 nm (open circle) and 1550 nm (triangle).	142
4.13	Dispersion characteristics of r_{33} versus wavelength. Triangles are r_{33} calculated by the rigorous analysis at 1310 nm and 1550 nm and solid line is obtained by a two-level model.	144
4.14	Optical property ($n + i\kappa$) of a ITO (Thin Film Device TM) measured by spectroscopic ellipsometry. Inset shows UV-VIS-NIR transmission spectrum.	146
4.15	R_{dc} (black) and R_m (red) versus N at 1550 nm in (a) TE and (b) TM modes. The peak voltage 1 Volt with an AC frequency of 200 Hz was applied to the NLO film to get the modulated signal R_m	148

4.16 (a) Measured $\delta\Psi_{sp}$ and $\delta B/B$ versus angle of incidence. Dashed and short dash lines are numerical fit to $\delta\Psi_{sp}$ and $\delta B/B$. (b) EO coefficients r_{33} calculated by the simple model (triangle) and the rigorous model (circle) at discrete angle of incidence. The r_{33} by the rigorous model at each angle are well aligned with fitted r_{33} 150

4.17 The estimate of error from the simple Teng-Man analysis generated using Java Teng-Man estimator. 152

4.18 (a) Measured $\delta\Psi_{sp}$ and $\delta B/B$ versus angle of incidence. Dashed and short dash lines are numerical fit to $\delta\Psi_{sp}$ and $\delta B/B$. (b) EO coefficients r_{33} calculated by the simple model (triangle) and the rigorous model (circle) at discrete angle of incidence. The r_{33} 's by the rigorous model at each angle are well aligned with fitted r_{33} 154

B.1 Snap shot of Java Teng-Man error estimator. 170

List of Abbreviations

AC	Alternation Current
ATR	Attenuated Total Reflection
DC	Direct Current
EO	Electro-Optic
FP	Fabry-Perot
GH	Guest Host
ITO	Indium Tin Oxide
LEO	Linear Electro-Optic
LHC	Left-Handed Circular
MC	Main Chain
MSR	Multilayer Stack Reflectivity
MSRM	Multilayer Stack Reflectivity Model
MZI	Mach-Zehnder Interferometer
NIR	Near Infrared
NLO	Nonlinear Optic
NLOP	Nonlinear Optic Polymer
OBC	Optical Bias Curve
OGM	Oriented Gas Model
OP amp	Operational amplifier
PEC	Perfect Electric Conductor
RHC	Right-Handed Circular
SBC	Soleil-Babinet Compensator
SC	Side Chain
SHG	Second Harmonic Generation
SVD	Singular Value Decomposition

T_g	glass transition temperature
TCO	Transparent Conducting Oxide
TE	Transverse Electric
TM	Transverse Magnetic
VASE	Variable Angle Spectroscopic Ellipsometry
WGM	Waveguide Model
XL	Crosslink

INTRODUCTION

1.1 Motivation and contributions

Organic molecules have attracted great interest for their potential applications in nonlinear optical (NLO) devices [1, 2, 3]. In particular, poled polymers based on second-order nonlinearity have been widely studied because they are a class of photonic material that could substitute for inorganic nonlinear crystals in high-speed optical communication and signal processing. Although poled polymers can have disadvantages such as thermal instability (depending on glass transition temperature), their interest is motivated by the following advantages:

- Large NLO response - much higher than r_{33} of LiNbO_3 [4, 5]
- Fast optical response - large bandwidth [6, 7]
- Low absorption loss at telecommunication wavelength [8]
- Ease of processing - conventional photolithography [9]
- Cost effectiveness [10]
- Possibility to change NLO properties by molecular engineering approach [4, 11].

Since the first poled NLO polymers were reported [12], research has been carried out on the development of new materials, the characterization of nonlinear

properties such as linear electro-optic (LEO) effect, THz generation, second harmonic generation (SHG), etc., and their applications to practical devices such as a modulators, resonators, polarization controllers, and so on. A macroscopic second-order NLO response requires orientation of chromophores, which can be achieved by electric field poling. Many researchers have been striving to synthesize polymeric EO materials and chromophores that will exhibit high nonlinearity in a poled polymer thin film. Therefore, a reliable and simple method for characterizing EO effect is indispensable to those who are extensively working on new material development. The electro-optic (EO) properties are often characterized using the reflection method introduced by Teng and Man (Teng-Man) [13] as well as Schildkraut [14] because it is simple and quick. The vast majority of quoted values of the electro-optic coefficient that are obtained from Teng-Man measurements result from a simplified analysis of the data that assumes the transparent conducting oxide (TCO) is perfectly transparent and the gold is perfectly reflective. However, it has been reported that experimental error can result from ignoring the reflection off the substrate-film interface and that an accurate determination of the EO coefficient could be achieved only by a numerical calculation that applies anisotropic Fresnel equations to the stratified layers containing the nonlinear poled polymer [13, 14, 15, 16, 17]. This limitation of the simple analysis in the Teng-Man reflection method motivates us to develop a new closed-form expressions for the analysis of multi-angle Teng-Man data including absorption of both the film and TCO layers. These expressions account for multiple reflection effects using a rigorous analysis of the multilayered structure for varying angles of incidence. We have also developed a stand-alone

software program in Java language for the estimation of error resulting from the simple Teng-Man method to offer convenience to those who want to estimate an error without any dependency on commercial numerical software such as MATLABTM and Mathematica.

A thick z -cut LiNbO₃ has been often used to validate a Teng-Man setup since Shuto and Amano presented that the EO coefficients of 0.5 mm thick z -cut LiNbO₃ measured by the simple Teng-Man method are in an excellent agreement with the known values [18]. Based on the rigorous Teng-Man analysis, we have examined the suitability of using a thick z -cut LiNbO₃ to validate a Teng-Man setup for measuring EO coefficients of poled polymer thin films.

We needed another characterization method that allows us to verify the rigorous Teng-Man method and that facilitates EO measurement because the rigorous Teng-Man method requires a long time to obtain multi-angle Teng-Man data and to analyze them numerically based on the multiple reflections in a multilayer structure. The attenuated total reflection (ATR) is another measurement method that can be applied to Teng-Man samples. Simply taking the metal electrode off the Teng-Man sample makes it feasible to use the ATR method using a metal-coated high index prism. This has great advantages over the Teng-Man method such as the measurement of anisotropic indices of refraction and thickness of the NLO film, the separate measurement of r_{13} and r_{33} , and so on. However, we have found that a measured film thickness based on a three-layer waveguide structure (air/film/glass) can introduce an error because of ignoring TCO layer. The ATR analysis based on a multilayer structure containing a TCO layer gives a more reliable EO estimation

than using a three-layer waveguide structure, especially when the film supports only a single guided mode. We recommend that the ATR analysis should be based on a multilayer structure containing a transparent conducting electrode layer for a more accurate determination of the linear EO coefficient.

The characterization of the optical properties of a TCO layer is required for both the rigorous Teng-Man and ATR analysis. For some cases, TCO is difficult to characterize because it displays a complicated graded microstructure, resulting in optical properties that can vary widely with deposition conditions and post-deposition processing. We use both single and graded multilayer models to characterize the optical property of TCO's using ellipsometric analysis. Our experimental results have shown that the result from the ATR method based on the multilayer structure shows a good agreement with that from the rigorous Teng-Man analysis. Finally, a very high linear electro-optic coefficient ($r_{33} = 350$ pm/V) has been measured from a NLO film (AJ-TTE-II) at 1310 nm wavelength, which is ~ 12 times higher than the best inorganic electro-optic crystal LiNbO_3 . This material was synthesized by Alex Jen and coworkers at the University of Washington.

Through this thesis, we discuss

- the development of the rigorous Teng-Man analysis for an accurate measurement
- the determination of the suitability of using thick z -cut LiNbO_3 to validate a Teng-Man setup
- the development of a stand-alone Java Teng-Man error estimator.
- the re-evaluation of the ATR analysis based on a multilayer structure

1.2 Review of second-order nonlinear polymers

1.2.1 Linear susceptibility and second-order nonlinearity

Polarization vector

In nonlinear optics, the macroscopic polarization vector can be expressed as a power series in the electric field in the form [19]

$$P_j = P_j^{(0)} + P_j^{(1)} + P_j^{(2)} + P_j^{(3)} + \dots, \quad (1.1)$$

where the subscript j represents a coordinate index ($j = 1, 2, 3$) in the laboratory frame. The first two terms are related to the spontaneous polarization and linear optical effects, respectively. The next higher order terms are related to the nonlinear optical effect. The third term is the second-order nonlinear effect that we are interested in. Assuming the medium is time invariant, the most general form of the polarization vector is, in the time domain, [19, 20]

$$\begin{aligned} P_j(t) &= P_j^{(0)}(t) \\ &+ \epsilon_o \int_{-\infty}^{\infty} \chi_{jk}^{(1)}(\tau) E_k(t - \tau) d\tau \\ &+ \epsilon_o \int_{-\infty}^{\infty} d\tau_1 \int_{-\infty}^{\infty} d\tau_2 \chi_{jkl}^{(2)}(\tau_1, \tau_2) E_k(t - \tau_1) E_l(t - \tau_2) \\ &+ \dots \end{aligned} \quad (1.2)$$

or

$$\begin{aligned}
P_j(t) &= P_j^{(0)}(t) \\
&+ \epsilon_o \int_{-\infty}^{\infty} \chi_{jk}^{(1)}(\omega) \hat{E}_k(\omega) e^{-i\omega t} d\omega \\
&+ \epsilon_o \int_{-\infty}^{\infty} d\omega_1 \int_{-\infty}^{\infty} d\omega_2 \chi_{jkl}^{(2)}(\omega_1, \omega_2) \hat{E}_k(\omega_1) \hat{E}_l(\omega_2) e^{-i(\omega_1+\omega_2)t} \\
&+ \dots,
\end{aligned} \tag{1.3}$$

where

$$\chi_{jk}^{(1)}(\omega) = \int_{-\infty}^{\infty} \chi_{jk}^{(1)}(\tau) e^{i\omega\tau} d\tau, \tag{1.4}$$

$$\chi_{jkl}^{(2)}(\omega_1, \omega_2) = \int_{-\infty}^{\infty} d\tau_1 \int_{-\infty}^{\infty} d\tau_2 \chi_{jkl}^{(2)}(\tau_1, \tau_2) e^{i(\omega_1\tau_1 + \omega_2\tau_2)}, \tag{1.5}$$

and the electric field $\hat{E}(\omega)$ in the frequency domain is given as

$$\hat{E}(\omega) = \frac{1}{2\pi} \int_{-\infty}^{\infty} E(t) e^{i\omega t} dt. \tag{1.6}$$

Here, we use the *Einstein* summation notation in the product of $\chi \hat{E}$ for simplicity.

From Eq. 1.2, we note that the polarization vector $P_j(t)$ is the convolution of the susceptibility and electric field. The $\epsilon_o \chi$ is the impulse response of the medium. By

Fourier transform, we have

$$\begin{aligned}
\hat{P}_j(\omega) &= \hat{P}_j^{(0)}(\omega) \\
&+ \epsilon_o \int_{-\infty}^{\infty} d\omega_1 \chi_{jk}^{(1)}(\omega_1) \hat{E}_k(\omega_1) \delta(\omega - \omega_1) \\
&+ \epsilon_o \int_{-\infty}^{\infty} d\omega_1 \int_{-\infty}^{\infty} d\omega_2 \chi_{jkl}^{(2)}(\omega_1, \omega_2) \hat{E}_k(\omega_1) \hat{E}_l(\omega_2) \delta(\omega - \omega_1 - \omega_2) \\
&+ \dots
\end{aligned} \tag{1.7}$$

Linear susceptibility

Assuming that the polarization response of the material is instantaneous, that is,

$\chi_{jk}^{(1)}(t) = \chi_{jk}^{(1)} \delta(t)$, $\chi_{jkl}^{(2)}(t_1, t_2) = \chi_{jkl}^{(2)} \delta(t_1, t_2)$, etc, Eq. 1.1 is rewritten as

$$P_j(t) = P_j^{(0)}(t) + \epsilon_o \chi_{jk}^{(1)} E_j(t) + \epsilon_o \chi_{jkl}^{(2)} E_j(t) E_k(t) + \dots, \tag{1.8}$$

which one might be familiar with. From basic electro-magnetic (EM) theory, we know

$$P_j^{(1)} = \epsilon_o \chi_{jk}^{(1)} E_k, \tag{1.9}$$

where χ_{jk} is the second-order. Equation 1.9 is equivalent to

$$\begin{pmatrix} P_x \\ P_y \\ P_z \end{pmatrix} = \epsilon_o \begin{pmatrix} \chi_{xx} & \chi_{xy} & \chi_{xz} \\ \chi_{yx} & \chi_{yy} & \chi_{yz} \\ \chi_{zx} & \chi_{zy} & \chi_{zz} \end{pmatrix} \begin{pmatrix} E_x \\ E_y \\ E_z \end{pmatrix}. \tag{1.10}$$

Second-order nonlinearity

From the second-order polarization vector terms in Eqs. 1.2 and 1.3, we note that the last two subscripts k and l in the expression of χ_{jkl} , are interchangeable. This is called intrinsic permutation symmetry¹. So, the number of independent elements in $\chi_{jkl}^{(2)}$ can be decreased from 27 to 18 and based on other symmetries some of these 18 elements are equivalent. The contracted form is given as

$$d_{j,kl} = \frac{1}{2}\chi_{j,kl}^{(2)} = d_{ju} = \begin{pmatrix} d_{11} & d_{12} & d_{13} & d_{14} & d_{15} & d_{16} \\ d_{21} & d_{22} & d_{23} & d_{24} & d_{25} & d_{26} \\ d_{31} & d_{32} & d_{33} & d_{34} & d_{35} & d_{36} \end{pmatrix}, \quad (1.11)$$

where the relation between kl and u is given as

$$\begin{array}{rcccccc} kl & = & 11 & 22 & 33 & 23, 32 & 13, 31 & 12, 21 \\ & & & & & & & \cdot \\ u & = & 1 & 2 & 3 & 4 & 5 & 6 \end{array}$$

Electric fields of monochromatic waves can be expressed as

$$E(t) = \frac{1}{2} \sum_{\omega_n > 0} [E(\omega_n)e^{-i\omega_n t} + E^*(\omega_n)e^{i\omega_n t}] \quad (1.12)$$

or

$$\hat{E}(\omega) = \frac{1}{2} \sum_{\omega_n > 0} [E(\omega_n)\delta(\omega - \omega_n) + E^*(\omega_n)\delta(\omega + \omega_n)]. \quad (1.13)$$

¹This is also valid in the higher order susceptibility.

Substituting Eq. 1.13 into Eq. 1.7 gives²

$$P_j^{(2)} = \frac{1}{4} \sum_{\omega_m > 0} \sum_{\omega_n > 0} [\chi_{jkl}(\omega_m, \omega_n) E_k(\omega_m) E_l(\omega_n) e^{-i(\omega_m + \omega_n)t} \quad (1.14)$$

$$+ \chi_{jkl}(\omega_m, -\omega_n) E_k(\omega_m) E_l^*(\omega_n) e^{-i(\omega_m - \omega_n)t} \quad (1.15)$$

$$+ \chi_{jkl}(-\omega_m, \omega_n) E_k^*(\omega_m) E_l(\omega_n) e^{i(\omega_m - \omega_n)t} \quad (1.16)$$

$$+ \chi_{jkl}(-\omega_m, -\omega_n) E_k^*(\omega_m) E_l^*(\omega_n) e^{i(\omega_m + \omega_n)t}]. \quad (1.17)$$

Suppose we have only two monochromatic waves given as

$$\hat{E}_j(\omega) = \frac{1}{2} E_j(\omega_1) \delta(\omega - \omega_1) + \frac{1}{2} E_j(\omega_2) \delta(\omega - \omega_2), \quad (1.18)$$

then, we have different kinds of nonlinear effects in the form

$$\left\{ \begin{array}{ll} \chi^{(2)}(-(\omega_1 + \omega_2); \omega_1, \omega_2) & \text{Sum frequency generation} \\ \chi^{(2)}(-2\omega_1; \omega_1, \omega_1) & \text{Second harmonic generation} \\ \chi^{(2)}(-(\omega_1 - \omega_2); \omega_1, -\omega_2) & \text{Difference frequency generation} \\ \chi^{(2)}(0; \omega_1, -\omega_1) & \text{Optical rectification} \\ \chi^{(2)}(-\omega_1; \omega_1, 0) & \text{Linear electro-optic effect or Pockel's effect,} \end{array} \right.$$

where the notation $\chi^{(2)}(-\omega_p; \omega_m, \omega_n)$, $\omega_p = \omega_m + \omega_n$ is used.

Now, we investigate the linear electro-optic effect, $\chi^{(2)}(-\omega_1; \omega_1, 0)$, in more detail. When a DC electric field parallel to the l -direction is applied to the sample,

²The number of subscript letters in the expression of χ also indicate the order of nonlinearity as shown in the superscript. Henceforth, either subscript or superscript can be used for simplicity.

the first two polarization terms are

$$P_j = \epsilon_o \{ \chi_{jk}(-\omega; \omega) E_k(\omega) + 2\chi_{jkl}(-\omega; \omega, 0) E_k(\omega) E_l(0) \}. \quad (1.19)$$

Using $\bar{\mathbf{D}} = \epsilon_o \bar{\mathbf{E}} + \bar{\mathbf{P}}$, the effective dielectric tensor can be defined by

$$D_j = \epsilon_o \{ \delta_{jk} + \chi_{jk}(-\omega; \omega) + 2\chi_{jkl}(-\omega; \omega, 0) E_l(0) \} E_k(\omega) \quad (1.20)$$

$$= \epsilon_o \{ \delta_{jk} + \chi_{jk}(-\omega; \omega) + \delta\chi_{jk} \} E_k(\omega) \equiv \epsilon_{jk}^{\text{eff}} E_k^\omega. \quad (1.21)$$

The electro-optic effect can be defined by using the electric impermeability $B \equiv 1/\epsilon_r$ induced by an electric field in the form

$$\Delta B_{jk} = B_{jk}(E) - B_{jk}(0) = \left[\frac{1}{\epsilon_r(E)} \right]_{jk} - \left[\frac{1}{\epsilon_r(0)} \right]_{jk} \equiv r_{jk,l} E_l(0), \quad (1.22)$$

where $r_{jk,l}$ is the linear electro-optic or Pockels coefficient. From Eqs. 1.21 and 1.22, we can derive

$$B_{jk}(0) + \Delta B_{jk} = (\delta_{jk} + \chi_{jk}(-\omega; \omega) + \delta\chi_{jk})^{-1} \quad (1.23)$$

and equivalently,

$$\delta_{jk} = \delta_{jk} + \Delta B_{jk} B_{jk}(0)^{-1} + B_{jk}(0) \delta\chi_{jk} + \Delta B_{jk} \delta\chi_{jk}, \quad (1.24)$$

where $B_{jk}(0)^{-1} = \delta_{jk} + \chi_{jk}$. Ignoring the last term in Eq. 1.24 and assuming $B(0)$

is diagonal³, we can obtain

$$\Delta B_{jk} = -B_{jm}(0)\delta\chi_{mn}B_{nk}(0) \quad (1.25)$$

$$= -2B_{jm}(0)\chi_{mnl}(-\omega; \omega, 0)E_l(0)B_{nk}(0) \quad (1.26)$$

$$= \frac{-2\chi_{jkl}(-\omega; \omega, 0)E_l(0)}{n_j^2 n_k^2} \quad (1.27)$$

$$= r_{jkl}E_l(0). \quad (1.28)$$

r_{jkl} is symmetric with respect to the first two indices and can be written in reduced tensor notation, r_{ul} , as described previously for the d_{ju} coefficient. In contracted notation, the linear electro-optic coefficient is

$$r_{ul} = \begin{pmatrix} r_{11} & r_{12} & r_{13} \\ r_{21} & r_{22} & r_{23} \\ r_{31} & r_{32} & r_{33} \\ r_{41} & r_{42} & r_{43} \\ r_{51} & r_{52} & r_{53} \\ r_{61} & r_{62} & r_{63} \end{pmatrix}. \quad (1.29)$$

A poled organic thin film prepared by spin coating belongs to the point-group symmetry ∞mm (space group $C_{\infty v}$) [21]. Two independent electro-optic tensor elements

³Note that first rank tensor B_{jk} or ϵ_{jk} can be diagonalized by proper choice of a coordinate system.

exist in the form

$$r_{ul} = \begin{pmatrix} 0 & 0 & r_{13} \\ 0 & 0 & r_{13} \\ 0 & 0 & r_{33} \\ 0 & r_{13} & 0 \\ r_{13} & 0 & 0 \\ 0 & 0 & 0 \end{pmatrix}. \quad (1.30)$$

The popular LEO crystal, LiNbO_3 , belongs to the $3m$ (space group C_{3v}) and has four independent tensor elements in the form [20, 18]

$$r_{ul} = \begin{pmatrix} 0 & -r_{22} & r_{13} \\ 0 & r_{22} & r_{13} \\ 0 & 0 & r_{33} \\ 0 & r_{51} & 0 \\ r_{51} & 0 & 0 \\ -r_{22} & 0 & 0 \end{pmatrix}. \quad (1.31)$$

1.2.2 Optical processes in orientationally ordered materials

The electric dipole moment is a measure of the polarity of a system such as electric charges or molecules. The polarization of the medium can be estimated to be the macroscopic sum of these electric dipole moments induced by an electric field. In organic molecules, the nature of the bonds determine the magnitude of the binding energy and consequently the ability of the electrons involved in these bonds to be

distorted by an electric field. A chromophore containing systems of conjugated π electrons is expected to have a large polarization because delocalized π electrons by alternating single and double bonds, often in aromatic systems, are more easily polarized than saturated materials. Since modulating frequencies are much lower than optical frequencies, acoustic and optical phonons can contribute to the electro-optic coefficients. However, one of the advantages of electro-optic polymers materials is that the nonlinearity is primarily electronic in nature, as opposed to inorganic materials in which the coupling to the lattice through acoustic and optical phonons contributes strongly [22]. We briefly review the relations between the molecular orientation and the optical susceptibility, concentrating on the ideal case that the medium is assumed to be linear, nondispersive, homogeneous, and isotropic⁴ based on Refs. [23, 24, 25, 26].

Linear susceptibility and birefringence

The bulk second-order susceptibilities in organic crystals are traceable to the nonlinear optical properties of the individual molecular units. Similar to Eq. 1.8, the molecular polarization is given as

$$p_J(t) = \mu_J + \alpha_{JK}(t)E_K(t) + \beta_{JKL}(t)E_K(t)E_L(t) + \dots, \quad (1.32)$$

where μ_J is the molecular ground state dipole moment, $\alpha_{JK}(t)$ the linear polarizability, and $\beta_{JKL}(t)$ the nonlinear optical susceptibilities or hyperpolarizability.

⁴It is often called an oriented gas model (OGM).

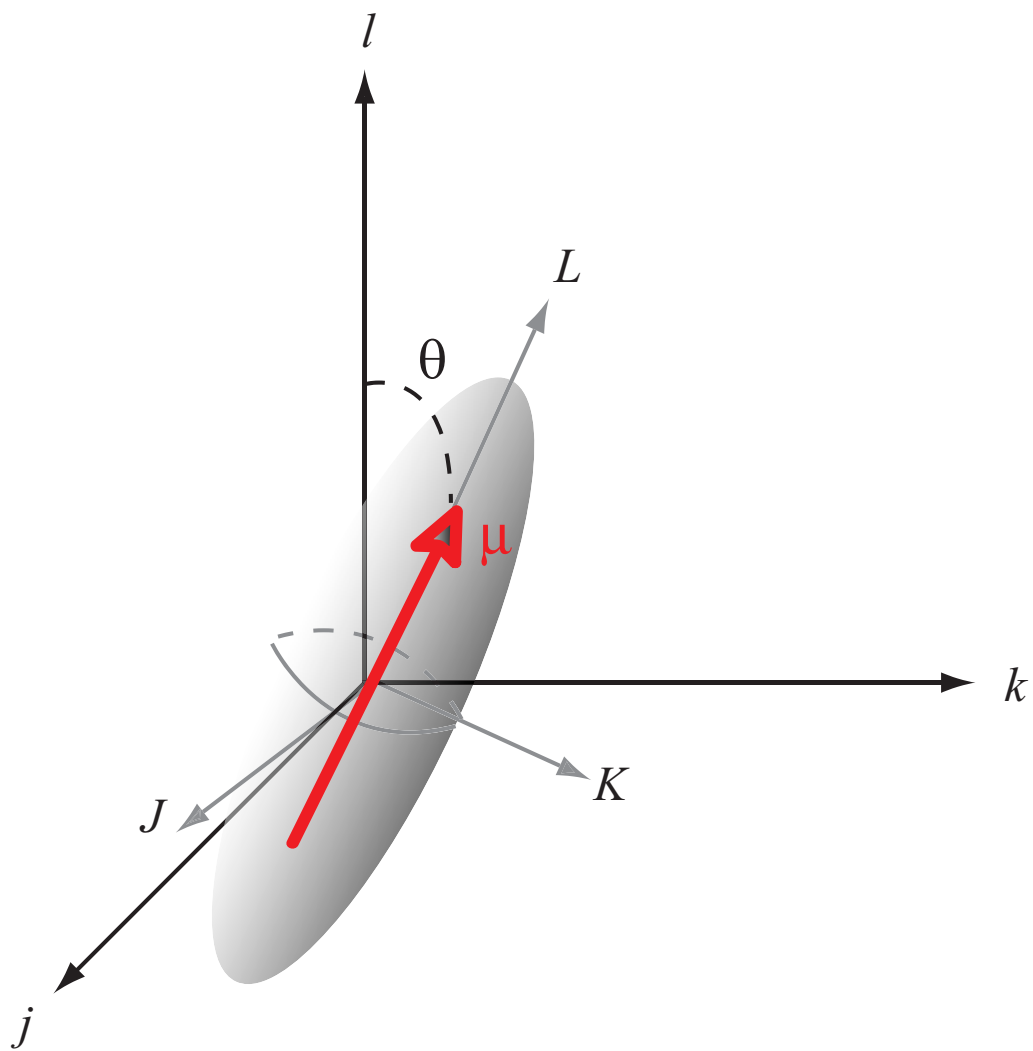


Figure 1.1: The j , k , and l axes represent the laboratory coordinates, while the J , K , and L the molecular system coordinates.

Assuming an axially symmetric polar molecule with a permanent dipole moment μ lying in the L -axis as shown in Fig.1.2, the linear polarizability is given as [27]

$$\alpha(\omega) = \begin{pmatrix} \alpha_{xx}(\omega) & \alpha_{xy}(\omega) & \alpha_{xz}(\omega) \\ \alpha_{yx}(\omega) & \alpha_{yy}(\omega) & \alpha_{yz}(\omega) \\ \alpha_{zx}(\omega) & \alpha_{zy}(\omega) & \alpha_{zz}(\omega) \end{pmatrix}. \quad (1.33)$$

Using the molecular polarization

$$p_i(\omega) = \alpha_{ii}(\omega)E_i(\omega), \quad (1.34)$$

the linear susceptibility can be expressed by a linear sum over the individual molecules with an orientational ensemble average:

$$\chi_{jk} = N\langle\alpha_{JK}^*\rangle_{jk} = N\alpha_{JK}^*\langle a_{jJ}a_{kK}\rangle, \quad (1.35)$$

where N is a number density of the molecules and $\langle\alpha_{JJ}^*\rangle$ is an orientational average of the linear susceptibility corrected by the local field factor given as

$$\langle\alpha^*\rangle = \frac{\int \alpha^*G(\Omega, E_p)d\Omega}{\int G(\Omega, E_p)d\Omega}. \quad (1.36)$$

The G is a Gibbs distribution function defined by

$$G(\Omega, E_p) = \exp[-U(\Omega, E_p)/kT], \quad (1.37)$$

where Ω is the solid angle and E_p is the poling electric field. The transformation matrix a is defined by [23]

$$\begin{pmatrix} \cos \theta \cos \phi \cos \psi - \sin \phi \sin \psi & \cos \theta \sin \phi \cos \psi + \cos \phi \sin \psi & -\sin \theta \cos \psi \\ -\cos \theta \cos \phi \sin \psi - \sin \phi \cos \psi & -\cos \theta \sin \phi \sin \psi + \cos \phi \cos \psi & \sin \theta \sin \psi \\ \sin \theta \cos \phi & \sin \theta \sin \phi & \cos \theta \end{pmatrix}. \quad (1.38)$$

Finally, the linear susceptibilities are

$$\chi_{11} = N \left[\frac{1}{4}(\langle \cos^2 \theta \rangle + 1)(\alpha_{xx}^* + \alpha_{yy}^*) + \frac{1}{2}\langle \sin^2 \theta \rangle \alpha_{zz}^* \right] = \chi_{22} \quad (1.39)$$

and

$$\chi_{33} = N \left[\frac{1}{2}\langle \sin^2 \theta \rangle (\alpha_{xx}^* + \alpha_{yy}^*) + \langle \cos^2 \theta \rangle \alpha_{zz}^* \right]. \quad (1.40)$$

Using the ensemble average of the Legendre polynomial, $\langle P_2 \rangle$, we can rewrite

$$\chi_{11} = N \left\{ \frac{-1}{3} \left[\alpha_{zz}^* - \frac{1}{2}(\alpha_{xx}^* + \alpha_{yy}^*) \right] \langle P_2 \rangle + \frac{1}{3}(\alpha_{xx}^* + \alpha_{yy}^* + \alpha_{zz}^*) \right\} \quad (1.41)$$

and

$$\chi_{33} = N \left\{ \frac{2}{3} \left[\alpha_{zz}^* - \frac{1}{2}(\alpha_{xx}^* + \alpha_{yy}^*) \right] \langle P_2 \rangle + \frac{1}{3}(\alpha_{xx}^* + \alpha_{yy}^* + \alpha_{zz}^*) \right\}. \quad (1.42)$$

For simplicity, assuming a one dimensional molecule, we have only one nonzero α_{zz}^* .

Using $1 + \chi = n^2$, the relationship between birefringence and $\langle P_2 \rangle$ can be expressed

as

$$n_3^2 - n_1^3 = \chi_{33} - \chi_{11} = N\alpha_{zz}^* \langle P_2 \rangle. \quad (1.43)$$

Second-order nonlinearity

In a similar way to the first-order susceptibility, the second-order nonlinear susceptibility can be expressed as

$$\chi_{jkl} = N \langle \beta_{JKL}^* \rangle_{jkl} = N \beta_{JKL}^* \langle a_{jJ} a_{kK} a_{lL} \rangle. \quad (1.44)$$

For the one dimensional molecule we have only one nonzero β_{zzz}^* . Then we have

$$\chi_{jkl} = N \beta_{zzz}^* \langle a_{jz} a_{kz} a_{lz} \rangle. \quad (1.45)$$

The nonzero tensor components in the material we are interested in are χ_{113} and χ_{333} . Finally, we have

$$\chi_{113} = N \beta_{zzz}^* \langle a_{1z} a_{1z} a_{3z} \rangle = \frac{N}{2} \beta_{zzz}^* \langle \cos \theta - \cos^3 \theta \rangle \quad (1.46)$$

and

$$\chi_{333} = N \beta_{zzz}^* \langle a_{3z} a_{3z} a_{3z} \rangle = N \beta_{zzz}^* \langle \cos^3 \theta \rangle, \quad (1.47)$$

which can be expressed in terms of the Legendre polynomials as

$$\chi_{113} = \frac{N \beta_{zzz}^*}{5} (\langle P_1 \rangle - \langle P_3 \rangle) \quad (1.48)$$

and

$$\chi_{333} = \frac{N\beta_{zzz}^*}{5} (2\langle P_3 \rangle + 3\langle P_1 \rangle) . \quad (1.49)$$

The Legendre polynomials can be constructed by using the recurrence relations in the form

$$(n + 1)P_{n+1}(x) = (2n + 1)xP_n(x) - nP_{n-1} , \quad (1.50)$$

where $x = \cos \theta$.

Oriental distribution functions

The electro-optic coefficient r_{33} can be expressed in terms of the order parameter $\langle \cos^3 \theta \rangle$. To determine the orientational average, we have to figure out the Gibbs distribution function shown in Eq. 1.37. In that function, U is the potential energy of the chromophore including intermolecular interactions of the chromophore and interactions with the chromophore and the local poling field. Various models can be found in Refs. [23, 28, 25, 26, 29] to describe the potential energy term. The approximations generally made in considering the potential energy as $U \approx \mu f(0)E_p \cos \theta$ by an oriented gas model (OGM) gives [24]

$$\langle \cos^n \theta \rangle = L_n[\mu f(0)E_p/kT] , \quad (1.51)$$

where L_n are the Langevin functions, $f(\omega)$ a local-field correction, and E_p the electric

poling field [24]. Then, we can write

$$\langle \cos \theta \rangle = L_1(y) = \coth y - \frac{1}{y} \quad (1.52)$$

$$\langle \cos^2 \theta \rangle = L_2(y) = 1 + \frac{2}{y^2} - \frac{2}{y} \coth y \quad (1.53)$$

$$\langle \cos^3 \theta \rangle = L_3(y) = (1 + 6y^2) \coth y - \frac{3}{y} \left(1 + \frac{2}{y^2} \right), \quad (1.54)$$

where $y = \mu f(0)E_p/kT$. For $\mu E_p/kT \ll 1$ Equation 1.54 can be approximated by

$$\langle \cos^3 \theta \rangle = \mu f(0)E_p/5kT. \quad (1.55)$$

Under the weak poling condition, that is, assuming that y is small, χ_{113} becomes 1/3 of χ_{333} .

1.2.3 Polymer systems

The second order NLO properties originate from noncentrosymmetric alignment of chromophores in poled polymer. To obtain device quality from NLO materials, a NLO polymer should satisfy some conditions: high nonlinearity, high intrinsic temporal stability in environments such as heat, oxygen, chemicals, light, and humidity and low optical loss at communication wavelengths. However, there can be a trade-off in that excessive nonlinearity may relinquish other advantages and vice versa. In general, the polymeric materials are comprised of guest-host system, side-chain, main-chain type, and crosslinked polymers from the point of view of the distribution and bonding types of chromophores [1, 30, 31].

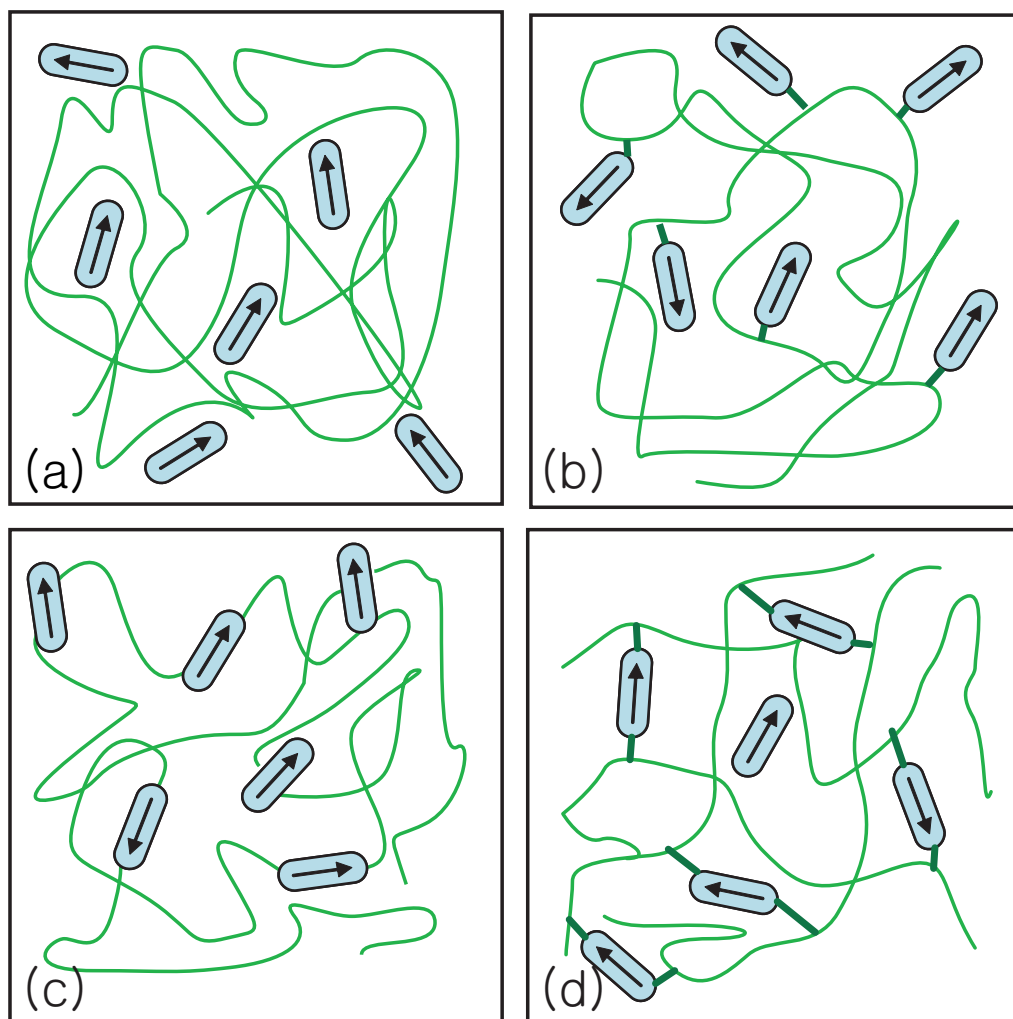


Figure 1.2: Simplified schematics of chemical structures of (a) guest host, (b) side chain, (c) main chain, and (d) crosslinked polymer system.

Guest Host (GH) Unattached chromophores (guest) dissolved in a polymer host are shown in Fig. 1.2(a). At high temperature, they can diffuse to the surface of the film and evaporate to the air. High concentrations of guest lead to dipole-to-dipole aggregation and phase-separate causing light scattering. The glass transition temperature (T_g) of the polymer host decreases due to plasticization by the guest chromophore. T_g is important in satisfying the device stability requirements for commercialization. Generally, GH-type NLO polymer with high glass transition temperature and chromophore with large molecular mass increases long term stability.

Side Chain (SC) Better thermal stability can be obtained if the nonlinear chromophore is chemically attached to the backbone as shown in Fig. 1.2(b). This type of polymer has the advantage that a high nonlinear chromophore concentration can be incorporated into the polymer system without aggregation, crystallization, or phase separation. The relaxation of polar order might be expected to be substantially slower than GH-type NLO polymer, because the motion of the chromophore is hindered by its attachment to the polymer backbone. Mostly, the glass transition temperature of a SC-type NLO polymer is higher than that of GH-type NLO polymer system containing the same concentration of chromophores.

Main Chain (MC) If the chromophore were to be chemically incorporated into the polymer backbone as shown in Fig. 1.2(c), poled order relaxation can be expected to be more restricted. The large segmental motions of the polymer backbone are required for efficient poling, so poling may be more difficult for MC than for GH

and SC-type NLO polymers. However, The relaxation of poled order is significantly inhibited. Additionally, the mechanical properties are improved.

Crosslink (XL) Crosslinking reactions increase the long term temporal stability below the glass transition temperature. Crosslinks are covalent bonds linking one polymer chain to another as shown in Fig.1.2(d). They have the characteristic property of a thermosetting polymer that cures to a rigid form through the addition of energy. Crosslinking can be formed by heat, pressure, chemical reaction, or radiation. Once the material is crosslinked, it is generally difficult or even impossible to repole.

1.2.4 Chromophore orientation techniques

The orientation of molecular dipoles in an electric field is necessary to break the centrosymmetry and generate nonlinearity. The creation of macroscopic noncentrosymmetry is one of the important tasks in getting functionalized polymers for second order NLO applications. There are a few techniques to achieve second order nonlinearity in an amorphous polymer:

- Static field poling.
- Photo induced poling.
- All optical poling.
- Langmuir-Blodgett-Kuhn processing.

The static poling technique takes advantage of the interaction between dipole moments and the applied static field; e.g., corona poling, electrode contact poling, photothermal poling, and electron beam poling. Photo-assisted and all optical poling utilize the cooperative effect of static and optical field and purely optical field, respectively. In Langmuir-Blodgett-Kuhn processing, the polymers have hydrophilic and hydrophobic properties and their forces are used to orient chromophores normal to the film surface.

Corona and electrode contact poling setups are illustrated in Fig. 1.3(a) and (b), respectively. The NLO polymer is heated to a temperature near the glass transition temperature (T_g) and then a DC electric field is gradually applied to the film, after which the sample is cooled down to room temperature while maintaining the applied electric field. These techniques have some advantages and drawbacks. Although corona poling allows one to apply a high poling field, it often leads to dielectric damage of the thin film surface. The corona creates the surface charges on the film surface, causing the dipoles to orient in the direction of the field. On the other hand, electrode contact poling is limited by the applied voltage because

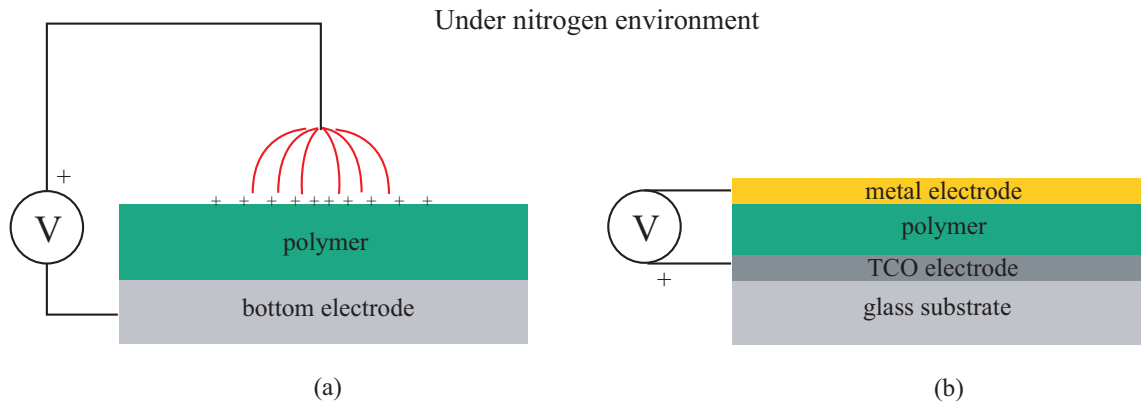


Figure 1.3: Schematics of (a) Corona and (b) electrode contact poling.

of dielectric breakdown.

Photothermal poling uses a focused laser beam to heat the polymer film locally to near the T_g under the external applied voltage [32]. It is useful to make a periodical poling pattern which is necessary for quasi-phase matching second harmonic generation (QPM SHG). Electron beam poling uses a monoenergetic electron beam which allows constant current corona poling as the sample is charged with a constant current [33]. The electrons decelerate in the sample and are trapped inside and the dipoles are oriented by the field of the trapped electrons.

1.2.5 Applications of second-order nonlinear polymers

The second-order nonlinear polymer has been exploited in the fields of photonic integrated circuits (PIC) such as the MZ-type electro-optic modulator [6, 7, 34, 35, 36], second harmonic generation [37], mode converter [38], resonators [39], optical rectification, sensor, and so on. We discuss briefly the EO modulator and quasi phase matching (QPM) SHG.

MZ EO modulator This waveguide device uses the principles of the Mach-Zehnder interferometer [40]. One or both arms can be poled by using the electrode contact poling method so that a relative phase difference between each light in the two arms can be controlled by a voltage applied to the electrodes. Figure 1.4(a) shows a push-pull type of MZ EO modulator which allows a reduction in the half-wave voltage V_π by half of the traditional V_π [41]. The half-wave voltage of a traditional MZ EO

modulator is defined by

$$V_{\pi} = \frac{\lambda h}{n^3 r_{33} L \Gamma}, \quad (1.56)$$

where λ is the wavelength, h the thickness of the layers, L is the length of the electrode, and Γ is the confinement factor.

QPM SHG The second harmonic power will oscillate along the direction of the poled waveguide structure because the poled polymer is not phase matched. One way of overcoming the problem is to pole periodically so that the second harmonic intensity interfere constructively as it propagates. The schematic of typical QPM SHG is shown in Fig. 1.4(b). The NLO waveguide is periodically poled to have a different χ_{zzz} direction in each segment. This structure results in no decrease in the second harmonic (SH) intensity because the guided SH wave interferes constructively as it propagates. Ju *et al.* demonstrated QPM SHG with a side-chain polymer waveguide whose normalized SHG efficiency shows 2.2% $\text{W}^{-1}\text{cm}^{-2}$ [37].

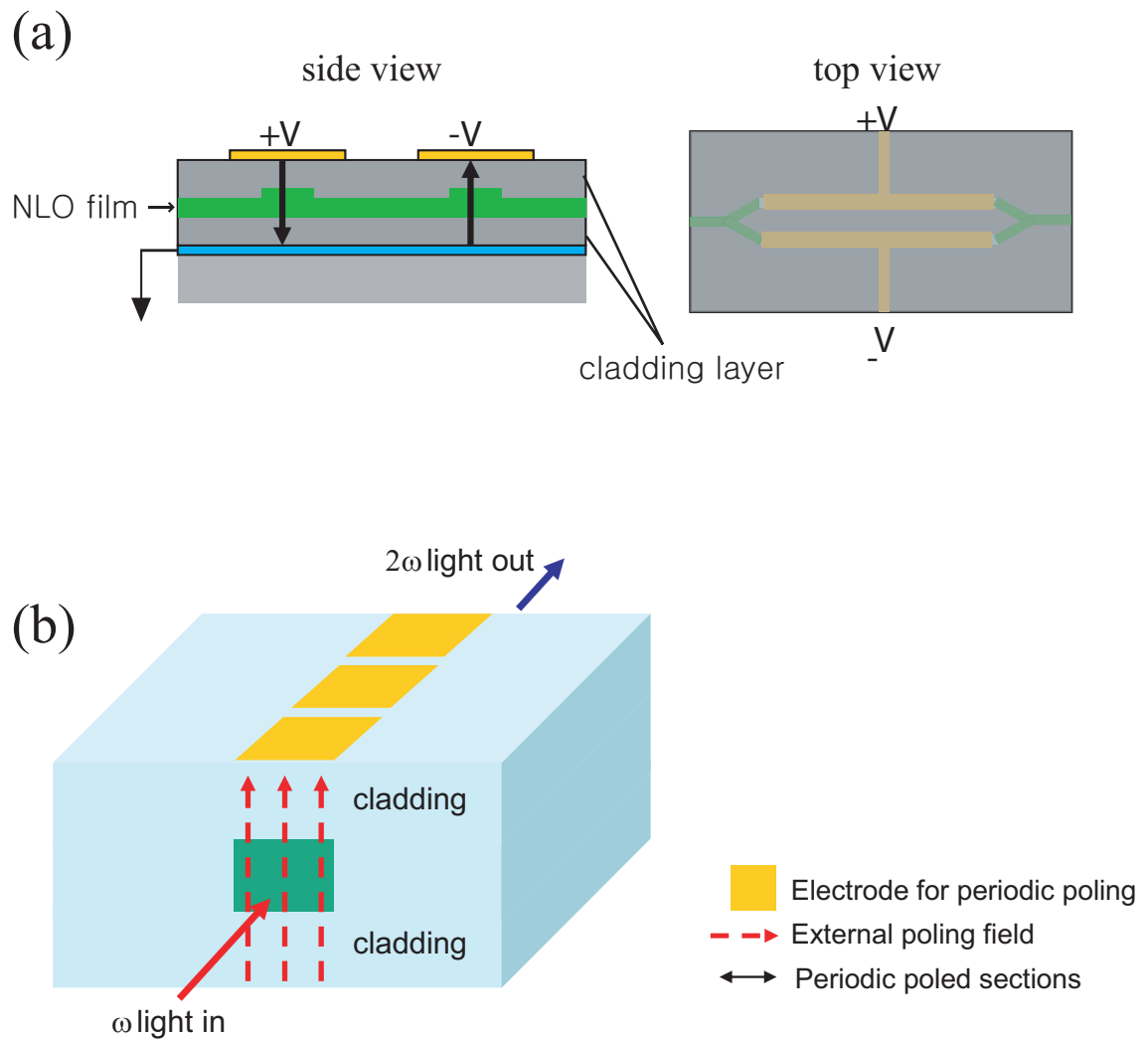


Figure 1.4: Schematic of (a) Mach-Zehnder electro-optic modulator and (b) quasi phase matching second harmonic generation.

1.2.6 Characterization methods

There are various techniques for measuring LEO effects of NLOP thin films. Methods include Mach-Zehnder (MZ) interferometry [42, 43, 44], Fabry-Perot (FP) interferometry [45], attenuated total reflection (ATR) [46, 47, 48, 49], waveguide method [50, 51], and two slit interference method [52]. One of the most popular measurement techniques is a reflection method introduced by Teng and Man [13] (Teng-Man) as well as by Schildkraut [14]. A transmission method was first mentioned by Schildkraut [14, 53], and was later discussed in some detail by Lundquist, *et al.* [54]. This method, which also measures a relative phase-shift, affords a somewhat simpler alignment compared to the reflection method, but requires two transparent electrodes. In almost all of these techniques, a modulated electric field is applied to the sample as this allows for the use of lock-in techniques to improve the signal-to-noise ratio. Jiang *et al.* presented an ATR technique which doesn't require the use of lock-in amp [49]. We discuss the Teng-Man reflection method and ATR in this thesis.

1.3 Convention

Almost all undergraduate physics texts, as well as engineering books at all levels, employ the international system (SI) of units throughout. Here we adopt the SI system as well. Regarding the notation for a plane wave, the one used in most physics texts is employed. That is, the \hat{x} -polarized electric field of the plane wave propagating in the \hat{r} -direction is expressed as

$$\bar{\mathbf{E}}(r, t) = \text{Re}\{\hat{x}E_0e^{i(k_0\tilde{n}z-\omega t)}\}, \quad (1.57)$$

where k_0 is the wave vector in free space and \tilde{n} is the complex index of refraction of a medium. As a result, the complex index of refraction has the form of $\tilde{n} = n + i\kappa$ where the imaginary part κ is equal to or larger than 0.

To describe the circular polarization, the trajectory of the endpoint of the electric field vector toward the propagating direction is considered at a fixed time t .⁵ For the right-handed circular polarization, the trajectory rotates counterclockwise when viewed from the propagation direction as shown in Fig.1.5. Using Jones vector representations, the right-handed and left-handed circularly polarized (RCP and LCP, respectively) light can be written as

$$\text{RCP} : \begin{pmatrix} E_x \\ E_y \end{pmatrix} = e^{i\phi} \frac{1}{\sqrt{2}} \begin{pmatrix} 1 \\ -i \end{pmatrix} \quad (1.58)$$

⁵Sometimes, the trajectory of the electric field is considered at a fixed position. For a more information, see [40]

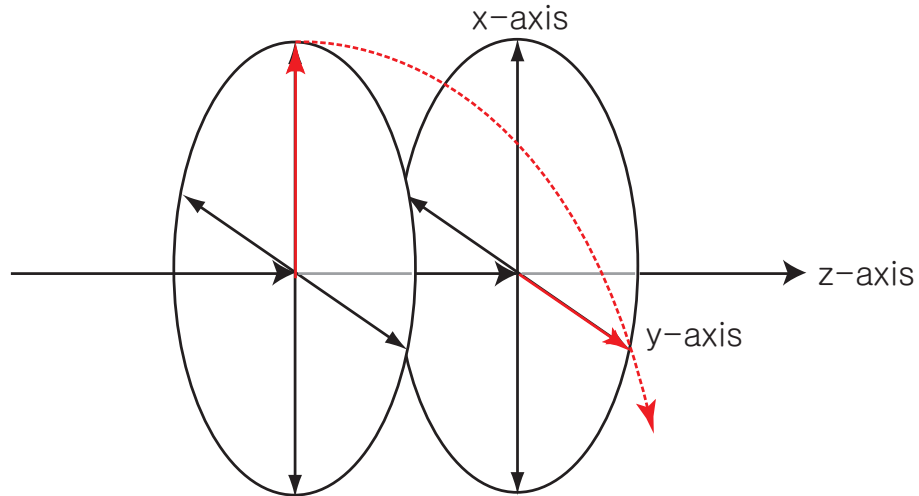


Figure 1.5: The trajectory of the electric field in the plane wave propagating in the z -direction represents the right-handed circularly polarized (RCP) light.

and

$$\text{LCP} : \begin{pmatrix} E_x \\ E_y \end{pmatrix} = e^{i\phi} \frac{1}{\sqrt{2}} \begin{pmatrix} 1 \\ i \end{pmatrix}, \quad (1.59)$$

where ϕ is an arbitrary phase of the electric field.

1.4 Scope of thesis

This thesis is separated into three principal parts: two parts for two characterization methods and one for experimental results.

Chapter 2 discusses the analysis of Teng-Man measurements of the electro-optic coefficients of poled polymer thin films. In this chapter, we provide new closed-form expressions for analysis of Teng-Man data including absorption of both the film and TCO layers. The analysis also applies to any uniaxial nonlinear thin film with the c -axis perpendicular to the nonlinear film surface, such as poled polymer thin films and z -cut LiNbO₃ crystal. In general, the modulation of both the real and imaginary parts of the complex refractive index under application of an electric field depends on both the real and imaginary parts of the complex EO coefficient, particularly inside the linear absorption band of the polymer [53]. Two models, both allowing for absorption of the nonlinear polymer layer, are analyzed and compared: a simple model that takes into account only the properties of the nonlinear polymer layer without multiple reflections and a rigorous model accounting for properties of the complete stratified layers of the test structure including multiple reflections. In both models, analytic expressions that are linearly dependent on the real and imaginary parts of the complex EO coefficient are presented so that standard linear least squares data analysis can be performed. In the case of the simple model, we obtain equations to characterize the imaginary part of the complex EO coefficients that are somewhat different from those reported earlier [16, 53, 55] as well as an identical equation to that usually used in the Teng-Man method for the real part

[18] outside the absorption band of the polymer. The rigorous model has the same fundamental starting point as that of Ref. [16], namely, the description of the total reflectivity of the multilayer structure. But we provide explicit analytic expressions for all derivatives involved along with a new compact formalism that allows a matrix representation of the dependence of the real and imaginary parts of the complex EO coefficient on the reflectivity and phase modulation. The rigorous model analysis is used to show that simple model calculations, which do not include the effects of multiple reflections, can, in some cases, either grossly underestimate or overestimate the complex electro-optic coefficient. In addition, it is shown that the relative error in using the simple model can undergo a large cyclic variation, an asymptotic behavior, or an irregular FP effect with increasing film thickness depending on operating wavelengths.

We examine the suitability of using thick z -cut LiNbO₃ to validate a Teng-Man setup for measuring EO coefficients of thin films. We use rigorous expressions for the analysis of Teng-Man data that include the absorption of a transparent conducting oxide (TCO) layer. We also examine the effect of the beam waist of a Gaussian beam optics in the Teng-Man measurement to validate the use of plane wave analysis.

Chapter 3 discusses the attenuated total reflection method. We examine the ATR method for the measurement of the EO coefficients of poled polymer thin films in multilayer structures containing a transparent conducting oxide layer. A more accurate determination of the film thickness can be achieved by considering a four-layer waveguide structure containing TCO layer (air/film/TCO/substrate) instead of the three-layer approximation to the waveguide structure (air/film/substrate).

This treatment is also applied to the determination of, $\partial N/\partial n$, the change of effective index N with respect to the EO-induced change in the refractive index n for better estimation of EO coefficients. We provide closed-form expressions of $\partial N/\partial n$ and $\partial N/\partial d$ based on the three-layer waveguide structure. The four-layer waveguide model (WGM) analysis is compared to show that the three-layer waveguide model analysis applied to a single mode NLO film can result in a large error in the determination of EO coefficients. The relative error in r_{33} using both the three-layer and four-layer waveguide models shows an asymptotic behavior with increasing film thickness, while the error from the simple Teng-Man analysis shows a large cyclic variation.

Chapter 4 discusses experimental results including the characterization of TCO such as ITO and ZnO by using the ellipsometric analysis. Selected poled NLO polymers are analyzed by the rigorous Teng-Man analysis and/or ATR method. We show that the result from the ATR method based on multilayer structure containing TCO layer is in a good agreement with that from the rigorous Teng-Man analysis.

Appendix A describes the mathematical expressions of the variation of propagation constant β and H functions used in the rigorous Teng-Man analysis in details.

Appendix B presents MATLABTM codes for the calculation of the estimate of the error resulting from the simple Teng-Man method. A free Java Teng-Man error estimator software program is introduced.

TENG-MAN METHOD

2.1 Introduction

2.1.1 Characterization methods

The EO effect can be determined by measuring the change of the dielectric constant or index of refraction when a field is applied across the NLO sample of interest. As we briefly discussed in Section 1.2.6, methods for measuring the linear electro-optic (LEO) effect include free space or fiber-optic Mach-Zehnder (MZ) interferometry [42, 43, 44], Fabry-Perot (FP) interferometry [45], attenuated total reflection (ATR) [46, 47, 48, 49], waveguide method [50, 51], and two slit interference method [52]. One of the most popular measurement techniques is a reflection method introduced by Teng and Man [13] (Teng-Man) as well as by Schildkraut [14]. The reflection measurement is generally easier to make compared to techniques such as MZ interferometry because it simply takes advantage of a relative phase-shift difference between the $s(\text{TE})$ - and $p(\text{TM})$ - polarized waves of a single laser beam reflected from the sample when a modulating voltage is applied across two parallel-plate electrodes. A transmission method was first mentioned by Schildkraut [14, 53], and

later discussed in some detail by Lundquist, *et al.* [54]

2.1.2 Teng-Man method

The EO properties of NLO films are often characterized using the Teng-Man reflection method because it is simple and quick [13, 14]. The vast majority of quoted values of the electro-optic coefficient that are obtained from Teng-Man measurements result from a simplified analysis of the data that assumes the transparent conducting oxide (TCO) is perfectly transparent and the gold is perfectly reflective. Consequently only the properties of the EO material [refractive indices (generally anisotropic in poled films), EO coefficients, and angle of incidence] are taken into account. However, it was realized that experimental error can result from ignoring the reflection off the substrate/film interface and that an accurate determination of the EO coefficient could be achieved only by a numerical calculation that applies anisotropic Fresnel equations to the stratified layers containing the nonlinear poled polymer [13, 14]. This requires a knowledge of the refractive index and thickness of all the layers. In addition, the simple analysis is valid only when the absorption of the film is negligible. Furthermore, Michelotti, *et al.* [15] reported that the simple Teng-Man analysis can give unreliable measurements if the experimental setup is operated in a spectral region where the TCO layer is absorbing, and suggested that if it is only slightly absorbing it is still possible to evaluate the EO properties of the polymer films with reasonable precision. Another disadvantage of the ellipsometric method is the impossibility in determining the r_{13} and r_{33} EO tensor coefficients

separately.

Shuto and Amano measured the EO coefficient of 0.5 mm thick z -cut LiNbO₃ crystal for validation of the Teng-Man setup. Wang *et al.* claimed a precise Teng-Man measurement by the cautious selection of near-infrared (NIR) In₂O₃ thin film electrodes [56]. In Section 2.3, we evaluate the suitability of using thick LiNbO₃ to validate a Teng-Man setup for a thin film measurement.

The effect of electrochromism (variation of the imaginary part of the index of refraction under application of an electric field) and the complex EO coefficient were added in Ref. [53], followed by efforts by a few researchers to characterize other nonlinear properties, such as the complex quadratic EO coefficient, based on a simple analysis of Teng-Man data [55]. Levy, *et al.* [16] and Chollet, *et al.* [17] presented both simple and rigorous expressions for estimation of the complex EO coefficient. Numerical solutions to the rigorous expressions were obtained using the simplex method [17]. They also pointed out that the modulated intensity at the maximum of the optical bias curve and some of the modulation dependence on the angle of incidence are attributed to absorption of the film and to multiple reflections, respectively. Ignoring the multiple reflections inside the polymer film, Khanarian, *et al.* [57] derived an approximate equation for the real part of the EO coefficient that takes into account the effects of reflectivity modulation at the glass/polymer and polymer/metal interfaces. Han and Wu [58] measured the modulated intensity as a function of optical bias, optical polarization, and angle of incidence in an effort to distinguish FP effects from EO phase modulation.

2.1.3 Outline of this chapter

In this chapter, we provide new closed-form expressions for analysis of Teng-Man data including absorption of both the film and TCO layers. The analysis also applies to any uniaxial nonlinear thin film with the c -axis perpendicular to the nonlinear film surface, such as thin z -cut LiNbO_3 . In the case of the simple model, we provide equations to characterize the imaginary part of the complex EO coefficients that are somewhat different from those reported earlier [16, 53, 55] as well as an identical equation to that usually used in the Teng-Man method for the real part [18] outside the absorption band of the polymer. We provide explicit analytic expressions for all derivatives involved along with a new compact formalism that allows a matrix representation of the dependence of the real and imaginary parts of the complex EO coefficient on the reflectivity and phase modulation. The rigorous model analysis is used to show that simple model calculation can either grossly underestimate or overestimate the complex electro-optic coefficient. We also show the relative error in using the simple model undergo a large cyclic variation, an asymptotic behavior, or an irregular FP effect with increasing film thickness depending on operating wavelength.

We discuss the estimate of error in the anisotropic case and the rigorous Teng-Man analysis for thick films. We also examine the suitability of using thick z -cut LiNbO_3 to validate a Teng-Man setup for measuring EO coefficients of thin films. We use rigorous expressions for the analysis of Teng-Man data that include the absorption of both the NLO film and transparent conducting oxide (TCO) layers.

Two types of analyses, one using simplified and the other using rigorous reflectance expressions, based on the plane wave analysis are employed. These are referred to as the simple and the rigorous model, respectively. We also examine the influence of the beam waist of a Gaussian beam on Teng-Man measurements.

2.2 Theory and analysis

2.2.1 Expression for variation of index of refraction

A poled organic thin film prepared by spin coating belongs to the point-group symmetry ∞mm (space group $C_{\infty v}$) [21] and has complex ordinary and extraordinary indices of refraction, $\tilde{n}_o (= n_o + i\kappa_o)$ and $\tilde{n}_e (= n_e + i\kappa_e)$, respectively. Two independent complex electro-optic tensor elements $\tilde{r}_{13} (= r_{13} + is_{13})$ and $\tilde{r}_{33} (= r_{33} + is_{33})$ determine the variations $\delta\tilde{n}_o (= \delta n_o + i\delta\kappa_o)$ and $\delta\tilde{n}_e (= \delta n_e + i\delta\kappa_e)$ of the complex refractive indices when an electric field V is applied to the film according to [53]

$$\delta\tilde{n}_\mu = -\frac{1}{2}\tilde{n}_\mu^3(r_{\mu 3} + is_{\mu 3})E_3, \quad (2.1)$$

where $\mu = 1$ or 3 ($n_1 = n_o$ and $n_3 = n_e$). For a parallel plate structure, $E_3 = V/d$, where V is the peak voltage of the AC signal applied to the sample and d is the thickness of the film. Usually it is argued that the real part, δn_μ , of $\delta\tilde{n}_\mu$ depends only on $r_{\mu 3}$ and the imaginary part, κ_μ , depends only on $s_{\mu 3}$ outside the polymer absorption band under the assumptions that $n \gg \kappa$, $n\delta\kappa \gg \kappa\delta n$, [53] and $\kappa\delta\kappa \ll n\delta n$.

Separation of Eq. 2.1 into real and imaginary parts gives

$$\delta n_\mu = -\frac{n_\mu^3}{2} \left[\left(1 - 3\frac{\kappa_\mu^2}{n_\mu^2} \right) r_{\mu 3} + \left(\frac{\kappa_\mu^2}{n_\mu^2} - 3 \right) \frac{\kappa_\mu}{n_\mu} s_{\mu 3} \right] E_3 \quad (2.2)$$

and

$$\delta\kappa_\mu = -\frac{n_\mu^3}{2} \left[\left(1 - 3\frac{\kappa_\mu^2}{n_\mu^2}\right) s_{\mu 3} + \left(3 - \frac{\kappa_\mu^2}{n_\mu^2}\right) \frac{\kappa_\mu}{n_\mu} r_{\mu 3} \right] E_3. \quad (2.3)$$

It can be seen that the change in both the real and imaginary parts of the refractive index depends in general on both the real and imaginary parts of the electro-optic coefficients. Even for a highly absorptive medium, at communication wavelengths the extinction coefficient is small (10 dB/cm loss corresponds to an extinction coefficient $\kappa = 0.000024$), so $\kappa/n \ll 1$ is a reasonable approximation. With these considerations in mind, for communication wavelengths in the 1300-1600 nm range, Eqs. 2.2 and 2.3 can be simplified to

$$\delta n_\mu = -\frac{n_\mu^3}{2} \left(r_{\mu 3} - 3\frac{\kappa_\mu}{n_\mu} s_{\mu 3} \right) E_3 \quad (2.4)$$

and

$$\delta\kappa_\mu = -\frac{n_\mu^3}{2} \left(s_{\mu 3} + 3\frac{\kappa_\mu}{n_\mu} r_{\mu 3} \right) E_3. \quad (2.5)$$

Outside the absorption band, we expect $r_\mu \gg 3(\kappa_\mu/n_\mu)s_\mu$, which simplifies Eq. 2.4 to

$$\delta n_\mu = -\frac{1}{2} n_\mu^3 r_{\mu 3} E_3. \quad (2.6)$$

Furthermore, still outside the absorption band, the assumption $s_\mu \gg 3(\kappa_\mu/n_\mu)r_\mu$ reduces Eq. 2.5 to

$$\delta\kappa_\mu = -\frac{n_\mu^3}{2} s_{\mu 3} E_3. \quad (2.7)$$

We note that the conditions $r_\mu \gg 3(\kappa_\mu/n_\mu)s_\mu$ and $s_\mu \gg 3(\kappa_\mu/n_\mu)r_\mu$ are equivalent

to those in Ref. [53] and Eqs. 2.6 and 2.7 are valid outside the polymer absorption band. Consequently, in this case δn and $\delta \kappa$ depend only on r_{33} and s_{33} , respectively. Within the absorption band of the polymer, however, this is not true and Eq. 2.1 or, equivalently, Eqs. 2.2 and 2.3 should be used.

2.2.2 General expressions

Figure 2.1 is the schematic for the Teng-Man measurement setup. As shown in the figure, 45° polarized light is incident at an angle on the multilayered sample structure containing the nonlinear poled thin film. The polymer material is usually spin-coated on a glass substrate coated with TCO, commonly indium tin oxide (ITO), and poled electrically to generate the second order nonlinearity. The first reflection off the air-glass interface and subsequent beams resulting from reflection of the first pass on its way out at the glass/air interface back into the polymer and out again are blocked [13, 14, 53]. The remaining light reflected off the sample experiences an additional controllable phase retardation introduced by a Soleil-Babinet Compensator (SBC). The intensity of the light is detected after passing through the analyzer using a lock-in amplifier. At each angle of incidence, two different data sets, the optical bias curve $I_{dc}(\Omega)$ and the modulated intensity $I_m(V, \Omega)$ are collected. The optical bias curve is the intensity profile obtained by varying the retardation generated by the SBC with no applied voltage to the sample, while the modulation data set is obtained by applying an AC voltage $V \sin(\omega t)$ to the sample and using a lock-in amplifier synced to the fundamental frequency of the applied

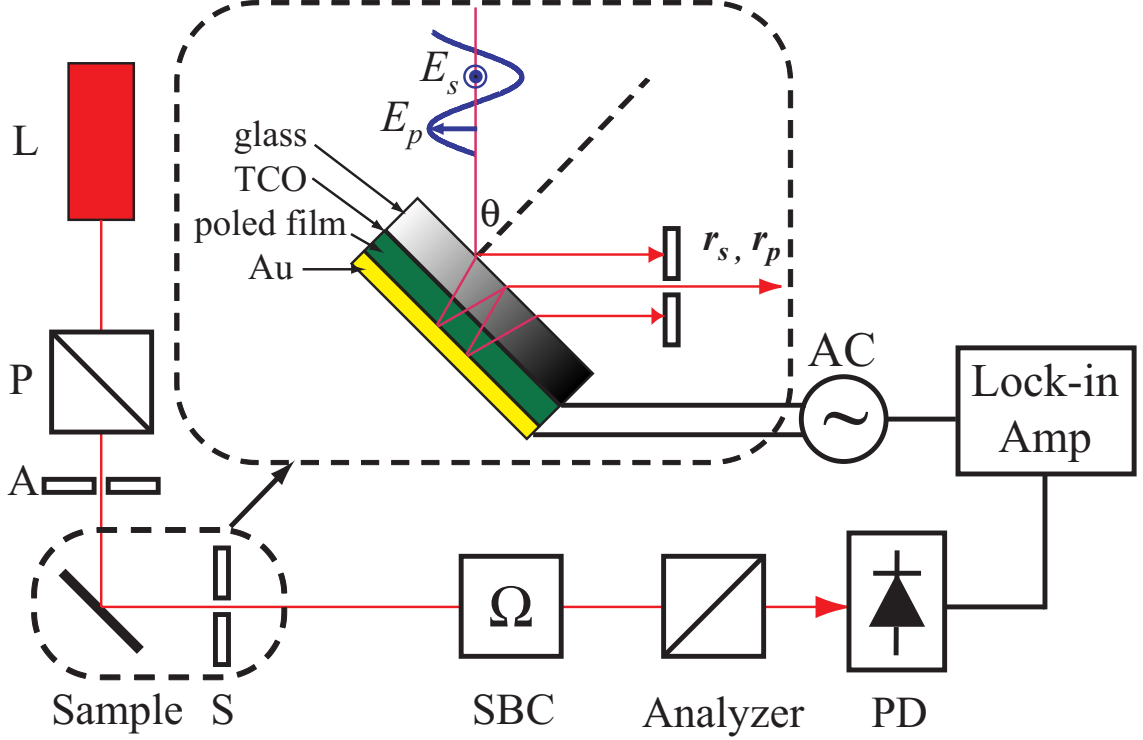


Figure 2.1: Schematic of the experimental Teng-Man setup. L is laser, P polarizer, A aperture, S slit, SBC Soleil-Babinet Compensator, and PD photodetector.

voltage to record the resulting modulation of $I_{dc}(\Omega)$ for a given retardation. $I_{dc}(\Omega)$ can be expressed in terms of the complex reflection coefficients r_s and r_p of the s - and p - polarized waves, the intensity of the incident laser I_o , and the phase retardation Ω [15, 17, 16].

Using Jones vector representation, the electric field at the photodetector can be expressed by

$$\begin{pmatrix} E_x \\ E_y \end{pmatrix} = \frac{E_o}{2} \begin{pmatrix} 1 & 1 \\ 1 & 1 \end{pmatrix} \begin{pmatrix} e^{i\Omega} & 0 \\ 0 & 1 \end{pmatrix} \begin{pmatrix} r_s & 0 \\ 0 & -r_p \end{pmatrix} \begin{pmatrix} \frac{1}{\sqrt{2}} \\ \frac{1}{\sqrt{2}} \end{pmatrix}, \quad (2.8)$$

where the first 2×2 matrix represents the crossed polarizer, the second one the SBC, the third the reflectance from the sample, and the last 2×1 matrix the vector

for 45° polarized light after the 45° polarizer. Note that the first 2×2 matrix representation for the crossed polarizer doesn't look crossed compared to the input polarization. This is because the y -axis (horizontal) of the coordinate system is flipped after the reflection. For the same reason, the sign of the r_p is the minus in the third matrix for the reflectance from the sample. The measured optical intensity, I , is proportional to the square of the electric field, $|\bar{E}|^2 = E_x^2 + E_y^2$. Varying the optical bias Ω generates the optical bias curve, which is given by

$$I_{dc} = \frac{I_o}{4} |r_s e^{i\Omega} - r_p|^2 = A + B \sin^2 \left(\frac{\Psi_{sp} + \Omega}{2} \right), \quad (2.9)$$

where

$$A = \frac{I_o}{4} (|r_s|^2 - |r_p|^2), \quad B = I_o |r_s| |r_p|, \quad (2.10)$$

$$r_s = |r_s| e^{i\Psi_s}, \quad r_p = |r_p| e^{i\Psi_p}, \quad (2.11)$$

and

$$\Psi_{sp} = \Psi_s - \Psi_p. \quad (2.12)$$

A and B can be expressed in terms of the ellipsometric parameter $\tan \Phi$, where

$$\frac{r_p}{r_s} = \tan \Phi \exp(-i\Psi_{sp}), \quad (2.13)$$

as follows,

$$A = \frac{I_o}{4} |r_s|^2 (1 - \tan \Phi)^2, \quad B = I_o |r_s|^2 \tan \Phi. \quad (2.14)$$

To first order in V , the modulated intensity $I_m(V, \Omega)$ is obtained by differentiating Eq. 2.9 to get

$$I_m = \delta A + \delta B \sin^2 \left(\frac{\Psi_{sp} + \Omega}{2} \right) + \frac{B}{2} \sin(\Psi_{sp} + \Omega) \delta \Psi_{sp}. \quad (2.15)$$

Representative data curves for optical bias I_{dc} and modulation I_m are shown in Fig. 2.2. We note in general that I_m is not symmetric with respect to the horizontal axis and the modulated intensities at points 1 and 2 are not maximum and minimum, respectively. From Eq. 2.15, $\delta \Psi_{sp}$ can be extracted by measuring the modulated intensities I_{m1} and I_{m2} at the two optical bias points corresponding to $\Psi_{sp} + \Omega = \pi/2, 3\pi/2$ as

$$\delta \Psi_{sp} = \frac{I_m(\pi/2) - I_m(3\pi/2)}{2I_c}, \quad (2.16)$$

where $I_c = B/2$. $\delta B/B$ can be obtained from the modulated intensities I_{m3} and I_{m4} at the two bias points corresponding to $\Psi_{sp} + \Omega = 0, \pi$ according to

$$\frac{\delta B}{B} = \frac{I_m(\pi) - I_m(0)}{2I_c}. \quad (2.17)$$

Typically, in the Teng-Man method, I_m is measured only at points 1 and 2 as a function of voltage and the average of the difference in the slopes in the plot of I_m versus V is used in Eq. 2.16 to extract $\delta \Psi_{sp}$. This verifies that the applied voltage is low enough to stay in the linear regime, as required for the validity of Eq. 2.16. Usually, I_m is positive at point 1 and negative at point 2 or vice versa. But this

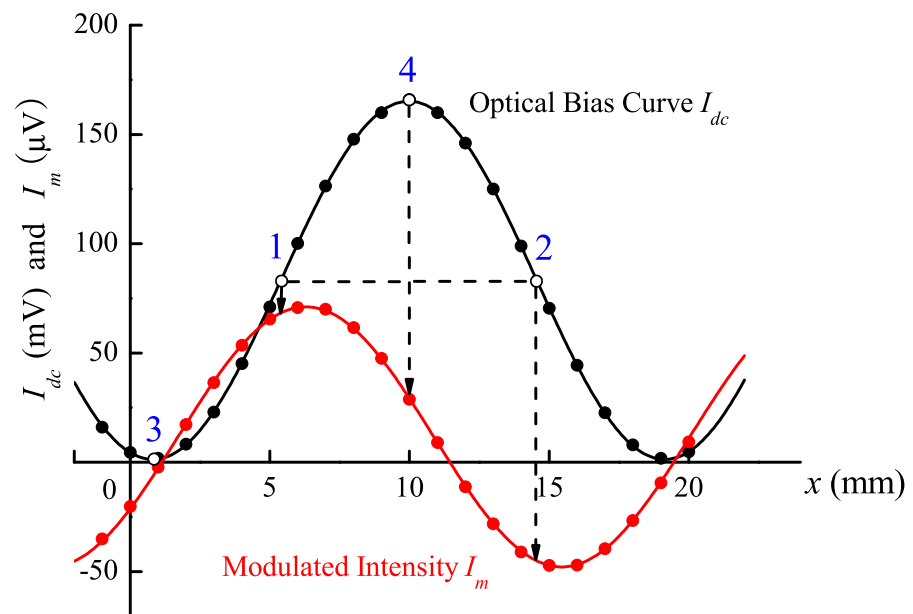


Figure 2.2: The optical bias curve and modulated intensity obtained as a function of SBC retardation setting x for a representative set of experimental data on a film. Points 1, 2, 3, and 4 correspond to compensator settings such that $\Psi_{sp} + \Omega = \pi/2, 3\pi/2, 0,$ and π , respectively.

is not always the case so care must be taken to note the phase of the reading on the lock-in amplifier, synced to the fundamental frequency of the applied voltage $V \sin(\omega t)$. A similar technique can be applied to obtain $\delta B/B$ from data at points 3 and 4 using Eq. 2.17. To measure modulated intensities at only points 1 and 2 in Fig. 2.2, an often employed quick measurement technique is to

- (a) vary the compensator to determine the minimum I_{dc} (point 3) and maximum I_{dc} (point 4)
- (b) set the compensator to obtain the average of these two intensities to locate point 1 and measure I_{m1}
- (c) dial the compensator through the maximum to the same dc average on the other side to locate point 2 and measure I_{m2}
- (d) use Eq. 2.16 to determine $\delta\Psi_{sp}$.

This can be expected to give as accurate a value for $\delta\Psi_{sp}$ as fitting a full modulation curve, provided multiple measurements are averaged. However, to measure $\delta B/B$ using Eq. 2.17 requires precisely locating the maximum and minimum in the bias curve, but these are points where the slope of I_{dc} versus Ω is zero. One can show that for a small error $\Delta\Omega$ in the compensator setting in locating points 3 and 4, the relative error in $\delta B/B$ from using Eq. 2.17 is $-\left[\delta\Psi_{sp}/\delta B/B\right]\Delta\Omega$. With moderate reflectivity modulation and $(\delta B/B)/\delta\Psi_{sp} \approx 1$ (higher ratios are possible), and if the error in determining the maximum I_{dc} is only 1% corresponding to $\Omega \approx 0.2$, then the relative error in determining $\delta B/B$ is already 20%. Better accuracy can be obtained

by fitting the full I_{dc} versus Ω curve to reduce $\Delta\Omega$. After verifying voltage values to be in the linear regime, we prefer to measure the full $I_m(V, \Omega)$ curves [15, 55] as well as $I_{dc}(\Omega)$ as shown in Fig. 2.2 and then fit these data to Eqs. 2.16 and 2.17 to extract A , B , Ψ_{sp} , δA , δB , and $\delta\Psi_{sp}$. Acquiring the full modulation curve provides a visual check for consistency as well as improved statistics on the extracted parameters. Note that in fitting the optical bias curve we put $\Psi_{sp} + \Omega \rightarrow cx + d$, where x is the SBC setting, and obtain c and d along with A and B from the fit. These are then used in fitting Eq. 2.17 to extract δA , δB , and $\delta\Psi_{sp}$. To facilitate relating these parameters to the complex EO coefficients, we define a new complex parameter \tilde{B} as

$$\tilde{B} \equiv I_o r_s r_p^* = B e^{i\Psi_{sp}} \quad (2.18)$$

so that

$$\frac{\delta\tilde{B}}{\tilde{B}} = \frac{\delta B}{B} + i\delta\Psi_{sp} = \frac{\delta r_s}{r_s} + \left(\frac{\delta r_p}{r_p}\right)^* . \quad (2.19)$$

Thus, the modulated reflectivity and phase are just the real and imaginary parts, respectively, of $\delta\tilde{B}/\tilde{B}$. From Eq. 2.19, assuming $\tilde{r}_{13} = \gamma\tilde{r}_{33}$ (γ is generally assumed to be 1/3 for weak poling [1, 31]), and assuming no piezoelectric contribution and making a Taylor expansion to first order in $\delta\tilde{n}_{o,e}$, the complex quantity $\delta\tilde{B}/\tilde{B}$ can be written as a linear function of r_{33} and s_{33} in the form

$$\frac{\delta\tilde{B}}{\tilde{B}} = \frac{1}{r_s} \frac{\partial r_s}{\partial \tilde{n}_o} \delta\tilde{n}_o + \left(\frac{1}{r_p} \frac{\partial r_p}{\partial \tilde{n}_o} \delta\tilde{n}_o + \frac{1}{r_p} \frac{\partial r_p}{\partial \tilde{n}_e} \delta\tilde{n}_e \right)^* \equiv H_r r_{33} + H_s s_{33}. \quad (2.20)$$

Separating into real and imaginary parts, we have

$$\begin{pmatrix} \delta\Psi_{sp} \\ \frac{\delta B}{B} \end{pmatrix} = \begin{pmatrix} \text{Im}(H_r) & \text{Re}(H_s) \\ \text{Re}(H_r) & -\text{Im}(H_s) \end{pmatrix} \begin{pmatrix} r_{33} \\ s_{33} \end{pmatrix}. \quad (2.21)$$

We note in general that the ratio r_{13}/r_{33} is not equal to $\delta n_o/\delta n_e$ because of birefringence and that both $\delta\Psi_{sp}$ and $\delta B/B$ depend on both r_{33} and s_{33} . Once $\delta\Psi_{sp}$ and $\delta B/B$ are determined experimentally at any single angle of incidence, Eq. 2.21 can be inverted to solve for r_{33} and s_{33} , provided that H_r and H_s which determine the 2×2 matrix are known. This matrix depends on the linear properties of the multilayered structure and its form for the simple and rigorous models is discussed in the next two sections.

2.2.3 Simple model

The simple model ignores the properties of the TCO layer and simplifies the multilayered structure of the sample to three layers, air/film/PEC(Perfect Electric Conductor), as shown in Fig. 2.3(a). By also ignoring the reflectance at the air-film interface, the reflection coefficients of the s - and p - waves can be expressed as

$$r_s = -e^{2i\beta_s d}, \quad r_p = -e^{2i\beta_p d}, \quad (2.22)$$

where the propagation constants of the s - and p - waves normal to the film surface are defined by

$$\beta_s = k_o \tilde{n}_s \cos(\tilde{\theta}_s), \quad \beta_p = k_o \tilde{n}_p \cos(\tilde{\theta}_p), \quad (2.23)$$

where $k_o = 2\pi/\lambda$ is the wave vector in free space, $\tilde{n}_s = \tilde{n}_o$, \tilde{n}_p is given in Eq. A.2, and the complex propagation angles $\tilde{\theta}_s$ and $\tilde{\theta}_p$ inside the anisotropic nonlinear medium are given in Eq. A.1. Inserting Eq. 2.22 into the general expression Eq. 2.9 gives the optical bias curve. We introduce lower-case letters a , b , and ψ_{sp} instead of A , B , and Ψ_{sp} to designate the simple model values. We emphasize the complex nature of the propagation constants $\beta_{s,p}$ by writing $\beta_s \equiv \beta_{sr} + i\beta_{si}$ and $\beta_p \equiv \beta_{pr} + i\beta_{pi}$. Then the phase retardation inside the film is given by

$$\psi_{sp} = 2(\beta_{sr} - \beta_{pr})d, \quad (2.24)$$

which is purely real. In this simple model, the coefficients a and b depend only on the imaginary parts of the propagation constants, while ψ_{sp} depends only on the real parts. From Eqs. 2.9-2.15 together with Eq. 2.24, we have

$$\delta\psi_{sp} = 2(\delta\beta_{sr} - \delta\beta_{pr})d \quad (2.25)$$

and

$$\delta b/b = -2(\delta\beta_{si} + \delta\beta_{pi})d. \quad (2.26)$$

Inserting Eq. 2.22 into the general expression Eq. 2.19, we have

$$\begin{aligned} \frac{\delta\tilde{b}}{\tilde{b}} &= \frac{\delta b}{b} + i\delta\psi_{sp} \\ &= 2id \left[\frac{\partial\beta_s}{\partial\tilde{n}_o} \delta\tilde{n}_o - \left(\frac{\partial\beta_p}{\partial\tilde{n}_o} \delta\tilde{n}_o + \frac{\partial\beta_p}{\partial\tilde{n}_e} \delta\tilde{n}_e \right)^* \right] \\ &\equiv h_r r_{33} + i h_s s_{33}, \end{aligned} \quad (2.27)$$

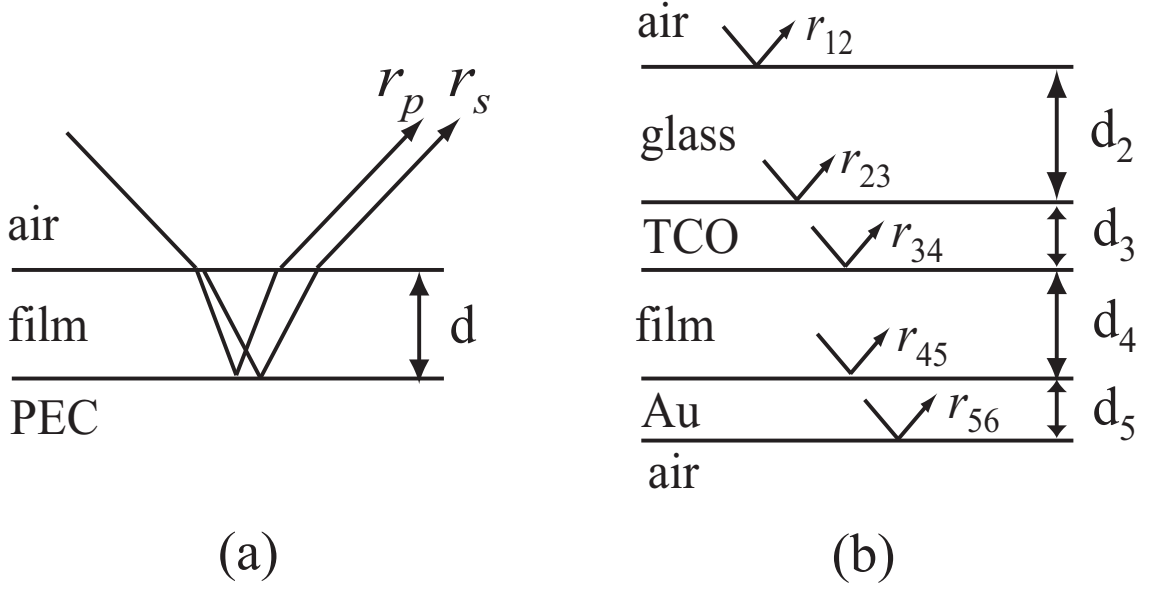


Figure 2.3: Multilayered structures in a simple model (a) and a rigorous model (b). For simplicity, subscripts s and p in the reflection coefficients are omitted in (b).

and separating into real and imaginary parts gives

$$\begin{pmatrix} \delta\psi_{sp} \\ \frac{\delta b}{b} \end{pmatrix} = \begin{pmatrix} \text{Im}(h_r) & \text{Re}(h_s) \\ \text{Re}(h_r) & -\text{Im}(h_s) \end{pmatrix} \begin{pmatrix} r_{33} \\ s_{33} \end{pmatrix}. \quad (2.28)$$

The functions h_r and h_s are complex quantities given by

$$h_r = iV \left[\left(\frac{k_o \tilde{n}_o^3}{\tilde{n}_e} \sqrt{\tilde{n}_e^2 - N^2} \right)^* \gamma - \frac{k_o \tilde{n}_o^4}{\sqrt{\tilde{n}_o^2 - N^2}} \gamma + \left(\frac{k_o \tilde{n}_o \tilde{n}_e N^2}{\sqrt{\tilde{n}_e^2 - N^2}} \right)^* \right] \quad (2.29)$$

and

$$h_s = -iV \left[\frac{k_o \tilde{n}_o^4}{\sqrt{\tilde{n}_o^2 - N^2}} \gamma + \left(\frac{k_o \tilde{n}_o^3}{\tilde{n}_e} \sqrt{\tilde{n}_e^2 - N^2} \right)^* \gamma + \left(\frac{k_o \tilde{n}_o \tilde{n}_e N^2}{\sqrt{\tilde{n}_e^2 - N^2}} \right)^* \right], \quad (2.30)$$

where $N = \sin \theta$ as defined in Eq. A.1 and we have used $r_{13} = \gamma r_{33}$ and $s_{13} = \gamma s_{33}$. The functions h_r and h_s have nonzero real and imaginary parts inside the absorption band. Outside the absorption band, we make the approximations discussed in Section 2.2.1 to compare with the formulas reported earlier [14, 16, 18, 53, 55]. Then, the 2×2 matrix in Eq. 2.28 is diagonalized because the real parts of h_r and h_s vanish, and we get

$$\begin{aligned}\delta\psi_{sp} &= -\left(\frac{n_o^4}{\sqrt{n_o^2 - N^2}} - \frac{n_o^3}{n_e} \sqrt{n_e^2 - N^2}\right) k_o \gamma r_{33} V + \frac{n_o n_e N^2}{\sqrt{n_e^2 - N^2}} k_o r_{33} V \\ &= \text{Im}(h_r) \cdot r_{33}\end{aligned}\quad (2.31)$$

and

$$\begin{aligned}\frac{\delta b}{b} &= \left(\frac{n_o^4}{\sqrt{n_o^2 - N^2}} + \frac{n_o^3}{n_e} \sqrt{n_e^2 - N^2}\right) k_o \gamma s_{33} V + \frac{n_o n_e N^2}{\sqrt{n_e^2 - N^2}} k_o s_{33} V \\ &= -\text{Im}(h_s) \cdot s_{33}.\end{aligned}\quad (2.32)$$

For $n_o \approx n_e \equiv n$ (isotropic), Eqs. 2.31 and 2.32 further reduce to

$$\delta\psi_{sp} = \frac{n^2 N^2}{\sqrt{n^2 - N^2}} (1 - \gamma) k_o r_{33} V = \text{Im}(h_r) \cdot r_{33}\quad (2.33)$$

and

$$\frac{\delta b}{b} = \left(\frac{2n^4 - n^2 N^2}{\sqrt{n^2 - N^2}} \gamma + \frac{n^2 N^2}{\sqrt{n^2 - N^2}}\right) k_o s_{33} V = -\text{Im}(h_s) \cdot s_{33}.\quad (2.34)$$

Equations 2.31 and 2.33 are identical with those reported previously [14, 18], but our Eqs. 2.32 and 2.34 describe the electrochromic effect somewhat differently from

that reported in Refs. [16], [53], and [55]. In Refs. [53] and [55], the ellipsometric parameter $\tan \Phi (= |r_p/r_s|)$ was used to calculate the electrochromic effect, but $\delta|r_s| = 0$ was assumed. In Ref. [16], the variation of complex phase retardation was introduced to estimate the electrochromic effect in the simple model, but their formula for the electrochromic effect is equivalent to that in Refs. [53] and [55] where $\delta|r_s| = 0$ is assumed.

2.2.4 Rigorous model

In this section, we use rigorous expressions for the s - and p - reflectance based on multilayer stack reflectivity model (MSRM) [16, 17, 59]. In the case of a thin film on a TCO-glass substrate, the first reflection off the glass is blocked from reaching the detector [14], as is a second-pass beam resulting from reflection of the first pass on its way out at the glass/air interface back into the polymer and out again. This eliminates reflection fluctuations from the glass layer. Greater care is required to block these beams at high and low angles of incidence, because the transverse separation between reflections becomes narrow at these angles of incidence [60]. If the glass is sufficiently thick, it is possible to block the gross multiple reflections efficiently, i.e., the first reflection off the glass and the second, third, etc. passes resulting from back-reflection off the glass/air interface as shown in Fig. 2.1, but it is generally not possible to avoid the multiple reflections inside a thin polymer film. These multiple reflections inside the film are accounted for in the rigorous model but not in the simple model. Assuming that the incident light is a plane wave,

the iteration of the Airy formula [61] gives the reflection coefficient in the whole multilayered sample as shown in Fig.2.3(b). As given in Refs.[16] and [17], the resulting expressions for r_s and r_p have the form

$$r = \frac{r_{23} + \hat{r}_{34}e^{2i\beta_3d_3}}{1 + r_{23}\hat{r}_{34}e^{2i\beta_3d_3}} \Leftarrow \hat{r}_{34} = \frac{r_{34} + \hat{r}_{45}e^{2i\beta_4d_4}}{1 + r_{34}\hat{r}_{45}e^{2i\beta_4d_4}} \Leftarrow \hat{r}_{45} = \frac{r_{45} + r_{56}e^{2i\beta_5d_5}}{1 + r_{45}r_{56}e^{2i\beta_5d_5}}, \quad (2.35)$$

where \Leftarrow represents a substitution and we have omitted the s - and p - subscripts to prevent the notation from becoming unduly cumbersome. In Eq.2.35 the s - or p - propagation constant β_j in each layer j is defined in Eq.2.23 and the corresponding reflection coefficient from layer j to k is given by

$$r_{ij} = \frac{Z_k - Z_j}{Z_k + Z_j} \quad (2.36)$$

with the s - and p - wave impedances [62] of each layer given by

$$Z^s = \frac{1}{\sqrt{\tilde{n}_o^2 - N^2}}, Z^p = \frac{1}{\tilde{n}_o} \sqrt{1 - \left(\frac{N}{\tilde{n}_e}\right)^2}. \quad (2.37)$$

In principle, these reflection coefficients should be multiplied by two transmittances, t_{12} and t_{21} , at the air-glass interface [17], but in practice these terms do not contribute to the calculation of $\delta\Psi_{sp}$ and $\delta B/B$ in our analysis. We derive expressions for the functions H_r and H_s that appear in Eq.2.20. Performing the operations described in Eq.2.20, we have

$$H_r = -\frac{V}{2d_4} \left[\frac{\gamma}{r_s} \frac{\partial r_s}{\partial \tilde{n}_o} \tilde{n}_o^3 + \gamma \left(\frac{1}{r_p} \frac{\partial r_p}{\partial \tilde{n}_o} \tilde{n}_o^3 \right)^* + \left(\frac{1}{r_p} \frac{\partial r_p}{\partial \tilde{n}_e} \tilde{n}_e^3 \right)^* \right] \quad (2.38)$$

and

$$H_s = -\frac{V}{2d_4} \left[\frac{\gamma}{r_s} \frac{\partial r_s}{\partial \tilde{n}_o} \tilde{n}_o^3 - \gamma \left(\frac{1}{r_p} \frac{\partial r_p}{\partial \tilde{n}_o} \tilde{n}_o^3 \right)^* - \left(\frac{1}{r_p} \frac{\partial r_p}{\partial \tilde{n}_e} \tilde{n}_e^3 \right)^* \right]. \quad (2.39)$$

The detailed expressions for the function H that appear in Eqs. 2.38 and 2.39 are given in Appendix C.

2.2.5 Data analysis

At a single angle and with knowledge of the linear parameters of the sample structure, the matrix equation shown in Eq. 2.21 can simply be inverted to solve for r_{33} and s_{33} . Data at multiple angles can be analyzed by solving Eq. 2.21 for r_{33} and s_{33} at each angle and then calculating mean values for r_{33} and s_{33} . Alternatively, for experimental data at n angles of incidence, we can construct a $2n \times 2$ matrix that is derived by stacking up Eq. 2.21 to form a large matrix equation

$$\begin{pmatrix} \delta\Psi_{sp}(\theta_1) \\ \vdots \\ \delta\Psi_{sp}(\theta_n) \\ \delta B/B(\theta_1) \\ \vdots \\ \delta B/B(\theta_n) \end{pmatrix} = \begin{pmatrix} \text{Im}[H_r(\theta_1)] & \text{Re}[H_s(\theta_1)] \\ \vdots & \vdots \\ \text{Im}[H_r(\theta_n)] & \text{Re}[H_s(\theta_n)] \\ \text{Re}[H_r(\theta_1)] & -\text{Im}[H_s(\theta_1)] \\ \vdots & \vdots \\ \text{Re}[H_r(\theta_n)] & -\text{Im}[H_s(\theta_n)] \end{pmatrix} \begin{pmatrix} r_{33} \\ s_{33} \end{pmatrix} \Leftrightarrow P = M \cdot x. \quad (2.40)$$

It is easy to calculate r_{33} and s_{33} simultaneously using several matrix decomposition methods such as **QR** and singular value decomposition (SVD) to implement least squares fitting [63]. Using **QR** decomposition, the matrix M can be decomposed

into Q and R which are $2n \times 2n$ orthogonal and $2n \times 2$ upper triangular matrices, respectively and we define \hat{P} as

$$\begin{aligned} M \cdot x = P &\Rightarrow QR \cdot x = P && \text{(QR decomposition)} \\ &\Rightarrow R \cdot x = Q^T P \equiv \hat{P} && \text{(by multiplying } Q^T), \end{aligned} \quad (2.41)$$

where Q^T is the transpose matrix of Q that is identical to Q^{-1} . Taking the 2×2 upper triangular matrix from R and the 2×1 upper matrix from \hat{P} allows one to obtain x ,

$$R \cdot x = \hat{P} \Rightarrow \begin{pmatrix} R_{2 \times 2} \\ R_{low} \end{pmatrix} \cdot x = \begin{pmatrix} P_{2 \times 1} \\ P_{low} \end{pmatrix} \Rightarrow x = R_{2 \times 2}^{-1} \cdot P_{2 \times 1}, \quad (2.42)$$

where R_{low} is the $(2n - 2) \times 2$ null matrix and the magnitude of P_{low} represents the goodness of least squares fitting. Because the linear parameters (including the refractive index and thickness of the film) that determine the H functions have experimental errors associated with their measurement, it is possible to tweak their values within their experimental uncertainty range and recalculate Eqs. 2.40-2.42 to attempt to improve the fit of r_{33} and s_{33} . Reference [17] followed a more complicated approach by finding numerical fits to the rigorous expressions using the simplex method to fit the modulated intensities at three bias points as a function of angle. The interdependent variations of complex refractive indices as shown in Eqs. 2.2 and 2.3 were not taken into account although it should be included for a highly absorptive medium.

2.2.6 Uncertainty and sensitivity

We can estimate the uncertainties in r_{33} and s_{33} which result from the uncertainties in the parameters such as the index of refraction, thickness, $\delta\Psi_{sp}$, and $\delta B/B$. From Eq. 2.40, we have

$$x = M^{-1} \cdot P, \quad (2.43)$$

where x is a 2×1 matrix and each matrix component (r_{33} and s_{33}) is a function of the indices of refraction, thicknesses, $\delta\Psi_{sp}$, and $\delta B/B$. Then, the uncertainties in r_{33} and s_{33} are expressed by

$$\Delta r_{33} = \sqrt{\sum_{k=1}^l \left[\left(\Delta \xi_k \frac{\partial r_{33}}{\partial \xi_k} \right)^2 \right] + \sum_{k=1}^{2n} (M_{1,k}^{-1} \Delta P_{k,1})^2} \quad (2.44)$$

$$\Delta s_{33} = \sqrt{\sum_{k=1}^l \left[\left(\Delta \xi_k \frac{\partial s_{33}}{\partial \xi_k} \right)^2 \right] + \sum_{k=1}^{2n} (M_{2,k}^{-1} \Delta P_{k,1})^2}, \quad (2.45)$$

where l is the number of uncertain variables and ξ represents the index of refraction, extinction coefficient, or thickness. n is the number of angles of incidence and ΔP is a $2n \times 1$ matrix representing the uncertainties in each experimental value. In addition, we can define the sensitivities to r_{33} in each parameter as

$$S_\xi = \frac{\partial r_{33}}{\partial \xi}. \quad (2.46)$$

2.2.7 Results

Error

We estimate the relative error that results from using the simple model for a number of different cases. Assuming the rigorous model gives the correct value, the relative error is defined by

$$\text{Error} = \frac{r_{33}^{SM} - r_{33}}{r_{33}}. \quad (2.47)$$

For a given modulated phase and reflectivity, r_{33} and s_{33} from the rigorous model are calculated from Eq. 2.21 together with Eqs. 2.38 and 2.39, while the simple model values r_{33}^{SM} and s_{33}^{SM} are calculated from Eqs. 2.28-2.30. To evaluate the error we equate the right hand sides of Eqs. 2.21 and 2.28 and rearrange to obtain

$$\begin{aligned} \text{Error} = & \frac{\text{Im}(h_s)[\text{Im}(H_r) - \text{Im}(h_r)] + \text{Re}(h_s)[\text{Re}(H_r) - \text{Re}(h_r)]}{\text{Im}(h_r)\text{Im}(h_s) + \text{Re}(h_r)\text{Re}(h_s)} \\ & + \frac{\text{Im}(h_s)\text{Re}(H_s) - \text{Re}(h_s)\text{Im}(H_s)}{\text{Im}(h_r)\text{Im}(h_s) + \text{Re}(h_r)\text{Re}(h_s)} \frac{s_{33}}{r_{33}}. \end{aligned} \quad (2.48)$$

The result depends on the ratio s_{33}/r_{33} , but not on the absolute magnitude of either coefficient. Outside the absorption band of the polymer, $\text{Re}(h_r) = \text{Re}(h_s) = 0$ for the simple model as discussed in Section 2.2.3.

Index-matched multilayer structure

As a first example, we consider the case of a sample structure with a thick gold electrode where the index of the nonlinear film and the TCO are matched with the glass substrate under the assumption of no electrochromic effect and no optical loss

in the polymer or TCO layer. That is, $n_2 = n_3 = n_4 = 1.5$ in the absence of an applied voltage. One might think that the simple model should apply exactly in this case, but the index matching condition is broken upon application of a voltage leading to some reflectivity modulation, which is ignored in the simple model. Using $r_{23} = r_{34} = 0$ and $\hat{r}_{45} = r_{45}$ (valid for gold thicker than ~ 75 nm), the reflection coefficient in Eq. 2.35 simplifies to

$$r = r_{45} e^{2i\beta_3 d_3} e^{2i\beta_4 d_4}, \quad (2.49)$$

and the f 's and g 's in Eq. A.15 are

$$f_{234}^q = e^{2i\beta_{q3} d_3}, f_{345}^q = e^{2i\beta_{q4} d_4}, g_{345}^q = 1 - (r_{45}^q)^2 e^{2i\beta_{q4} d_4}, g_{345}^q = 1. \quad (2.50)$$

Then, H_r in Eq. 2.38 can be expressed as

$$H_r \equiv -\frac{V n_4^3}{2d_4} (K_1 \cos 2\beta_4 d_4 - iK_2 \sin 2\beta_4 d_4 + K_3) - iV n_4^3 K_4, \quad (2.51)$$

where

$$K_1 = [1 - (r_{45}^s)^2] \frac{\gamma}{r_{45}^s} \frac{\partial r_{34}^s}{\partial \tilde{n}_o} + [1 - (r_{45}^{p*})^2] \left(\frac{\gamma}{r_{45}^{p*}} \frac{\partial r_{34}^p}{\partial n_o} + \frac{1}{r_{45}^{p*}} \frac{\partial r_{34}^p}{\partial \tilde{n}_e} \right), \quad (2.52)$$

$$K_2 = [1 + (r_{45}^s)^2] \frac{\gamma}{r_{45}^s} \frac{\partial r_{34}^s}{\partial \tilde{n}_o} - [1 + (r_{45}^{p*})^2] \left(\frac{\gamma}{r_{45}^{p*}} \frac{\partial r_{34}^p}{\partial n_o} + \frac{1}{r_{45}^{p*}} \frac{\partial r_{34}^p}{\partial \tilde{n}_e} \right), \quad (2.53)$$

$$K_3 = \frac{\gamma}{r_{45}^s} \frac{\partial r_{45}^s}{\partial \tilde{n}_o} + \frac{\gamma}{r_{45}^{p*}} \frac{\partial r_{45}^{p*}}{\partial n_o} + \frac{1}{r_{45}^{p*}} \frac{\partial r_{45}^{p*}}{\partial \tilde{n}_e}, \quad (2.54)$$

$$K_4 = \gamma \frac{\partial \beta_{4s}}{\partial \tilde{n}_o} - \gamma \frac{\partial \beta_{4p}}{\partial n_o} - \frac{\partial \beta_{4p}}{\partial \tilde{n}_e}. \quad (2.55)$$

and the derivatives in these expressions are given in Eqs. A.16-A.18. The first two terms in Eq. 2.51 are due to modulation of the reflectivity at the TCO/polymer interface and contribute oscillation as the thickness d_4 of the polymer film changes, while the third term is due to modulation of the reflectivity of the polymer-gold interface and contributes an offset. The terms involving the complex quantities K_1 , K_2 , and K_3 are inversely proportional to the film thickness, but the last term involving the real quantity K_4 is independent of film thickness and equal to h_r in the simple model shown in Eq. (24). With $s_{33} = 0$, the error expression Eq. (33) takes the form

$$\text{Error} = \frac{1}{2d_4K_4} [\text{Im}(K_1) \cos 2\beta_4d_4 - \text{Re}(K_2) \sin 2\beta_4d_4 + \text{Im}(K_3)] . \quad (2.56)$$

The error percentage is plotted as a function of film thickness in Fig. 2.4. This calculation was obtained by using MATLABTM codes as given in Appendix B.1. It is notable that the error oscillates from overestimation to underestimation and the envelope decreases with increasing thickness even in the index-matched case.

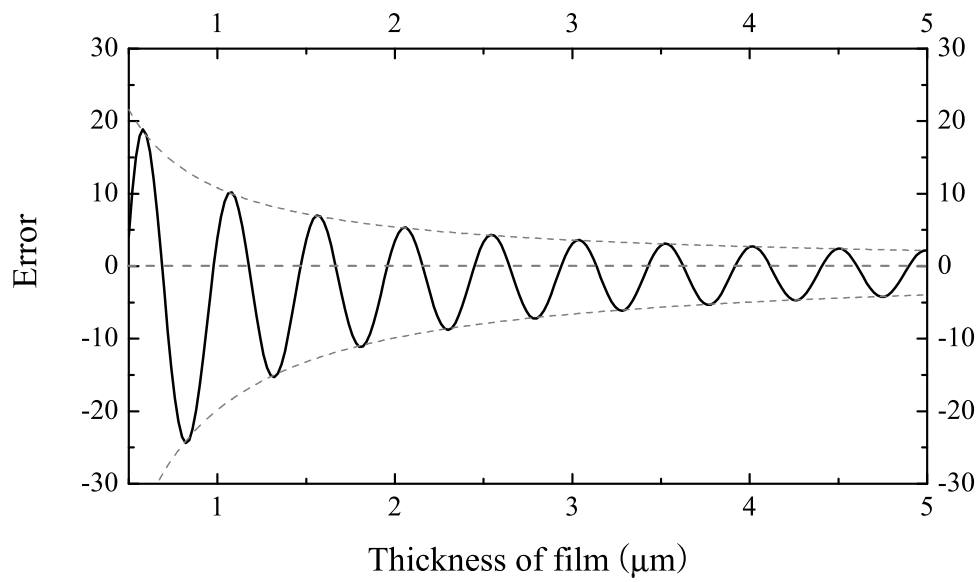


Figure 2.4: Error percentage plot for varying film thickness when the refractive indices of film and TCO are matched with glass ($n = 1.5$) at $1.3 \mu\text{m}$ wavelength. The positive and negative envelopes are proportional to $\pm 1/d_4$ with a negative offset.

Isotropic case

As additional examples, we consider the relative error for different refractive index and thickness combinations of the polymer film for selected values of complex index and thickness of ITO at four wavelengths, 0.8, 1, 1.3, and 1.55 μm and the ratio s_{33}/r_{33} is assumed to be 1 and 2 at 0.8 μm , and to be 0.1 at wavelengths 1, 1.3, and 1.55 μm for the simulation. The complex index of refraction of ITO measured by ellipsometry and the complex index of refraction of a representative doped NLO polymer film are shown in Fig. 2.5. The optical properties of ITO are strongly dependent on the manufacturing process so there are wide variations in commercial ITO properties. Free carrier absorption is usually noticeable in the near infrared range, whereas interband transitions dominate in the visible range [64]. The gold metal layer is assumed to be thicker than ~ 75 nm, because we have found that for thicknesses greater than this the thickness of the gold layer can be ignored because no light is reflected back from the gold/air interface.

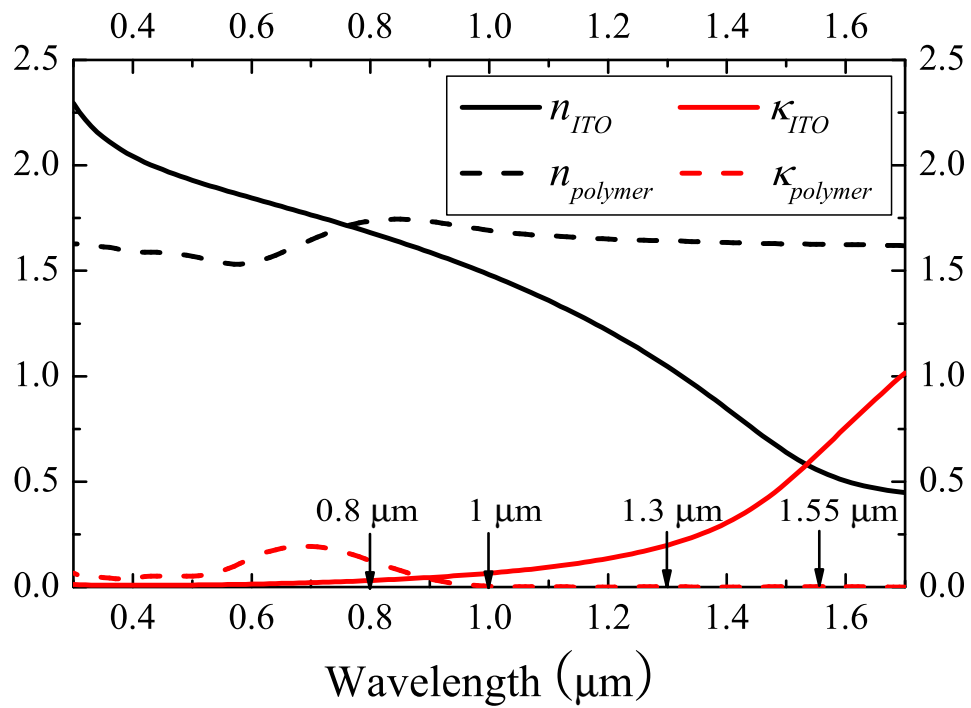


Figure 2.5: Optical properties ($n + i\kappa$) of (solid) a representative ITO (Abrisa[®]) measured by ellipsometry and (dashed) a representative polymer film selected for the simulation. (real part : black, imaginary part : red).

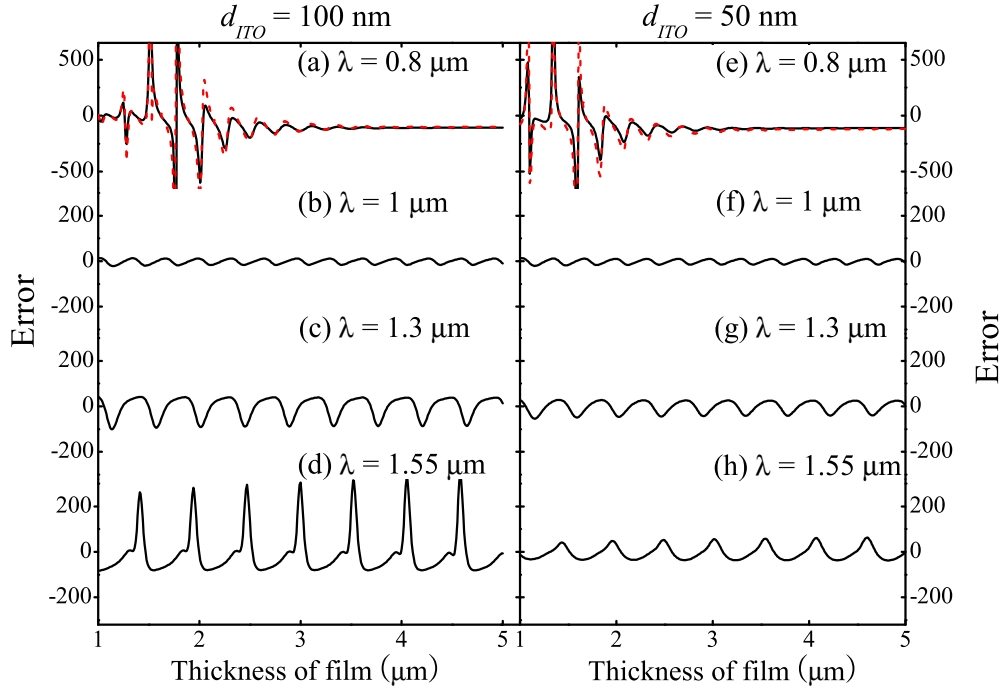


Figure 2.6: Error plots by varying the thickness of the film for fixed indices of refraction of ITO and the film and two thicknesses of ITO, 100 nm (a-d) and 50 nm (e-h) at various wavelengths and 45° angle of incidence under assumption of $\gamma = 1/3$. For plots (a) and (e), $s_{33}/r_{33} = 1$ (black solid), and $s_{33}/r_{33} = 2$ (red dashed). For the wavelengths other than $0.8 \mu\text{m}$, values of s_{33}/r_{33} between 0 and 0.1 produce curves that are indistinguishable on this scale. For (a) and (e), the errors approach -107% and -110%, respectively. For (b), (f), (c), (g), (d), and (h), the error extremes are -18% to 12%, -15% to 10%, -86% to 38%, -40% to 25%, -80% to 350%, and -37% to 63%, respectively.

Figure 2.6 shows the error plots as a function of thickness of the polymer for polymer indices of refraction shown in Fig. 2.5 (ignoring birefringence). Noteworthy is that for a given refractive index, the error cycles from positive to negative (overestimation to underestimation) as a function of film thickness when the loss of the film is negligible as shown in Figs. 2.6(b)-2.6(d) and 2.6(f)-2.6(h). This is so because increasing the thickness causes a periodic phase retardation. The error extremes also tend to increase as the wavelength increases because the ITO becomes more reflective, which enhances FP effects inside the polymer layer. Thicker ITO also tends to increase the reflectivity. When the operating wavelength is in the absorption band of the polymer film as shown in Figs. 2.6(a) and 2.6(e), the error initially fluctuates irregularly when the film is thin and finally converges to a constant negative value as the film thickness increases. This is so because propagation loss in the film has a dual effect of reducing multiple reflections as well as reducing the relative amount of phase modulation from the polymer bulk compared to the phase modulation of the light reflected from the ITO/polymer interface, which is not accounted for in the simple model. Within the absorption band, a thick film results in a constant error, but the correct value is not predictable without the rigorous analysis.

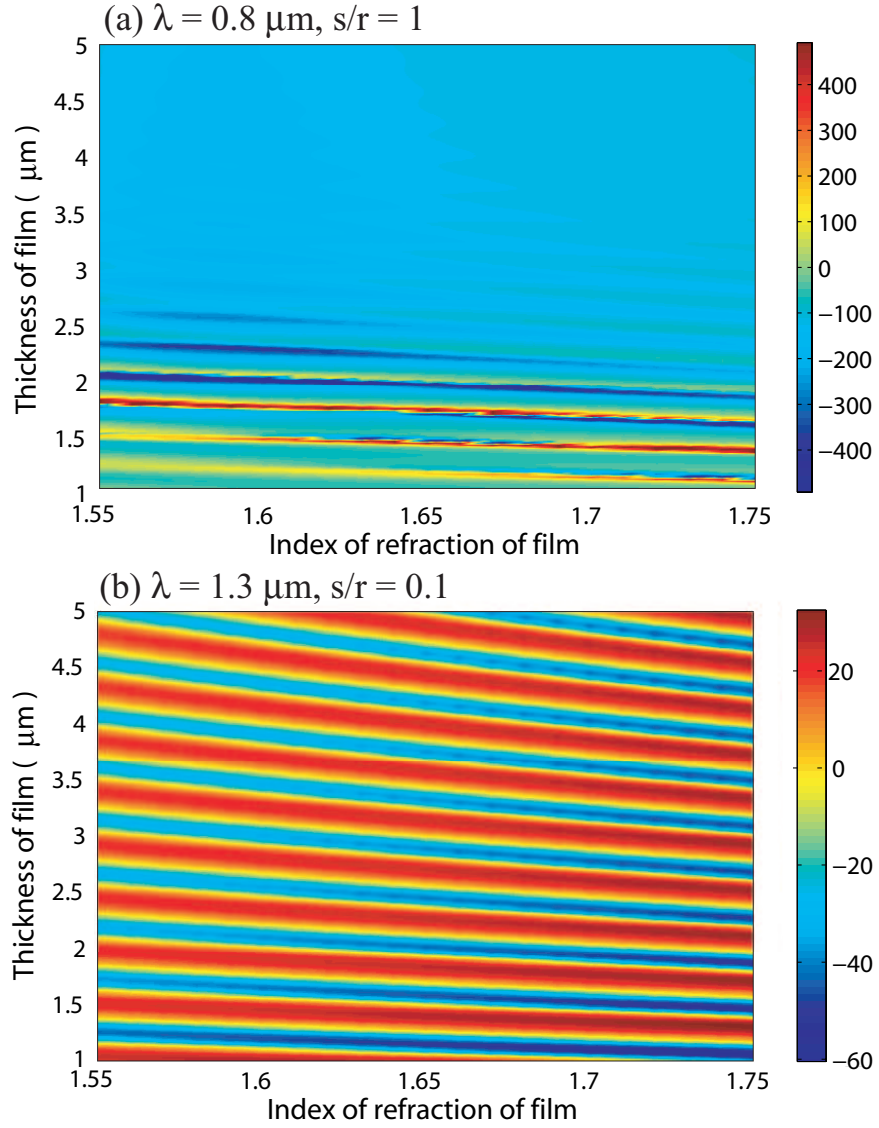


Figure 2.7: Error contour plots at (a) $\lambda = 0.8 \mu\text{m}$ and $s_{33}/r_{33} = 1$ (b) $\lambda = 1.3 \mu\text{m}$ and $s_{33}/r_{33} = 0.1$ with thickness of ITO = 100 nm, 45° angle of incidence, and $\gamma = 1/3$. Each contour plot (a) and (b) shows asymptotic and cyclic behaviors with thickness of film irrespective of index of refraction of film, respectively.

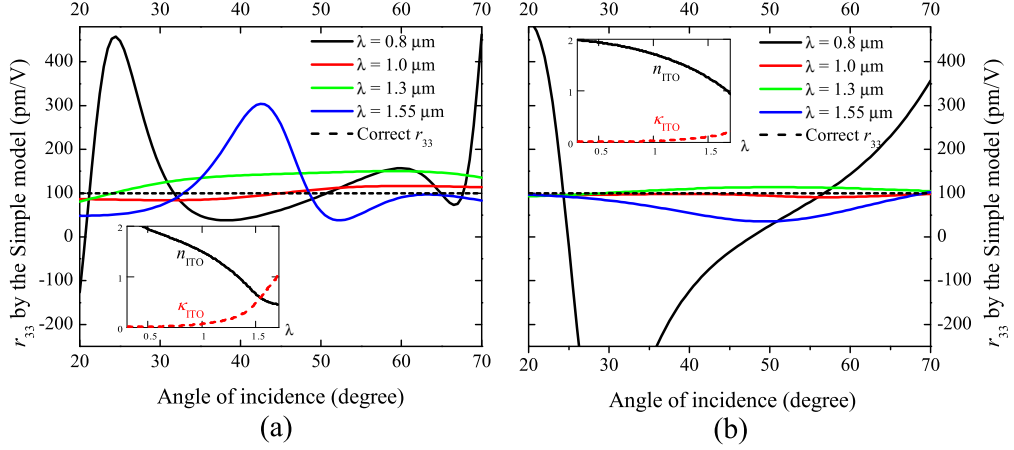


Figure 2.8: EO coefficients r_{33} calculated by the simple model at various wavelengths and angles of incidence using thickness of film and ITO, $1.4 \mu\text{m}$ and 100 nm , respectively. EO coefficient $r_{33} = 100 \text{ pm/V}$ was used for the simulation. The ratios s_{33}/r_{33} are 2 at $0.8 \mu\text{m}$ and $0.1 \mu\text{m}$ at the other wavelength. Insets in (a) and (b) show the optical properties of ITO selected for the simulation. The crossover points of n and κ of ITO are around 1.54 and $1.92 \mu\text{m}$ in (a) and (b), respectively.

The error in using the simple model versus the film thickness shows qualitatively similar behavior irrespective of the index of refraction of the film as shown in Figs. 2.7(a) and (b). We also note, contrary to earlier suggestions [16, 57], that the error from using the simple model is not in general reduced by using film thicknesses on the order of a wavelength or less.

Figure 2.8 shows simple model r_{33} values as a function of angle of incidence for two different ITO samples where the ITO for Fig. 2.8(b) is less reflective than for Fig. 2.8(a). In Fig. 2.8(a), most EO coefficients calculated by the simple model with a varying angle of incidence are far away from the correct r_{33} . Note that although the simple model EO coefficient values seem to be flat at $1.3 \mu\text{m}$ for angles of incidence between 30° and 60° , they are nevertheless overestimated by about 50%. Thus,

obtaining nearly constant simple model r_{33} values as a function of angle of incidence does not guarantee that the value is correct. When the ITO is less absorptive as shown in the inset of Fig. 2.8(b), the correct r_{33} is approached for wavelengths of 1 and $1.3\ \mu\text{m}$ because these wavelengths are in a spectral region where both polymer and ITO are more transparent.

In Figs. 2.9(a) and 2.9(b), the simulated $\delta\Psi_{sp}$ and $\delta B/B$ are plotted at wavelengths 1.3 and $1.55\ \mu\text{m}$ using the rigorous model. We notice that the $\delta\Psi_{sp}$'s are quite different from those of the simple Teng-Man method [53, 55]. Also, $\delta B/B$ at a wavelength of $1.55\ \mu\text{m}$ passes through 0 at several angles of incidence. Thus, measuring $\delta B/B = 0$ at a fixed angle of incidence does not mean that there is no electrochromic effect, contrary to the suggestion in Ref. [16]. We observe that $\delta\Psi_{sp}$ and $\delta B/B$ fluctuate more at $1.55\ \mu\text{m}$ than at $1.3\ \mu\text{m}$ because of the more reflective ITO.

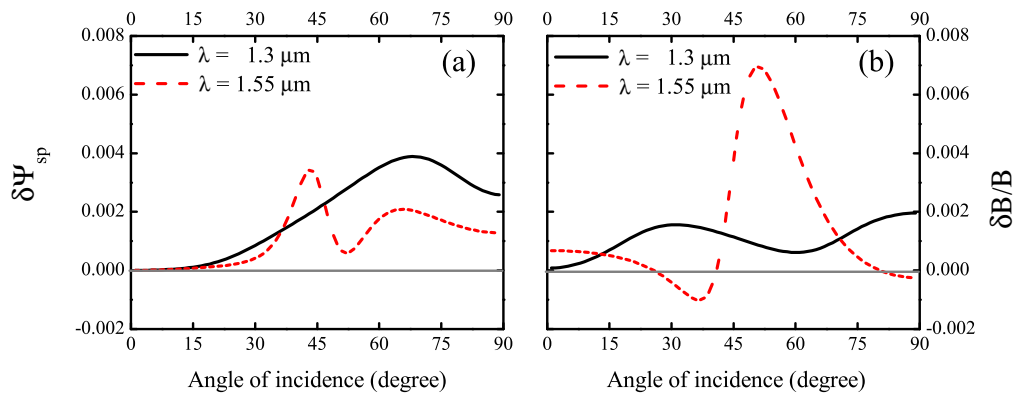


Figure 2.9: (a) $\delta\Psi_{sp}$ and (b) $\delta B/B$ versus angle of incidence at wavelengths 1.3 and $1.55\ \mu\text{m}$. The ratio $s_{33}/r_{33} = 0.1$ and film thickness = $1.4\ \mu\text{m}$ were used at both wavelengths for the ITO properties shown in Fig. 2.5.

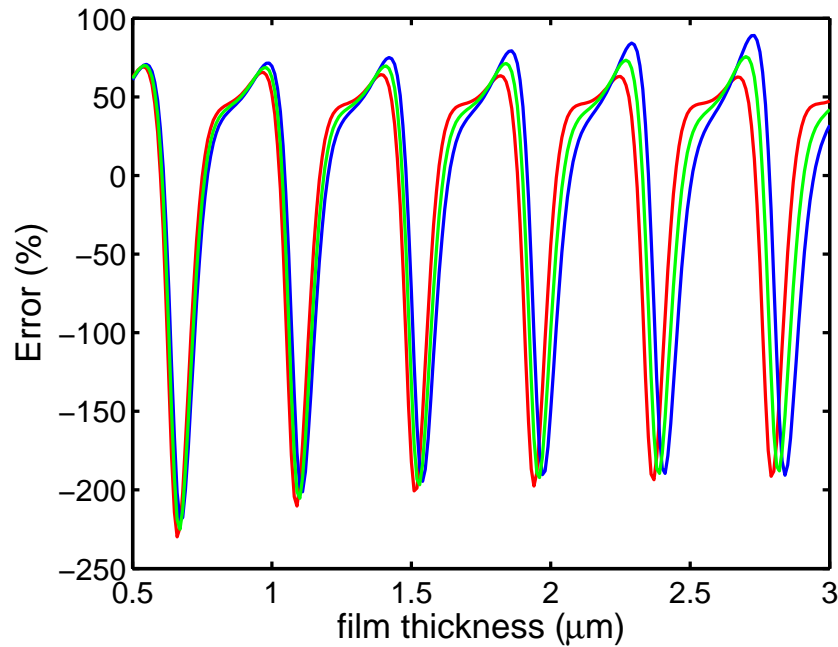


Figure 2.10: Representative error profiles in anisotropic case using 150 nm thick ITO at $1.3 \mu\text{m}$ wavelength. Red, green, and blue lines are for the birefringence $\Delta n \equiv n_e - n_o$ of 0, 0.03, 0.06, and 0.09, respectively.

Anisotropic case

Poled polymer thin film is generally anisotropic as discussed in Section 1.2.1. In this case, the error is somewhat different from that in the isotropic case. Figure 2.10 shows error percentages with different birefringence, 0, 0.03, 0.06, and 0.09 at $1.3 \mu\text{m}$ wavelength. The error profiles look quite similar with one another, but we notice that there can be a drastic change in error percentage by an introduction of birefringence when the film thickness is in the sharp edge of the error curves (steep slope in curves).

In an isotropic case, we have shown that the estimate of error can oscillate from overestimation to underestimation and the envelope of the error can converge with increasing thickness. However, in an anisotropic case, the estimate of error

shows a beating behavior with increasing thickness as shown in Fig. 2.11.

Thick films

EO polymer films can be used in optical rectification and electro-optic sensing to generate and detect terahertz (THz) radiation, respectively. The THz amplitude obtained from the polymer increases with the film thickness [65]. When the film is thick, the small change of angle of incidence can make a large phase change, which results in large variation of $\delta\Psi_{sp}$ with a varying angle of incidence. Figure 2.12 shows representative $\delta\Psi_{sp}$'s with three different film thicknesses at wavelength $1.3\ \mu\text{m}$. The $\delta\Psi_{sp}$ with $1\ \mu\text{m}$ thick film is smooth, whereas that with $50\ \mu\text{m}$ has many oscillations throughout the range of angles of incidence. The oscillations become dense as the

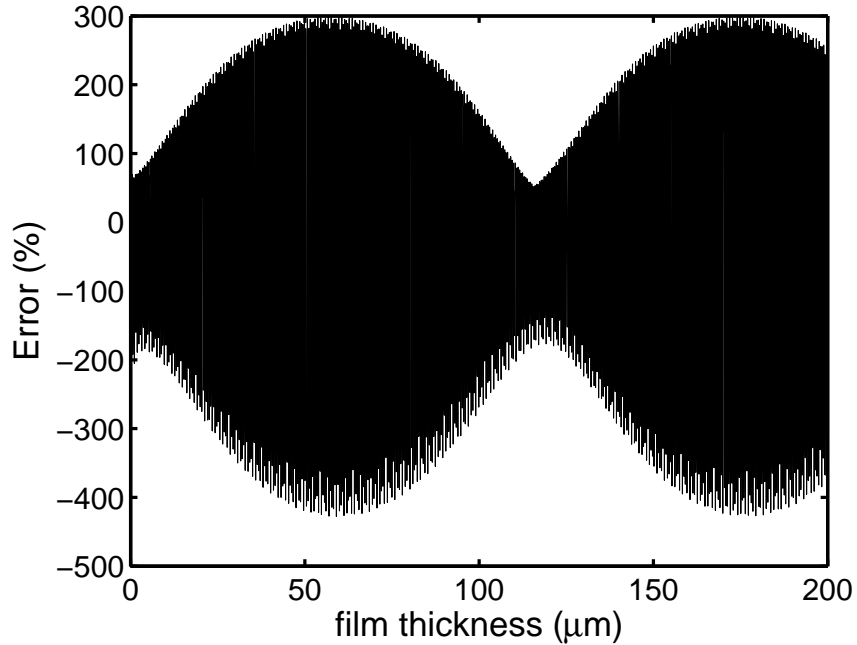


Figure 2.11: Representative error percentage in anisotropic case at $1.3\ \mu\text{m}$ wavelength. The error shows a beating behavior unlike asymptotic one as shown in the isotropic case.

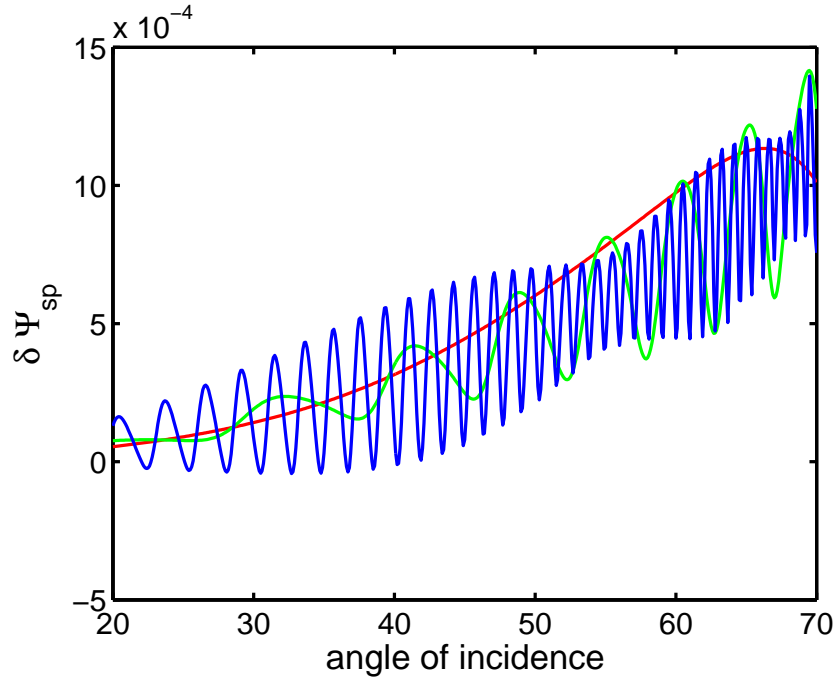


Figure 2.12: Representative $\delta\Psi_{sp}$ with three different film thicknesses at $1.3\ \mu\text{m}$ wavelength. Red, green, and blue lines are for the film thickness of 1, 10, $50\ \mu\text{m}$, respectively.

angle of incidence approaches 90° , because the slight change of angle of incidence make a large phase retardation with increasing angle of incidence. For the rigorous Teng-Man analysis, multi-angle Teng-Man data is necessary for a better estimation of the EO coefficient. Therefore, a large number of data points are needed for the fit of $\delta\Psi_{sp}$. Thick films make the rigorous Teng-Man analysis difficult.

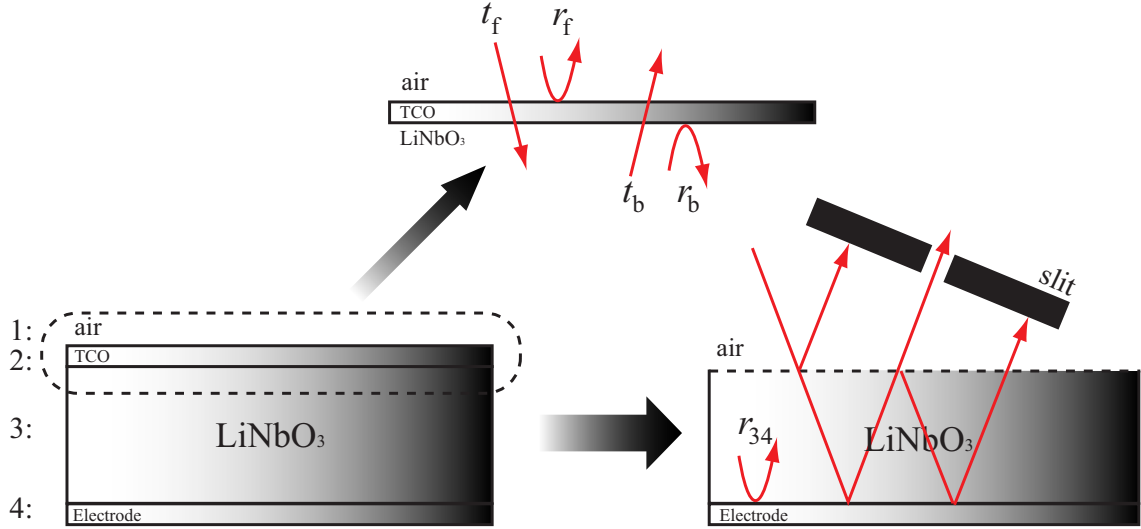


Figure 2.13: Smith's technique is applied to air/TCO/LiNbO₃ interface which can be considered as a single interface.

2.3 Thick z -cut LiNbO₃ crystal for validation of Teng-Man method

2.3.1 Rigorous analysis

As stated in Section 2.1, Shuto and Amano measured EO coefficients of a 0.5 mm thick z -cut LiNbO₃ crystal using the simple Teng-Man method and found agreement with standard values [18]. In addition, they also presented a mathematical expression for r_{33} that includes the effect of birefringence. For this reason, z -cut LiNbO₃ has often been adopted as a standard to verify the Teng-Man method. Here we examine the suitability of using z -cut LiNbO₃ to validate a Teng-Man setup for measuring EO coefficient of thin films [66].

Using Smith's technique [60, 67], the air/TCO/LiNbO₃ interface can be reduced to a single virtual interface characterized by reflection and transmission coefficients r_f , r_b , t_f , and t_b in the forward and backward directions, as shown in Fig. 2.13. The advantage of this technique is to be able to isolate any single or mul-

tilayer combination. Then, as usual, the total reflection coefficient at the sample is represented by the infinite sum

$$r = r_f + t_f t_b r_{34} e^{2i\beta_3 d_3} + t_f t_b r_b r_{34}^2 e^{4i\beta_3 d_3} + \dots, \quad (2.57)$$

where r_{34} and β_3 are given in Eq. 2.36 and in Eqs. A.3 and A.4, respectively. The reflection and transmission coefficients at the virtual interface are defined as

$$r_f = \frac{r_{12} + r_{23} e^{2i\beta_2 d_2}}{1 + r_{12} r_{23} e^{2i\beta_2 d_2}}, \quad (2.58)$$

$$r_b = \frac{r_{21} + r_{32} e^{2i\beta_2 d_2}}{1 + r_{21} r_{32} e^{2i\beta_2 d_2}}, \quad (2.59)$$

$$t_f = \frac{t_{12} t_{23} e^{i\beta_2 d_2}}{1 + r_{12} r_{23} e^{2i\beta_2 d_2}}, \quad (2.60)$$

$$t_b = \frac{t_{21} t_{32} e^{i\beta_2 d_2}}{1 + r_{21} r_{32} e^{2i\beta_2 d_2}}. \quad (2.61)$$

If the beam size is focused by a lens or narrowed by an aperture, the first term and the multiple reflection terms in Eq. 2.57 can be blocked by a slit as shown in Fig. 2.13, so only the second term contributes and the reflectance is

$$r = t_f t_b r_{34} e^{2i\beta_3 d_3}. \quad (2.62)$$

Using this reflectance and Eq. 2.19, the imaginary part of $\delta\tilde{B}/\tilde{B}$, that is, $\delta\Psi_{sp}$ is given by

$$\delta\Psi_{sp} = \text{Im} \left(\frac{\delta\tilde{B}}{\tilde{B}} \right) = \text{Im} \left(\frac{\delta C}{C} \right) + 2(\delta\beta_{3s} - \delta\beta_{3p})d_3. \quad (2.63)$$

where $C = t_f^s t_b^s r_{34}^s (t_f^p t_b^p r_{34}^p)^*$. Note that the last term in the Eq. 2.63 is identical

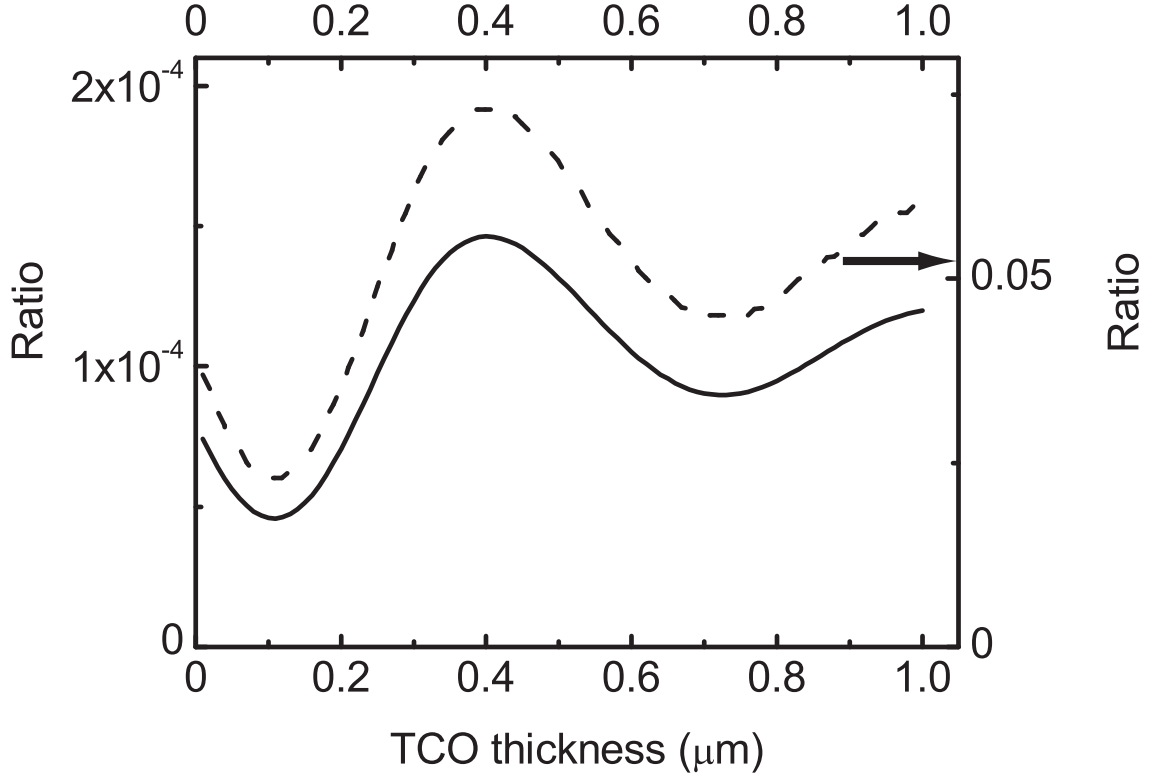


Figure 2.14: Solid and dashed lines are the ratios of $|\text{Im}(\delta C/C)|$ to $|2(\delta\beta_{3s} - \delta\beta_{3p})d_3|$ when the LiNbO_3 is 0.5 mm and 1 μm thick, respectively.

to the simple model expression as given in Eq. 2.25. This means that the simple Teng-Man analysis works only if $\delta C/C$ is negligible compared to $2(\delta\beta_{3s} - \delta\beta_{3p})d_3$.

2.3.2 Results

It turned out that it is difficult to show in general whether $\text{Im}(\delta C/C)$ or $2(\delta\beta_{3s} - \delta\beta_{3p})d_3$ is dominant. So we pick a particular example and calculate $\text{Im}(\delta C/C)$ and $2(\delta\beta_{3s} - \delta\beta_{3p})d_3$ for a selected index of refraction of TCO to see if the simple Teng-Man analysis works.

Figure 2.14 shows the ratio of $|\text{Im}(\delta C/C)|$ to $|2(\delta\beta_{3s} - \delta\beta_{3p})d_3|$ when the LiNbO₃ is 0.5 mm and 1 μm thick, respectively. We note that in the case of thick LiNbO₃, $\text{Im}(\delta C/C)$ is negligible compared to $2(\delta\beta_{3s} - \delta\beta_{3p})d_3$, which means that the simple Teng-Man method works well. When the LiNbO₃ is only 1 μm thick (although this is not the real case), the ratio is still much less than 1. However, it doesn't mean that the simple Teng-Man method can be applied to the thin NLO film. We are reminded that we only included the second reflection term in Eq. 2.57 for this calculation, but for the thin LiNbO₃ the higher order reflections must be included. In other words, as long as only the second reflection term can be detected without any interference with the neighboring reflections, the simple Teng-Man method will work well even in the case of thin LiNbO₃ film, but in practice, these neighboring reflections cannot be blocked.

We found that the modulation of transmission at the virtual interface and of the reflection at the electrode are small compared to that resulting from propagation through the thick LiNbO₃ layer. Equation 2.63 can be approximately reduced to

$$\text{Im} \left(\frac{\delta \tilde{B}}{\tilde{B}} \right) \approx 2(\delta\beta_{3s} - \delta\beta_{3p})d_3. \quad (2.64)$$

If the input laser beam size is large compared to the thickness of LiNbO₃, then it is impossible to separate each reflection to detect the second reflection only. In this case, the multiple reflections are similar to those of a thin film so the rigorous model must be applied. However, the reflectance then fluctuates rapidly as a function of incident angle because the thickness of the LiNbO₃ is much larger than the operating

wavelength, which makes using the rigorous analysis unless data can be taken at a very fine angular resolution.

2.4 Gaussian beam optics

2.4.1 Theory

Both the simple and rigorous models assume an infinite plane wave, but the actual experimental setup uses a laser with a finite Gaussian beam profile. For a Gaussian beam analysis, the single virtual layer, air/TCO/NLO film as shown in Fig. 2.13 is considered again [66]. The electric field of the incident beam has the transversal dependence

$$E_i(r, z) = E_o \frac{w_o}{w(z)} \exp\left(\frac{-r^2}{w^2(z)}\right) \exp\left(-ikz - ik \frac{r^2}{2R(z)} + i\zeta(z)\right), \quad (2.65)$$

where $r = x^2 + y^2$ and w_o is the width of the beam waist. The variation of the spot size is given by

$$w(z) = w_o \sqrt{1 + \left(\frac{z}{z_o}\right)^2}, \quad (2.66)$$

where

$$z_o = \frac{\pi w_o^2}{\lambda}, \quad (2.67)$$

which is called the Rayleigh range. $R(z)$ is the radius of curvature of the wavefronts comprising the beam. Its value as a function of position is

$$R(z) = z \left[1 + \left(\frac{z_o}{z}\right)^2\right]. \quad (2.68)$$

Assuming that the beam waist is located at $z = 0$ of the virtual layer interface as

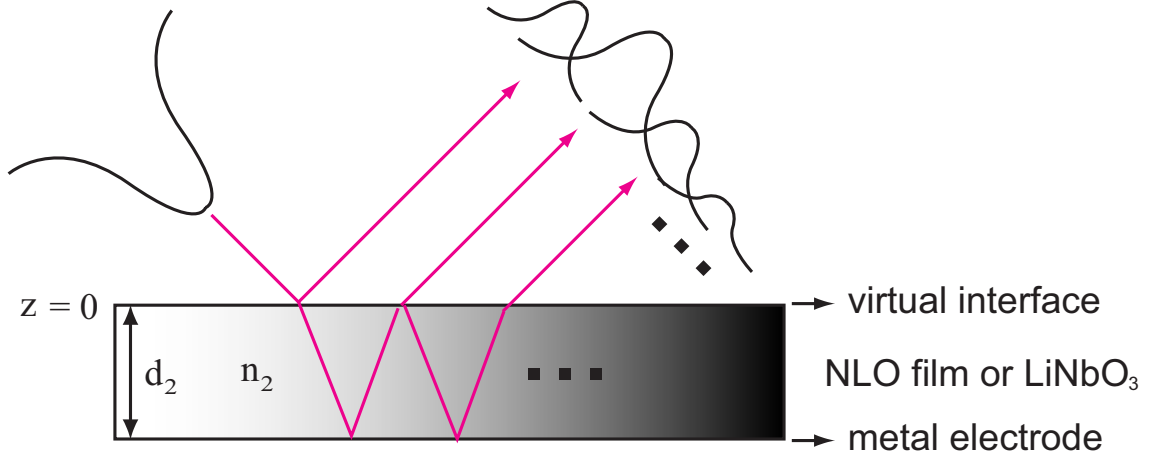


Figure 2.15: Simplified multilayer structure using a virtual interface.

shown in Fig. 2.15, the total electric field of the reflected light is represented by the infinite sum

$$\begin{aligned}
 E_t(x, y) = & E_o r_f \exp\left(\frac{-(x^2 + y^2)}{w_o^2}\right) \\
 & + E_o \sum_{p=1}^{\infty} A_p \frac{w_o}{w(p)} \exp(-ipk_o\beta) \exp\left(-\frac{x^2 + (y - p\Delta y)^2}{w(p)^2}\right) \quad (2.69) \\
 & \exp\left[i \arctan\left(\frac{p\beta}{z_o}\right)\right] \exp\left[-i \frac{\pi}{\lambda} \frac{x^2 + (y - \Delta y)^2}{p\beta + \frac{z_o^2}{p\beta}}\right],
 \end{aligned}$$

where $A_p = t_f t_b r_b^{p-1} r_{34}^p$ and $\beta = 2n_2 d_2 \sqrt{n_2^2 - N^2}$.

2.4.2 Results

When the beam waist is small compared to the thickness of the sample and all reflections are collected at the detector (we observed that the first two terms are dominant in Eq. 2.57), the reflectance and its phase are quite different from those of the plane wave analysis. As one might expect, the reflectance of the Gaussian beam converges to that predicted by the infinite plane wave analysis as the beam

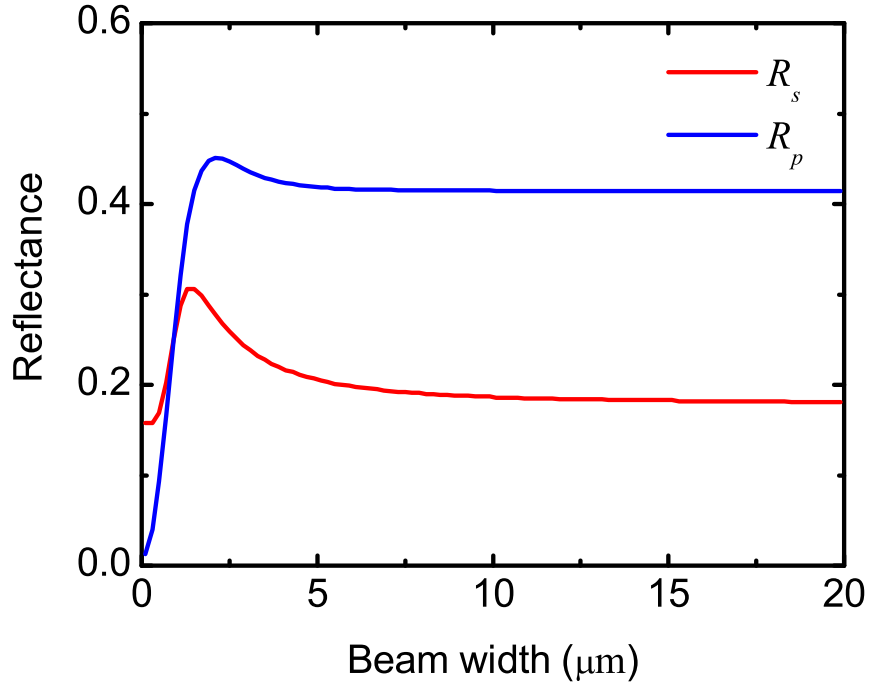


Figure 2.16: Calculated reflectances of the s (red)- and p (blue)- wave of a Gaussian beam versus beam width at 45° angle of incidence.

waist increases. When the beam waist is less than the thickness of the NLO film, there are severe deviations of the optical bias curve and modulated intensity from a plane wave analysis. Figure 2.16 shows calculated reflectances of the s - and p - wave of a Gaussian beam as a function of beam waist at a 45° angle of incidence. The refractive indices, n_o , n_e , and thickness of NLO film we used in Fig. 2.16 are 1.6, 1.65, and $2\ \mu\text{m}$, respectively. We also observed that reflectance deviations at low beam waist increase with the angle of incidence from a low angle to 45° because the transverse separations between reflected beams also increase.

The required beam waist is recommended to be larger than at least ~ 10 times the thickness of the film so that the measurement should not be affected by a focused Gaussian beam causing deviations from the plane wave analysis.

As stated above, in the case of a thick sample such as LiNbO_3 and a glass substrate in a Teng-Man sample, the beam should be narrow enough to resolve the second reflection. The large beam waist generates rapid reflectance fluctuations with angle because of the large thickness to wavelength ratio. In our setup, an aperture was used in front of the sample to make a small beam size while maintaining beam divergence as well as a large beam waist and blocking unnecessary reflections as shown in Fig. 2.13. When we used a lens with a 10 cm focal length instead of an aperture, the beam waist was $24 \mu\text{m}$ which is still large compared to the film thickness. In this case, we needed another lens after the sample because the reflected beam diverged too much before reaching the detector.

ATTENUATED TOTAL REFLECTION METHOD

3.1 Introduction

3.1.1 Prism coupling technique

We have discussed both the reflection and transmission of light in a multilayered structure for the rigorous Teng-Man analysis. In addition, a multilayered structure can support confined electromagnetic wave propagation for the proper refractive index relationships [68, 69]. These modes of wave propagation are called guided modes and the structures that support guided waves are called waveguides. For many years, guided waves in integrated optics have led to numerous new applications in the laser and optical communication fields [70]. In earlier experiments, coupling light into waveguides had been studied when the light was incident to the edge of the waveguide [71]. This method was usually limited by multimode excitation and excessive scattering at the edge of the junction. A grating on the waveguide and tapered film light wave coupler are also means for coupling light [72, 73]. The prism coupling technique has been widely used for evaluating the propagation characteristics of waveguides as well as for coupling light in and out [74, 75, 76]. It

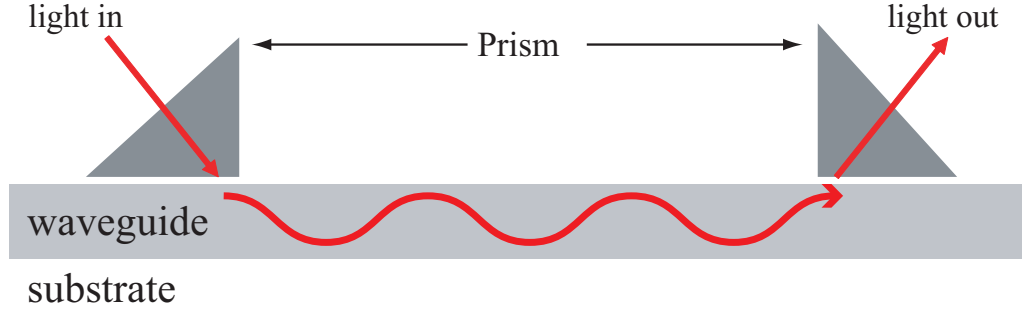


Figure 3.1: The prism coupling technique for coupling light in and out.

makes use of a high-refractive-index prism placed in close proximity to a waveguide as shown in Fig. 3.1. The laser light is incident at a certain angle in order to have a total reflection at the prism/air interface, and then an evanescent wave is generated in the air gap. When its wave vector matches with one of the propagation constants of the waveguide modes, the evanescent field is coupled, so called *optical tunneling*, into the waveguide and the reflected light off the prism/air interface is drastically attenuated. A practical application of the prism coupling technique is characterization of the optical properties of thin film, bulk material and optical waveguide. These properties include the anisotropic index of refraction, the thickness, and the propagation loss.

3.1.2 ATR for EO measurement

ATR is another method for EO measurement [46, 47, 77]. For sample preparation, the NLO polymer can be coated directly on a metal-coated prism [77] or onto a free-standing substrate which is then pressed against the prism using index-matching fluid [46]. When an EO sample is designed for Teng-Man measurement, it is usually not appropriate to apply the ATR method directly because the metal electrode

layer, normally Au, can be too thick for the light to be coupled into the NLO film layer. However, simply taking the metal electrode off the Teng-Man sample makes it feasible to use the ATR method with a metal-coated high index prism [48]. It enables measurement of r_{13} and r_{33} separately without an assumption for the ratio of r_{13} to r_{33} as required in the Teng-Man method. In addition, the anisotropic indices of refraction (n_o and n_e) and the thickness of the film can be determined in the ATR measurement when the thin film waveguide supports two or more propagation modes. However, the film thickness estimated from the simple calculation by ignoring the TCO layer may be quite different from the actual one.

The refractive indices are crucial for the determination of EO coefficients. The film thickness is particularly important because the calculation of EO coefficients is directly proportional to the thickness. However, the film thickness estimated from the simple calculation by ignoring the TCO layer may be quite different from the actual one. A more accurate determination of the film thickness can be achieved by considering a multilayer waveguide structure instead of the three-layer approximation to the waveguide structure air/film/glass. This treatment is also applied to the determination of $\partial N/\partial n$, the change of the effective index N with respect to the EO-induced change in refractive indices, for better estimation of EO coefficients.

3.1.3 Outline of the chapter

In this chapter, we re-evaluate the ATR method for the measurement of the EO coefficients of poled polymer thin films based on multilayer structure containing a

transparent conducting oxide layer. We review planar waveguide theory in an asymmetric anisotropic three-layer or multilayer waveguide structure and derive closed-form expressions of $\partial N/\partial n$ and $\partial N/\partial d$ from the three-layer waveguide structure.

A more accurate determination of the film thickness can be achieved by considering a multilayer waveguide structure containing TCO layer (glass/TCO/film/air) instead of a three-layer approximation to the waveguide structure (glass/film/air) [78]. This treatment is also applied to the determination of $\partial N/\partial n$, the change of effective index N with respect to the EO-induced change in the refractive index n for better estimation of EO coefficients. We present mathematical formulations for the ATR analysis based on the multilayer structures. The four-layer waveguide model (WGM) analysis is compared with the three-layer waveguide model to show that the three-layer waveguide model analysis applied to a single mode NLO film can result in a large error in the determination of the EO coefficients. The relative error in r_{33} using both the three-layer and four-layer waveguide models shows an asymptotic behavior with increasing film thickness, while the error from the simple Teng-Man analysis shows a large cyclic variation. We also discuss the accuracy of $\partial N/\partial n$ at higher order modes.

3.2 Theory and analysis

3.2.1 Principle of ATR

As shown in Fig. 3.2, a sample consisting an NLO film spun on TCO-coated glass substrate is pressed against the bottom of the high-index prism by the coupling head which is controlled by pneumatic pressure. In reality, the air gap is not uniform because the sample is bent as illustrated in the small inset of Fig. 3.2. Assuming that the air gap is uniform, we can apply the Fresnel equation to simulate the reflection coefficient. The *s*- or *p*- polarized light is incident to the prism and the light reflected from the prism/air interface makes an evanescent wave in the air gap between the prism and the NLO film when the internal angle θ_p is equal to or larger than the critical angle for total internal reflection. The evanescent wave is coupled into a slab waveguide (NLO film) and travels along the waveguide only at certain angles of incidence which satisfy the guided mode condition. The intensity reflected from the prism/air interface at these incident angles drastically drops. One can estimate the anisotropic indices of refraction and the thickness of the film from the angles of incidence giving rise to each pair of guided modes.

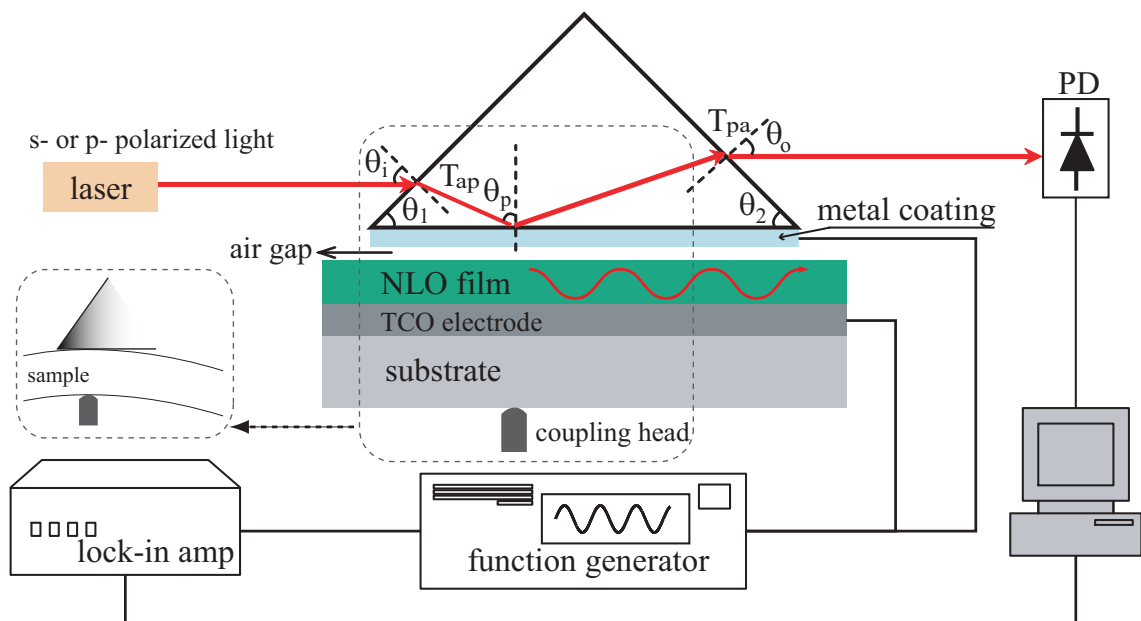


Figure 3.2: Schematic of the experimental ATR setup.

The intensities of multilayer stack reflectivity (MSR) R_{dc} are collected at discretely varying angles of incidence. The modulated data set R_m is also obtained by applying an AC voltage $V \sin \omega t$ to the sample and using a lock-in amplifier to record the modulation of R_{dc} for a given angle of incidence. R_{dc} can be expressed as

$$R_{dc}(\theta_i, n_o, n_e, d_f) = I_o T_{ap}(\theta_i) R(\theta_i, n_o, n_e, d_f) T_{pa}(\theta_o), \quad (3.1)$$

where I_o is the incident intensity and T_{ap} , T_{pa} , and R are the transmissivities at the entrance air/prism and exit prism/air interfaces and reflectivity at the prism/metal interface including the air gap and multilayered sample structure. When a DC voltage V is applied to the sample, a small change in the refractive index and thickness induced by a DC voltage V generates a slightly different MSR curve $R_{dc}(V)$.

We define $N = n_p \sin \theta_p$ where n_p is the refractive index of the prism. The relationships between N and $\theta_{i,o}$ are given by

$$\sin \theta_i = N \cos \theta_1 - \sqrt{n_p^2 - N^2} \sin \theta_1, \quad (3.2)$$

$$\sin \theta_o = N \cos \theta_2 - \sqrt{n_p^2 - N^2} \sin \theta_2. \quad (3.3)$$

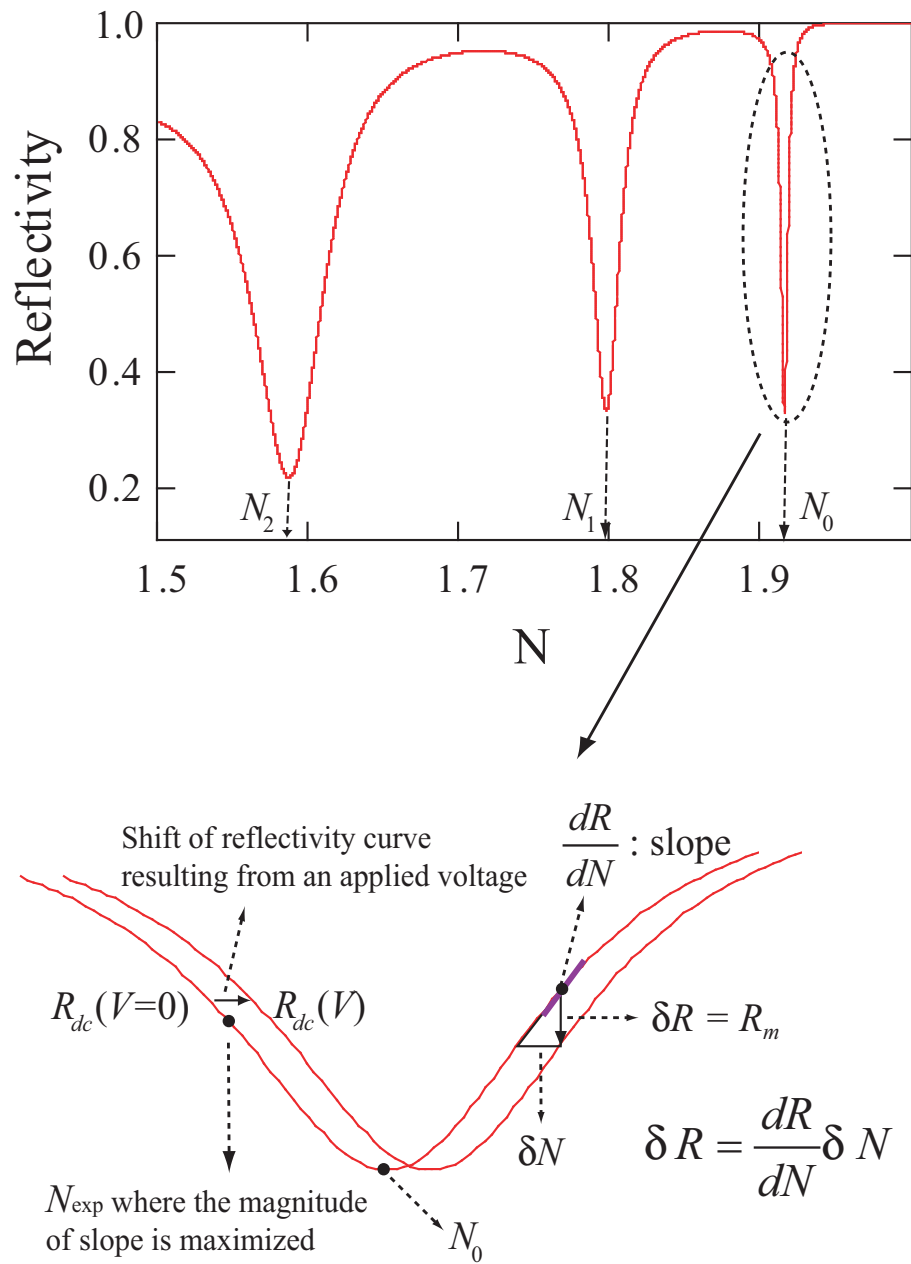


Figure 3.3: Reflectivity versus N . A DC voltage V generates a slight shift of reflectivity curve.

We assume that the new MSR curve $R_{dc}(V)$ is shifted slightly in N from $R_{dc}(V = 0)$ as shown in Fig. 3.3. Then, by expanding to 1st order, we have

$$R_m^s = \frac{\partial R_{dc}^s}{\partial V} \delta V = \frac{\partial R_{dc}^s}{\partial N^s} \frac{\partial N^s}{\partial n_o} \delta n_o + \frac{\partial R_{dc}^s}{\partial N^s} \frac{\partial N^s}{\partial d_f} \delta d_f, \quad (3.4)$$

$$R_m^p = \frac{\partial R_{dc}^p}{\partial V} \delta V = \frac{\partial R_{dc}^p}{\partial N^p} \frac{\partial N^p}{\partial n_o} \delta n_o + \frac{\partial R_{dc}^p}{\partial N^p} \frac{\partial N^p}{\partial n_e} \delta n_e + \frac{\partial R_{dc}^p}{\partial N^p} \frac{\partial N^p}{\partial d_f} \delta d_f, \quad (3.5)$$

where R_{dc}^s and R_{dc}^p are MSR curves and R_m^s and R_m^p are modulated reflectivities for the TE and TM cases, respectively. The piezoelectric coefficient p is defined by

$$\delta d_f = d_f p E_3. \quad (3.6)$$

Assuming no piezoelectric effect, that is, $\delta d_f = 0$, we can write

$$R_m^s = \frac{\partial R_{dc}^s}{\partial N^s} \frac{\partial N^s}{\partial n_o} \delta n_o, \quad (3.7)$$

$$R_m^p = \frac{\partial R_{dc}^p}{\partial N^p} \frac{\partial N^p}{\partial n_o} \delta n_o + \frac{\partial R_{dc}^p}{\partial N^p} \frac{\partial N^p}{\partial n_e} \delta n_e. \quad (3.8)$$

Using Eqs. 2.6, 3.7, and 3.8, the linear electro-optic coefficients are

$$r_{13} = -\frac{R_m^s}{\frac{\partial R_{dc}^s}{\partial N^s} \frac{\partial N^s}{\partial n_o}} \cdot \frac{2d_f}{n_o^3 V}, \quad (3.9)$$

$$r_{33} = -\frac{R_m^p + \frac{\partial R_{dc}^p}{\partial N^p} \frac{\partial N^p}{\partial n_o} \frac{1}{2} n_o^3 r_{13} \frac{V}{d_f}}{\frac{\partial R_{dc}^p}{\partial N^p} \frac{\partial N^p}{\partial n_e}} \cdot \frac{2d_f}{n_e^3 V}. \quad (3.10)$$

$R_m^{s,p}$ is obtained from a lock-in amplifier and $\partial R_{dc}^{s,p} / \partial N$ is simply the derivative of the MSR curve $R_{dc}^{s,p}$. The refractive indices n_o and n_e , and the thickness d_f can be

calculated from a pair of reflectivity dips in $R_{dc}^{s,p}$ curves, as discussed in the next section. The derivatives $\partial N^s/\partial n_o$, $\partial N^p/\partial n_o$, and $\partial N^p/\partial n_e$ can be calculated from mode equations which will also be treated in the following sections.

3.2.2 Asymmetric and anisotropic slab waveguides

Three-layer slab waveguide

The simplest optical waveguides are dielectric slabs which consist of a thin dielectric layer, called the guiding layer or the core, sandwiched between two semi-infinite bounding media (cladding layer). The index of refraction of the guiding layer must be greater than those of the cladding layer to guide the light inside the core. Most textbooks on photonics treat a symmetric slab waveguide first because it is the simplest form as a three-layer waveguide. Here we start with a three-layer asymmetric slab waveguide containing an anisotropic NLO film layer as shown in Fig. 3.4 because it is useful for the actual sample structure we are interested in [69, 70].

From Maxwell's equations, two of the most important results can be obtained [79]: the wave equations and the existence of electromagnetic waves that are solu-

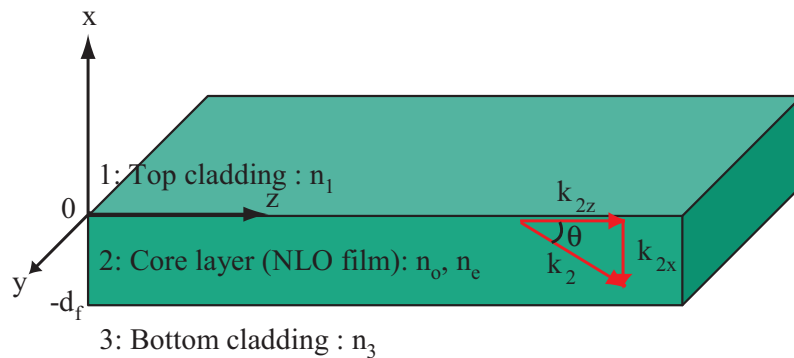


Figure 3.4: Schematic of the three-layer slab waveguide.

tions to them. Assuming a homogeneous and nonmagnetic medium, we have the wave equation in the form

$$\nabla^2 \bar{\mathbf{E}} - \mu \varepsilon \frac{\partial^2 \bar{\mathbf{E}}}{\partial t^2} = 0, \quad \nabla^2 \bar{\mathbf{H}} - \mu \varepsilon \frac{\partial^2 \bar{\mathbf{H}}}{\partial t^2} = 0, \quad (3.11)$$

where ε is a tensor of rank 2 in the form

$$\begin{pmatrix} \varepsilon_o n_e^2 & 0 & 0 \\ 0 & \varepsilon_o n_o^2 & 0 \\ 0 & 0 & \varepsilon_o n_o^2 \end{pmatrix}. \quad (3.12)$$

They are satisfied by the monochromatic plane wave equation,

$$\Psi = A e^{i(\bar{k} \cdot \bar{r} - \omega t)}, \quad (3.13)$$

where A is a constant amplitude. The angular frequency ω and the magnitude of the wave vector \bar{k} are related by $|\bar{k}| = \omega \sqrt{\mu \varepsilon} = k_o n \sqrt{\mu_o \varepsilon_o}$. The medium is homogeneous in each layer of the structure. So all we have to do is to write the plane wave equations for each layer and then match the boundary condition at the layer interfaces. The medium is homogeneous in the direction of y and z , so solutions to the wave equations can be

$$E(x, t) = E(x) e^{i(k_z z - \omega t)}, \quad H(x, t) = H(x) e^{i(k_z z - \omega t)} \quad (3.14)$$

where k_z is propagation constant. By substituting these expressions in the wave

equation Eq. 3.11, we have

$$\left[\frac{d^2}{dx^2} + (k_o n)^2 - k_z^2 \right] E(x) = 0, \quad (3.15)$$

$$\left[\frac{d^2}{dx^2} + (k_o n)^2 - k_z^2 \right] H(x) = 0. \quad (3.16)$$

We must consider two possible electric field polarizations, transverse electric (TE) and transverse magnetic (TM). The longitudinal axis of the waveguide is oriented in the z direction. We have the solution of the equation in the form

$$E_y(x) = E_o e^{\pm i \sqrt{(k_o n)^2 - k_z^2} x}, \quad (3.17)$$

$$H_y(x) = H_o e^{\pm i \sqrt{(k_o n)^2 - k_z^2} x}. \quad (3.18)$$

in the TE and TM cases, respectively. k_z should be preserved in each layer by Snell's law. In the core layer, k_z is the z component of the wave vector k_2 which is identical to $k_2 \sin \theta$ or $k_o N$ as illustrated in Fig. 3.4. To find the values of k_z that lead to allowed solutions to the wave equation, we must apply the boundary conditions to the general solutions developed. For a guided wave, the following condition should be satisfied:

$$k_o n_{1,3} < k_z < k_o n_{o,e}. \quad (3.19)$$

In the TE mode, the transverse electric field amplitudes in the three regions

are

$$\text{layer 1 : } E_y(x) = Ae^{-k_{1x}x}, \quad (3.20)$$

$$\text{layer 2 : } E_y(x) = B \cos k_{2x}x + C \sin k_{2x}x, \quad (3.21)$$

$$\text{layer 3 : } E_y(x) = De^{k_{3x}(x+d_f)}. \quad (3.22)$$

where A , B , C , and D are amplitude coefficients to be determined by the boundary conditions and k_x 's, which are called a transverse wave vector, are defined by

$$k_{1x} = k_o \sqrt{N^2 - n_1^2}, \quad (3.23)$$

$$k_{2x} = k_o \sqrt{n_o^2 - N^2}, \quad (3.24)$$

$$k_{3x} = k_o \sqrt{N^2 - n_3^2}. \quad (3.25)$$

The boundary conditions that enable us to find the unknown amplitude coefficients are 1) tangential E and 2) tangential H are continuous. Recall that

$$\nabla \times \bar{\mathbf{E}} = -\frac{\partial \bar{\mathbf{B}}}{\partial t}. \quad (3.26)$$

Because there is no x component in the electric field for the TE case, we get an explicit relation for the tangential component of the magnetic field

$$\frac{\partial E_y}{\partial x} = j\omega\mu H_z, \quad (3.27)$$

for a sinusoidal field. Applying the boundary condition for the electric field to two interfaces and the boundary condition for the magnetic field from Eq. 3.27 at the interface $x = 0$, we can obtain

$$E_y(x) = Ae^{-k_{1x}x}, \quad (3.28)$$

$$E_y(x) = A \left(\cos k_{2x}x - \frac{k_{1x}}{k_{2x}} \sin k_{2x}x \right), \quad (3.29)$$

$$E_y(x) = A \left(\cos k_{2x}x + \frac{k_{1x}}{k_{2x}} \sin k_{2x}x \right) e^{k_{3x}(x+d)}. \quad (3.30)$$

Applying the boundary condition for the magnetic field at the interface $x = -d_f$, we get finally

$$\tan k_{2x}d_f = \frac{k_{1x} + k_{3x}}{k_{2x} - \frac{k_{1x}k_{3x}}{k_{2x}}}. \quad (3.31)$$

Similarly for the TM case, we can get

$$\tan k_{2x}d_f = \frac{\frac{k_{1x}n_o^2}{n_1^2} + \frac{k_{3x}n_o^2}{n_3^2}}{k_{2x} - \frac{k_{1x}k_{3x}n_o^4}{k_{2x}n_1^2n_3^2}}, \quad (3.32)$$

where k_{1x} and k_{3x} are same as in Eqs. 3.23 and 3.25, respectively and k_{2x} is defined by

$$k_{2x} = k_o \frac{n_o}{n_e} \sqrt{n_e^2 - N^2}. \quad (3.33)$$

The mode equations Eqs. 3.31 and 3.32 are equivalent to

$$k_o \sqrt{n_o^2 - N^2} d_f - \tan^{-1} \frac{\sqrt{N^2 - n_1^2}}{\sqrt{n_o^2 - N^2}} - \tan^{-1} \frac{\sqrt{N^2 - n_3^2}}{\sqrt{n_o^2 - N^2}} = m\pi \quad (3.34)$$

and

$$k_o \frac{n_o}{n_e} \sqrt{n_e^2 - N^2} d_f - \tan^{-1} \frac{n_o n_e \sqrt{N^2 - n_1^2}}{n_1^2 \sqrt{n_e^2 - N^2}} - \tan^{-1} \frac{n_o n_e \sqrt{N^2 - n_3^2}}{n_3^2 \sqrt{n_e^2 - N^2}} = m\pi, \quad (3.35)$$

for TE and TM modes, respectively.

For ATR, we need the derivatives of the effective index N with respect to the refractive indices and thickness. Using Eq. 3.34 for the three-layer waveguide structure, we calculate

$$\frac{\partial N}{\partial n_o} = \frac{n_o k_o d_f + \frac{\sqrt{N^2 - n_1^2}}{n_o^2 - n_1^2} + \frac{\sqrt{N^2 - n_3^2}}{n_o^2 - n_3^2}}{N k_o d_f + \frac{1}{\sqrt{N^2 - n_1^2}} + \frac{1}{\sqrt{N^2 - n_3^2}}}, \quad (3.36)$$

for the TE case and from Eq. 3.35 we get for the TM case

$$\frac{\partial N}{\partial n_o} = \frac{n_e^2 - N^2}{n_o N} \frac{k_o d_f - \frac{\sqrt{N^2 - n_1^2}}{n_1^2 - n_o^2 + N^2 \left(\frac{n_o^2}{n_1^2} - \frac{n_1^2}{n_e^2} \right)} - \frac{\sqrt{N^2 - n_3^2}}{n_3^2 - n_o^2 + N^2 \left(\frac{n_o^2}{n_3^2} - \frac{n_3^2}{n_e^2} \right)}}{k_o d_f + \frac{\frac{n_e^2 - n_1^2}{\sqrt{N^2 - n_1^2}}}{n_1^2 - n_o^2 + N^2 \left(\frac{n_o^2}{n_1^2} - \frac{n_1^2}{n_e^2} \right)} + \frac{\frac{n_e^2 - n_3^2}{\sqrt{N^2 - n_3^2}}}{n_3^2 - n_o^2 + N^2 \left(\frac{n_o^2}{n_3^2} - \frac{n_3^2}{n_e^2} \right)}} \quad (3.37)$$

and

$$\frac{\partial N}{\partial n_e} = \frac{N}{n_e} \frac{k_o d_f + \frac{\sqrt{N^2 - n_1^2}}{n_1^2 - n_o^2 + N^2 \left(\frac{n_o^2}{n_1^2} - \frac{n_1^2}{n_e^2} \right)} + \frac{\sqrt{N^2 - n_3^2}}{n_3^2 - n_o^2 + N^2 \left(\frac{n_o^2}{n_3^2} - \frac{n_3^2}{n_e^2} \right)}}{k_o d_f + \frac{\frac{n_e^2 - n_1^2}{\sqrt{N^2 - n_1^2}}}{n_1^2 - n_o^2 + N^2 \left(\frac{n_o^2}{n_1^2} - \frac{n_1^2}{n_e^2} \right)} + \frac{\frac{n_e^2 - n_3^2}{\sqrt{N^2 - n_3^2}}}{n_3^2 - n_o^2 + N^2 \left(\frac{n_o^2}{n_3^2} - \frac{n_3^2}{n_e^2} \right)}}, \quad (3.38)$$

where we have omitted the s, p designations in N .

In addition, for piezoelectric effect, the variations of N induced by the change

in thickness d_f are

$$\frac{\partial N}{\partial d_f} = \frac{k_o}{N} \frac{n_o^2 - N^2}{k_o d_f + \frac{1}{\sqrt{N^2 - n_1^2}} + \frac{1}{\sqrt{N^2 - n_3^2}}} \quad (3.39)$$

and

$$\frac{\partial N}{\partial d_f} = \frac{k_o}{N} \frac{n_e^2 - N^2}{k_o d_f + \frac{n_e^2 \left(\frac{n_e^2}{n_1^2} - 1 \right)}{\sqrt{N^2 - n_1^2} \left[n_e^2 - N^2 + \frac{n_e^2 n_2^2}{n_1^2} \left(\frac{N^2}{n_1^2} - 1 \right) \right]} + \frac{n_e^2 \left(\frac{n_e^2}{n_3^2} - 1 \right)}{\sqrt{N^2 - n_3^2} \left[n_e^2 - N^2 + \frac{n_e^2 n_2^2}{n_3^2} \left(\frac{N^2}{n_3^2} - 1 \right) \right]}, \quad (3.40)$$

for TE and TM modes, respectively.

Multilayer slab waveguide

We describe the mode equation for a general multilayer structure having more than 3 layers. Solving the boundary conditions in each layer gives the mode condition which enables us to find the propagation constants of the modes in a given sample structure. Geometric optics can also be used to obtain the mode condition. As shown in Fig. 3.5, the phase change that the light experiences while passing through A to C should be an integer multiple of 2π for constructive interference.

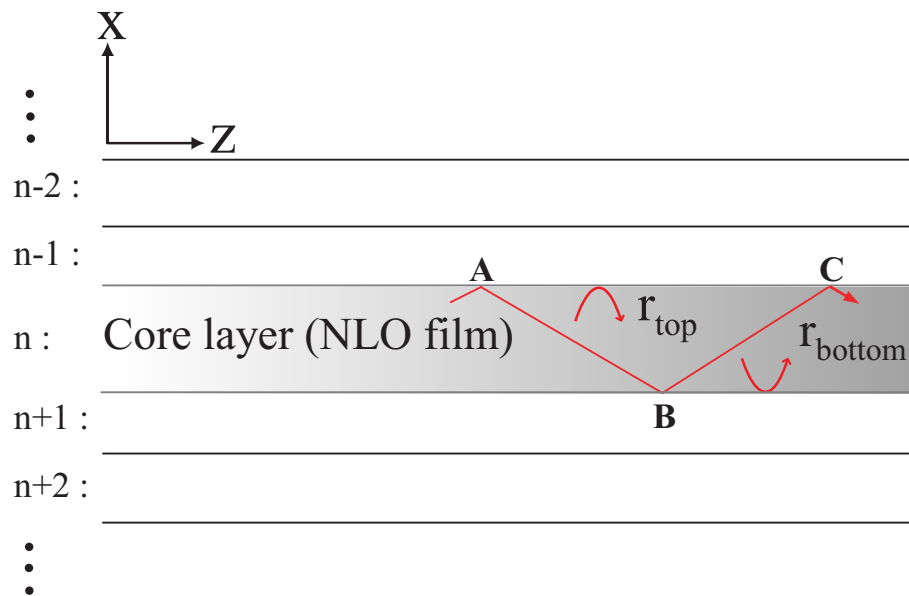


Figure 3.5: Schematic of the multilayer slab waveguide.

Then we obtain

$$2k_x^s d_f + \angle r_{\text{top}}^s + \angle r_{\text{bottom}}^s = 2m\pi \quad : \text{TE} \quad (3.41)$$

and

$$2k_x^p d_f + \angle r_{\text{top}}^p + \angle r_{\text{bottom}}^p = 2(m+1)\pi \quad : \text{TM}, \quad (3.42)$$

where k_x is the transverse wave vector in the x -direction as defined in Eqs. 3.24 and 3.33 for TE and TM modes, respectively. $\angle r_{\text{top}}$ and $\angle r_{\text{bottom}}$ are the phases of the reflectance in the top and bottom layer including multilayer structures and m is the mode number. The mode number starts with $m = 0$ for the 0^{th} order mode and increases by one for each higher order mode. Note that in the TM mode case the phase in the lefthand side is 2π for the zeroth order because each phase shift of the TM reflectances, $\angle r_{\text{top}}$ and $\angle r_{\text{bottom}}$, include π which does not affect the resonance condition.

We can obtain an identical mode equation to Eqs. 3.34 and 3.35 in a three-layer waveguide structure using Eqs. 3.41 and 3.42 and the phases of the reflectances at a single interface

$$\angle r_{\text{top}} = \begin{cases} -2 \tan^{-1} \frac{\sqrt{N^2 - n_1^2}}{\sqrt{n_o^2 - N^2}} & \text{TE} \\ \pi - 2 \tan^{-1} \frac{n_o n_e \sqrt{N^2 - n_1^2}}{n_1^2 \sqrt{n_e^2 - N^2}} & \text{TM} \end{cases} \quad (3.43)$$

and

$$\angle r_{\text{bottom}} = \begin{cases} -2 \tan^{-1} \frac{\sqrt{N^2 - n_3^2}}{\sqrt{n_o^2 - N^2}} & \text{TE} \\ \pi - 2 \tan^{-1} \frac{n_o n_e \sqrt{N^2 - n_3^2}}{n_3^2 \sqrt{n_e^2 - N^2}} & \text{TM}. \end{cases} \quad (3.44)$$

In a multilayer waveguide structure, one can use a numerical software tool to calculate

$$\frac{\partial N^s}{\partial n_o} = \frac{\frac{\partial f^s}{\partial n_o}}{\frac{\partial f^s}{\partial N^s}}, \quad \frac{\partial N^p}{\partial n_o} = \frac{\frac{\partial f^p}{\partial n_o}}{\frac{\partial f^p}{\partial N^p}}, \quad \frac{\partial N^p}{\partial n_e} = \frac{\frac{\partial f^p}{\partial n_e}}{\frac{\partial f^p}{\partial N^p}}, \quad (3.45)$$

where

$$f^{s,p} = 2k_x^{s,p} d_f + \angle r_{\text{top}}^{s,p} + \angle r_{\text{bottom}}^{s,p}. \quad (3.46)$$

In addition, for the piezoelectric effect, the variations of N induced by the change of the thickness d_f are

$$\frac{\partial N^s}{\partial d_f} = \frac{\frac{\partial f^s}{\partial d_f}}{\frac{\partial f^s}{\partial N^s}}, \quad \frac{\partial N^p}{\partial d_f} = \frac{\frac{\partial f^p}{\partial d_f}}{\frac{\partial f^p}{\partial N^p}}. \quad (3.47)$$

3.2.3 Data analysis

Assuming no piezoelectric effect, Eqs. 3.9 and 3.10 can be used to calculate EO coefficients. When the piezoelectric effect is included, at least two guided modes should be excited for the calculation. For the TE mode, the variations of N_0 and N_1 with respect to the EO-induced change in the refractive index n_o for the 0th and 1st guided modes, respectively, are given by

$$\begin{pmatrix} \delta N_0 \\ \delta N_1 \end{pmatrix} = \begin{pmatrix} \frac{\partial N_0}{\partial n_o} & \frac{\partial N_0}{\partial d_f} \\ \frac{\partial N_1}{\partial n_o} & \frac{\partial N_1}{\partial d_f} \end{pmatrix} \begin{pmatrix} \delta n_o \\ \delta d_f \end{pmatrix}, \quad (3.48)$$

where

$$\delta N = \frac{R_m}{\frac{\partial R_{dc}}{\partial N}}. \quad (3.49)$$

R_m is the modulated data collected by the lock-in amplifier and $\partial R_{dc}/\partial N$ is the derivative of reflectivity curve R_{dc} with respect to N . The 2×2 matrix in Eq. 3.48 can be inverted to get both r_{13} and p . For the TM mode, substituting both δn_o and δd_f into Eq. 3.5 gives r_{33} .

3.2.4 Results

Error

We discuss the errors in the determination of refractive index, thickness, and EO coefficients resulting from ignoring the TCO layer (1) for selected values of indices of refraction, r_{13}^{MSRM} and r_{33}^{MSRM} of NLO film and TCO at the wavelengths 1310 nm and 1550 nm. For the anisotropic indices of refraction n_o and n_e , 1.67 and 1.75 were used at 1310 nm, and 1.65 and 1.71 at 1550 nm, respectively. The complex index of refraction for TCO was obtained from an ITO/glass substrate manufactured by Thin Film Devices, Inc. To estimate the errors, we used the MSR model to generate a reflectivity scan and a modulated reflectivity. These are then treated as data input to be analyzed by the three- and four- layer WGM. We have found the MSR model to fairly well represent actual scans from the prism coupling setup.

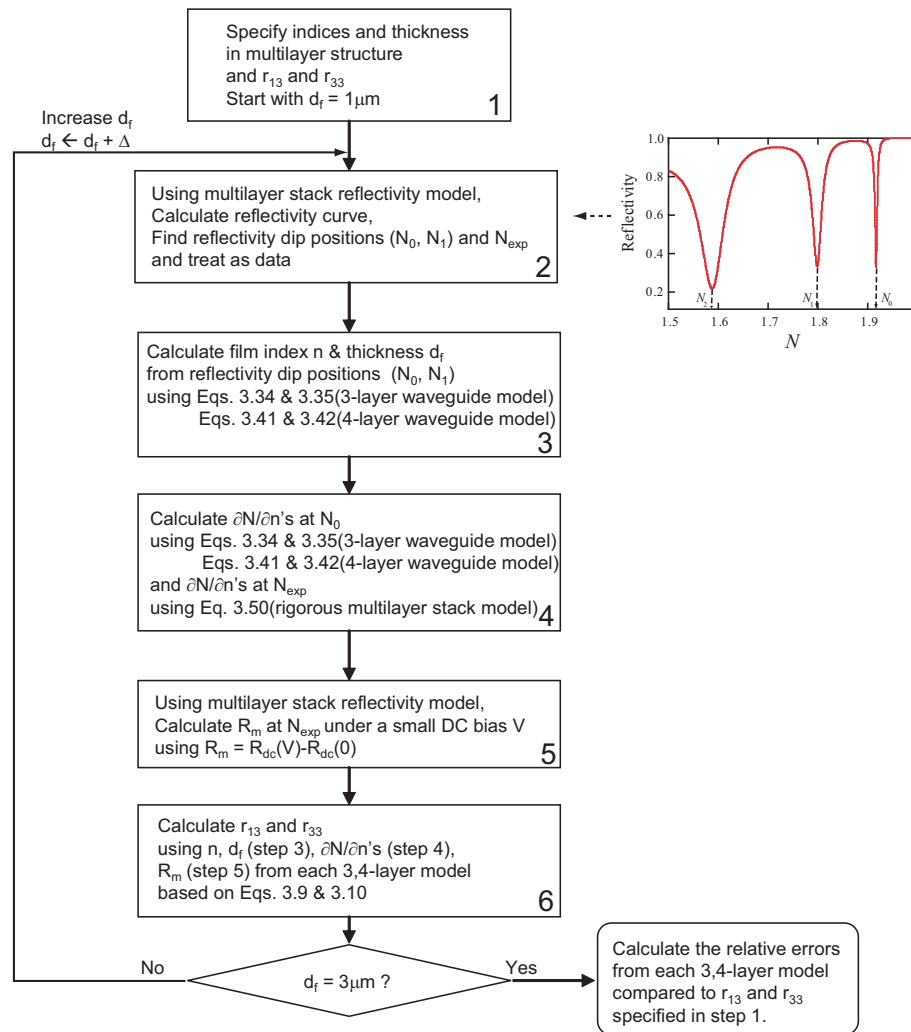


Figure 3.6: Flow chart showing the procedures to calculate the relative errors of r_{13} and r_{33} from both three-layer and four-layer waveguide models.

At a given NLO film thickness, (2) we calculate MSR curves R_{dc} 's and their derivatives $\partial R_{dc}/\partial N$'s from a multilayer stack reflectivity model (MSRM) including the Ni-coated prism (prism/Ni/air/NLO film/TCO/glass) as a function of N ($= n_p \sin \theta_p$) for TE and TM modes and find the reflectivity dips of this projected R_{dc} . These dip positions correspond to effective indices of the slab waveguide structure as shown in Fig. 3.3. We note that T_{ap} and T_{pa} as shown in Eq. 3.1 can be ignored in calculating the projected R_{dc} because they don't contribute to the calculation of effective indices. (3) The indices of refraction and thickness of the NLO film can be estimated from the effective indices using the three-layer or the four-layer waveguide mode equation, as given in Eqs. 3.34 and 3.35 or Eqs. 3.41 and 3.42, respectively. When the film thickness is too small to excite two or more guided modes, the correct film thickness was fed to the calculation in order to be able to estimate the indices of refraction.

(4) We calculate $\partial N/\partial n$'s by using both the three-layer and the four-layer waveguide models at the 0^{th} order mode obtained from the reflectivity dip, N_0 as shown in Fig. 3.3 and also calculate these derivatives from the complete multilayer structure model (including the prism) using

$$\frac{\partial N^s}{\partial n_o} = \frac{\frac{\partial R_{dc}^s}{\partial n_o}}{\frac{\partial R_{dc}^s}{\partial N^s}}, \quad \frac{\partial N^p}{\partial n_o} = \frac{\frac{\partial R_{dc}^p}{\partial n_o}}{\frac{\partial R_{dc}^p}{\partial N^p}}, \quad \frac{\partial N^p}{\partial n_e} = \frac{\frac{\partial R_{dc}^p}{\partial n_e}}{\frac{\partial R_{dc}^p}{\partial N^p}}. \quad (3.50)$$

where N is selected in the vicinity of the reflectivity dip at the 0^{th} order mode, N_{exp} as shown in Fig. 3.3, so that $\partial^2 N/\partial n^2$ is equal to 0 and $-\partial N/\partial n$ is maximized.

(5) We assume a DC voltage V applied to the NLO film, which is small enough

for the R_{dc} to be in the linear regime at N_{exp} . Then $R_m (= R_{dc}(V) - R_{dc}(V = 0))$ can be calculated using the complete multilayer structure model. (6) Based on the anisotropic indices of refraction, NLO film thickness, $\partial N/\partial n$'s, and R_m , the r_{13}^{WGM} and r_{33}^{WGM} can be calculated by three-layer and four-layer waveguide model using Eqs. 3.9 and 3.10. Steps (2)-(6) are repeated with varying NLO film thickness 1-3 μm . Finally, the relative errors versus NLO film thickness can be calculated using

$$\text{Error} = \frac{r_{13}^{MSRM} - r_{13}^{WGM}}{r_{13}^{MSRM}} \cdot 100, \quad \text{Error} = \frac{r_{33}^{MSRM} - r_{33}^{WGM}}{r_{33}^{MSRM}} \cdot 100, \quad (3.51)$$

where r_{13}^{MSRM} and r_{33}^{MSRM} are EO coefficients from MSRM and r_{13}^{WGM} and r_{33}^{WGM} are EO coefficients from three or four-layer WGM.

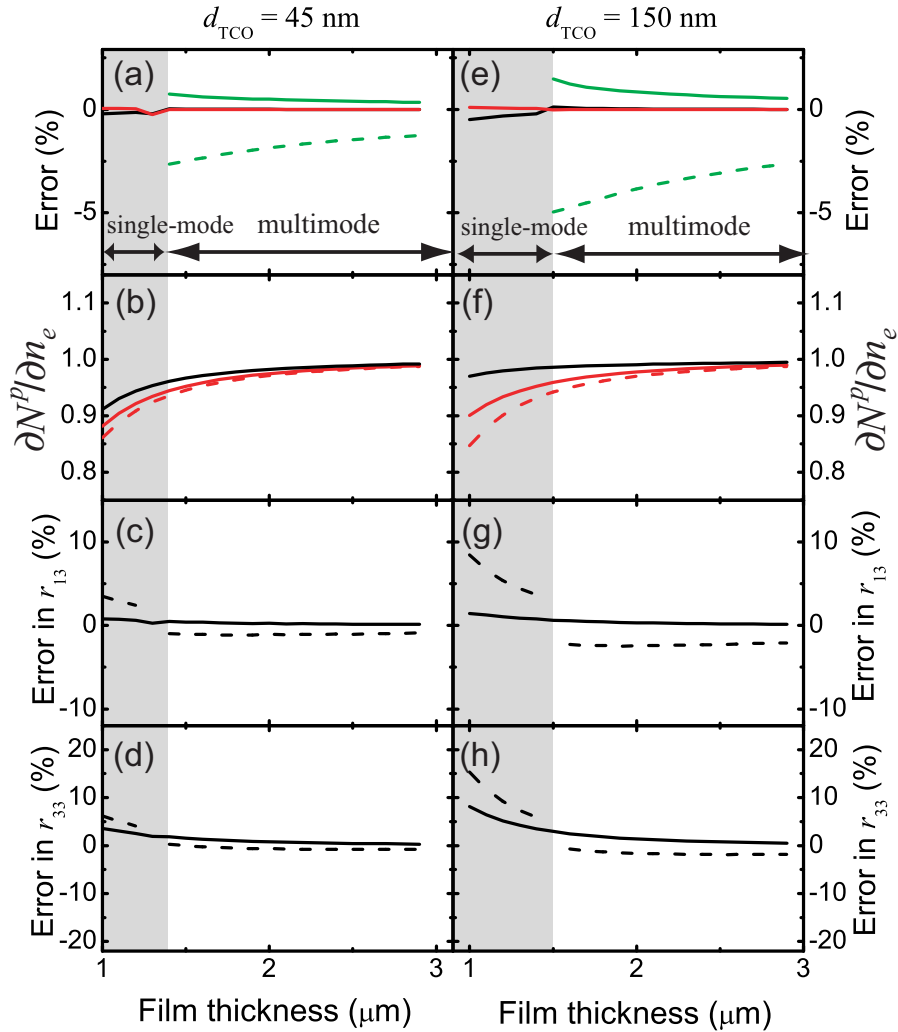


Figure 3.7: Plots of error and $\partial N^p/\partial n_e$ by varying the film thickness for selected index of refraction of TCO and the film and two TCO thickness, 45 nm (a-d) and 150 nm (e-h) at wavelength of 1310 nm. For plots (a) and (e), black and red lines show errors in the estimation of n_o for the three- and the four-layer waveguide model, respectively. Green dashed and solid lines show errors in the estimation of d_f from the three- and the four-layer waveguide model, respectively. In (b) and (f), $\partial N^p/\partial n_e$ is plotted. For plots (c) and (g), dashed line shows error in the estimation of r_{13} from the three-layer waveguide model and solid lines from the four-layer waveguide model. For plots (d) and (h), dashed line shows error in the estimation of r_{33} from the three-layer waveguide model and solid lines from the four-layer waveguide model.

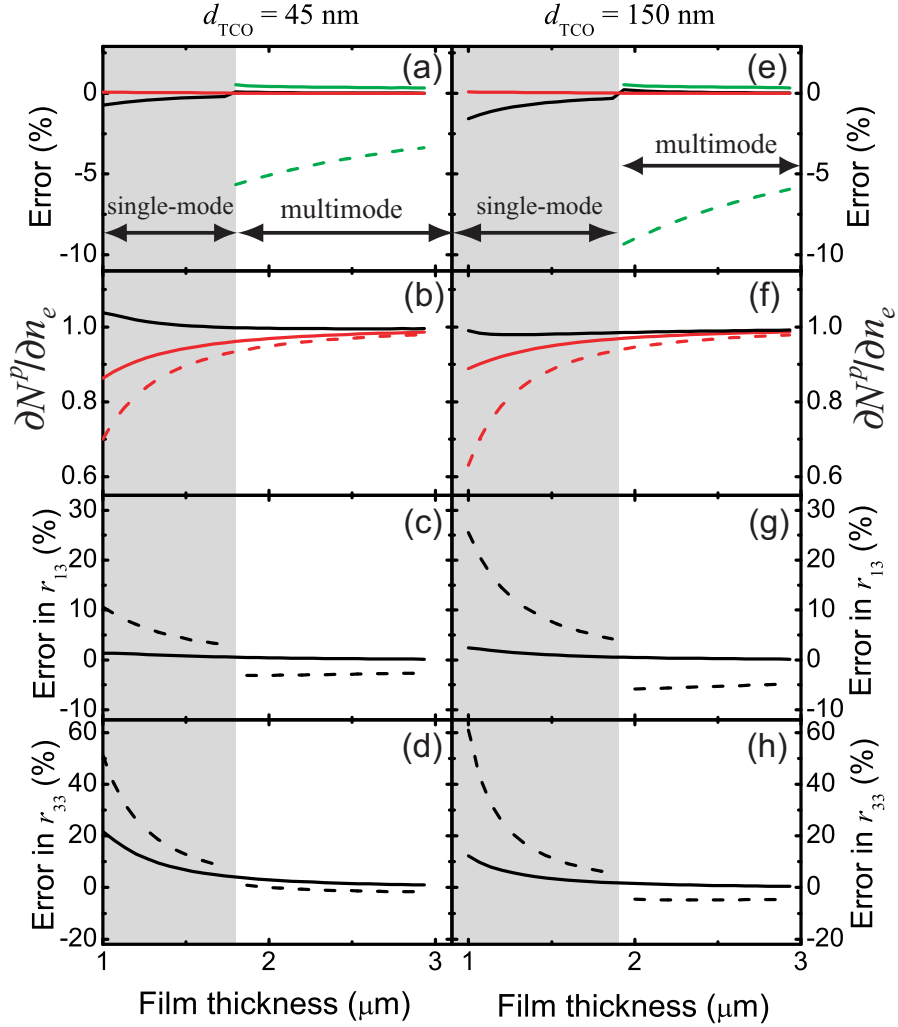


Figure 3.8: Plots of error and $\partial N^p/\partial n_e$ by varying the film thickness for selected index of refraction of TCO and the film and two TCO thickness, 45 nm (a-d) and 150 nm (e-h) at wavelength of 1550 nm. For plots (a) and (e), black and red lines show errors in the estimation of n_o for the three- and the four-layer waveguide model, respectively. Green dashed and solid lines show errors in the estimation of d_f from the three- and the four-layer waveguide model, respectively. In (b) and (f), $\partial N^p/\partial n_e$ is plotted. For plots (c) and (g), dashed line shows error in the estimation of r_{13} from the three-layer waveguide model and solid lines from the four-layer waveguide model. For plots (d) and (h), dashed line shows error in the estimation of r_{33} from the three-layer waveguide model and solid lines from the four-layer waveguide model.

Figure 3.7(a) and (e) plot the relative errors in the determination of the refractive index and thickness of the NLO film as a function of film thickness at the wavelength of 1310 nm using a TCO thickness of 45 nm and 150 nm, respectively. Noteworthy is that the relative error in n_o (black and red) is negligible in both the three-layer (black) and the four-layer (red) waveguide model. However, the relative error in the film thickness from the three-layer waveguide model (green dashed) is not negligible compared to that from the four-layer waveguide model (green solid). The error tends to increase as the TCO thickness increases.

Figure 3.7(b) and (f) plot $\partial N^p/\partial n_e$'s. The black solid lines were calculated by taking into account the actual multilayer structure as discussed above. When the film thickness is in the single mode region (shaded), $\partial N^p/\partial n_e$ from the three-layer waveguide model (dashed) shows a large difference with that from Eq. 3.50 (black solid), whereas that from the four-layer waveguide model (red solid) has a rather small difference with that from Eq. 3.50. It implies that when the NLO film supports only one guided mode, the assumption of the slight shift in MSR curve (R_{dc}) under a bias is not quite correct. We note that all of three $\partial N/\partial n$'s are approaching 1 with increasing thickness.

In Fig. 3.7(c,d) and (g,h), the relative errors in r_{13} and r_{33} are plotted using the estimated n , d_f , and $\partial N/\partial n$'s from the three-layer waveguide (dashed) and the four-layer waveguide model (solid). The dashed line in the single-mode region was calculated assuming that the film thickness was given correctly. As expected from the errors in d_f and $\partial N/\partial n$'s by the three-layer waveguide model, the relative error in r_{33} increases as the film thickness decreases. In the multimode region, it decreases

asymptotically with increasing thickness in both models. In both three-layer and four-layer waveguide models, thick TCO introduces a somewhat large relative error because of the large error in the film thickness.

Figure 3.8 is plots at the wavelength of 1550 nm. It shows similar behaviors to Fig. 3.7. We note that the relative error in r_{33} from the three-layer waveguide model are larger than that at the wavelength of 1310 nm. It is because the TCO is more index-mismatched with glass at the wavelength of 1550 nm.

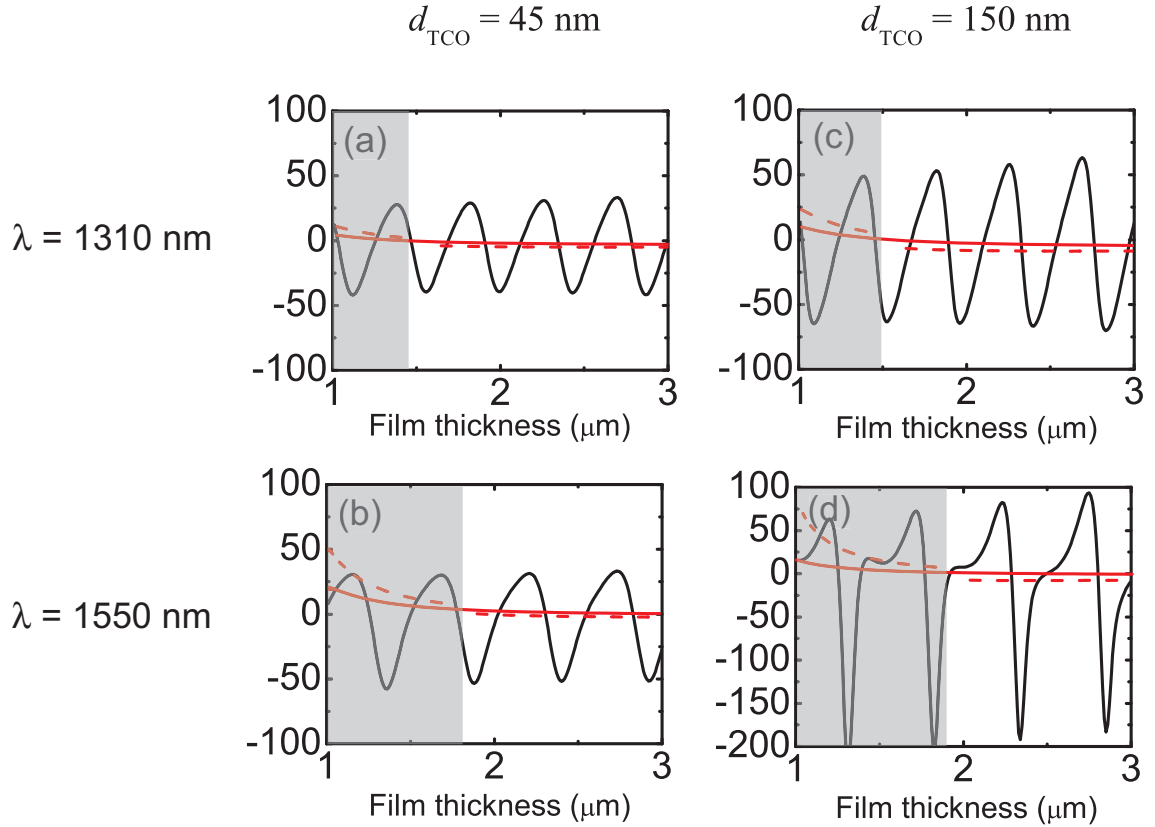


Figure 3.9: Error percentages from the ATR based on the three-layer and four-layer waveguide models and the simple Teng-Man method at 45° . Plots of error by varying the film thickness for selected index of refraction of TCO and the film and two TCO thickness, 45 nm (a,b) and 150 nm (c,d) at wavelength of 1310 nm (a,c) and 1550 nm (b,d). Red dashed line shows error in the estimation of r_{33} from the three-layer waveguide model and red solid lines from the four-layer waveguide model. Black solid line shows error from the simple Teng-Man method. Shaded region represents a single mode film.

Figure 3.9 plots the relative errors (red) in r_{33} by the three-layer and four-layer waveguide models at the wavelengths of 1310 and 1550 nm. For comparison, the relative error in r_{33} from the simple Teng-Man method at 45° is also plotted. The errors from the simple Teng-Man method shows a large cyclic variation with increasing thickness in the given range 1-3 μm . The error extremes increase as the TCO thickness increases because the FP effect is enhanced inside the NLO film layer and they increase as the wavelength increases because the TCO becomes reflective, which also enhances FP effect [80, 81, 82]. We note that the relative error from ATR based on the three-layer waveguide model is quite smaller than the simple Teng-Man error when the sample has a multimode film.

The ATR method based on the three-layer waveguide model can introduce a substantial error in the estimation of EO coefficients when the film has only one guided mode, which implies that the assumption of the slight shift in MSR curve (R_{dc}) under a bias is not quite correct.

Higher order modes

So far, we have discussed the relative errors in the ATR method and found that the error is relatively small in both three-layer and four-layer waveguide models when the film supports two or more guided modes and the error can be large in the case of a single mode film when a three-layer waveguide model is used. One might think that when the NLO film supports two or more guided modes, the three-layer waveguide model works well and the EO coefficients calculated from higher order modes (N_1, N_2, \dots) rather than the fundamental mode N_0 are also reliable.

However, the estimation of EO coefficients from the highest order mode is expected to produce a large error just as expected in the case of a single mode film, especially when the three-layer waveguide model is used.

Figure 3.10 shows $\partial N^p/\partial n_e$'s by using three-layer and four-layer waveguide models with varying NLO film thickness for selected indices of refraction and thickness of TCO and the film at a wavelength of 1310 nm. In regions B, C, and D, the difference between two $\partial N^p/\partial n_e$'s increases as the mode number increases for a given film thickness. For this reason, the r_{33} calculation based on the higher order mode can give a large error, especially when the three-layer waveguide model is used. Therefore, a multimode film and the analysis based on the four-layer waveguide model using the fundamental mode (N_0) are required for a reliable estimation of EO coefficients. Special care should be taken in order to include the piezoelectric effect in the calculation using a higher order mode, because the use of the first order mode is required for the calculation as shown in Eq. 3.48. The use of a higher order mode may introduce an error in both the EO and piezoelectric coefficients when the film has only two guided modes and the three-layer waveguide model is used. For the use of the 0^{th} and the 1^{st} order modes, a multimode film having more than two guided modes and the analysis based on the four-layer waveguide model are required for a more reliable estimation of both EO and piezoelectric effects.

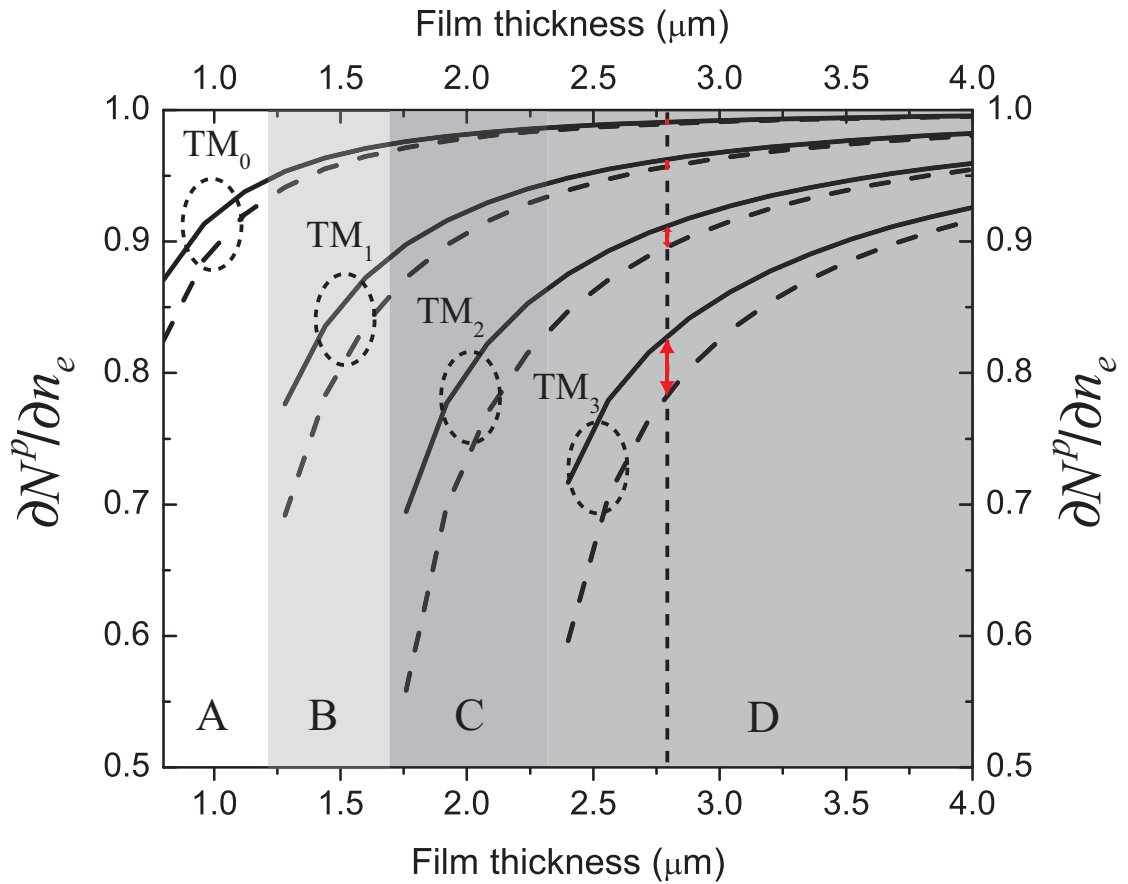


Figure 3.10: Plots of $\partial N^p / \partial n_e$ by varying the film thickness for selected indices of refraction and thickness of TCO and the film at wavelength of 1310 nm. Solid and dashed lines are $\partial N^p / \partial n_e$'s calculated by using four-layer and three-layer waveguide models, respectively. A, B, C and D represent the regions of film thickness where the film supports single, two, three, and four or more than four guided mode/modes, respectively.

MEASUREMENT

4.1 Introduction

4.1.1 Measurement procedures

Up to this point, we have discussed how to measure the EO coefficients of nonlinear optical polymer (NLOP) films using the rigorous Teng-Man and ATR methods. We have found that it is essential to characterize the optical properties of the TCO layer as well as the NLOP film in a multilayered Teng-Man sample for the application of these methods. For the characterization of TCO, it is strongly recommended that the TCO/glass substrate be obtained from the same batch as in the NLO sample structure because the optical property of TCO can widely vary depending on the manufacturing process. The optical properties of poled NLO films can be characterized by the prism coupling technique during the ATR measurement. When NLO films were poled by electrode contact poling, the metal electrode, generally gold, performs its duty as a reflector in Teng-Man experiment. For ATR, Au and Al metal electrodes can be removed by using the solution of $\text{KI}+\text{I}_2+\text{H}_2\text{O}$ and Al etchant type D (Transene, Inc), respectively.

To summarize, (a) we characterize the optical properties of TCO, (b) take multi-angle Teng-Man data, (c) etch off the metal electrode on the NLO film surface, (d) take ATR data (R_{dc} and R_m) for TE and TM modes using a metal-coated prism, (e) measure the anisotropic refractive indices of poled NLO film as well as the film thickness using an uncoated prism, (f) analyze the ATR data and get r_{13} and r_{33} , and (g) use the ratio of r_{13} and r_{33} obtained from the ATR to analyze the multi-angle Teng-Man data.

4.1.2 Outline of the chapter

In this chapter, we briefly describe the basic physics of TCO's with the Drude model. We present some of the results of TCO films such as ITO and ZnO using a spectroscopic ellipsometry. We describe our experimental setups: electrode contact poling, Teng-Man and ATR. For EO measurements, we characterized four different NLOP films synthesized by Alex Jen's group at the University of Washington such as AJ302¹, AJ404L, AJLS102, and AJ-TTE-II. Every NLOP film here was characterized by the rigorous Teng-Man method. Additionally, AJLS102 and AJ-TTE-II were characterized by the ATR method.

¹We reported the experiment and analysis for this sample [80]. Here, we correct the mistake resulting from using wrong optical property of TCO layer.

4.2 Characterization of transparent conducting oxides

4.2.1 Transparent conducting oxides

Transparent conducting oxides (TCO) are indispensable materials in various applications such as flat panel display, collector electrodes in solar cells, deicing electrodes, electromagnetic shielding, and other optoelectronic devices, because it has both the electrical conductivity and optical transparency. Most electric conductors are opaque in the visible wavelength range. When one is fabricating a device which must be electrically connected to other devices, but requires light transmission to obtain the desired response, TCO is a logical choice for the conductor. Since discovery of the first TCO (thin film CdO) was reported in 1907 by Baedeker [83], various TCO's has been investigated and some TCO's are now commercially available. Sn-doped In_2O_3 ($\text{In}_{2-x}\text{Sn}_x\text{O}_3$) and $\text{In}_2\text{O}_{3-x}$ are the well-known TCO's because of their high conductivity (10^3 - 10^4 S/cm) and high optical transparency (>80%) in the visible range [83, 84]. The chemical dopant Sn produces the shallow donor or impurity energy states in the proximity of the conduction band, which result in high conductivity. The oxygen vacancy impurity energy states in $\text{In}_2\text{O}_{3-x}$ contributes to the conductivity. Those electrons in the states can be thermally ionized into the conduction band at room temperature. Other transparent conducting oxides such as zinc oxide (ZnO) and Zn-doped indium oxide ($\text{Zn}_x\text{In}_2\text{O}_{x+3}$) have also been investigated by many researchers.

The Drude model of electrical conduction explains well the transport properties of those electrons [85]. The Drude model is simply the application of kinetic

theory to electrons in a solid under the assumption that solids have fixed immobile positive ions and free electrons (electron gas : non-interacting each other). Under an applied electric field \mathbf{E} , the equation of motion is

$$m^* \frac{d}{dt} \langle \bar{v} \rangle = e \bar{\mathbf{E}} - \gamma \langle \bar{v} \rangle, \quad (4.1)$$

where m^* is the effective mass of an electron, $\langle \bar{v} \rangle$ is the average velocity of electrons ($\bar{}$ represents vector quantity.), and γ/m^* is the scattering rate. Multiplying both sides by Ne and using $\bar{\mathbf{J}} = Ne \langle \bar{v} \rangle$ give

$$m^* \frac{d}{dt} \bar{\mathbf{J}} = Ne^2 \bar{\mathbf{E}} - \gamma \bar{\mathbf{J}}. \quad (4.2)$$

From $\bar{\mathbf{J}} = \sigma(\omega) \bar{\mathbf{E}}$, assuming an $e^{-i\omega t}$ time dependence and using $\gamma/m^* = 1/\tau$, we have

$$\sigma(\omega) = \frac{Ne^2\tau}{m^*} \frac{1}{1 - i\omega\tau} \equiv \frac{\sigma_0}{1 - i\omega\tau}, \quad (4.3)$$

where the DC conductivity is defined by $\sigma_0 = Ne^2\tau/m^*$ [86]. Since $\nabla \times \bar{\mathbf{H}} = \bar{\mathbf{J}} - i\omega\epsilon_0\epsilon_\infty \bar{\mathbf{E}} = i\omega\epsilon_0\epsilon(\omega) \bar{\mathbf{E}}$, the dielectric function is

$$\epsilon(\omega) = \epsilon_\infty \left(1 - \frac{\omega_p^2}{\omega^2 + i\omega/\tau} \right), \quad (4.4)$$

where ω_p is the plasma resonance frequency. The optical transmission drops drasti-

cally near the plasma resonance frequency which is given by

$$\omega_p^2 = \frac{Ne^2}{\epsilon_0\epsilon_\infty m^*}. \quad (4.5)$$

4.2.2 Spectroscopic ellipsometry for characterization of TCO

Before the characterization of TCO, the refractive index of a glass substrate is measured for later use. We characterize the optical properties of a blank TCO/glass substrate which is preferably from the same batch as used in the NLO sample structure. The refractive indices of glass are measured using a MetriconTM at wavelengths of 632, 1032, 1310, and 1550 nm. Then, the indices are fitted using the series expansion with respect to inverse of wavelength in the form [87]

$$n(\lambda) = A + \frac{B}{\lambda} + \frac{C}{\lambda^2} + \frac{D}{\lambda^3}. \quad (4.6)$$

where λ is the wavelength and A , B , C , and D are the unknown coefficients. We measure four refractive indices at four different wavelengths using MetriconTM, and the fitting coefficients can be determined by a least squares fitting.

The fitted coefficients are plugged into the variable angle of incidence spectroscopic ellipsometry (VASETM) software for the refractive index of a glass substrate. The thickness of TCO at the edge after wet etching a small part of it is measured by a profilometer in order to use it as the initial guess in the software.

Ellipsometric measurement is made to obtain a complex index of refraction of some blank TCO samples. VASETM system manufactured by J.A. Woollam

Inc. is a useful non-destructive optical technique often used to characterize the optical properties of thin films and multilayered structures [87]. A monochromatic, polarized beam of light is reflected from a sample surface at a known angle of incidence and the resulting polarization state and amplitude of the reflected beam are measured as a function of wavelength and angle of incidence. Two parameters obtained from this measurement are given in the form

$$\frac{r_p}{r_s} = \tan \Psi e^{i\Delta} . \quad (4.7)$$

where Ψ is the arctangent of the ratio of $|r_p|$ to $|r_s|$ and Δ the phase retardation.

In the case of ITO, free carrier absorption is usually noticeable in the infrared range, while interband transition dominates in the visible range [64]. The characterization of ITO on glass is relatively difficult, because the reflected light off the sample is weak and the back-surface reflection (air/glass interface) effects the measurement. The back surface of the glass substrate should be roughened prior to measurement of the experimental data so that the reflected light from the back surface is scattered. Ellipsometric data are numerically fitted to a built-in oscillator model which describes free carrier absorption in the infrared region and interband transition in the visible region. The complex dielectric function having one or more Lorentz harmonic oscillators is generally expressed as [64, 87]

$$\epsilon(\lambda) = \epsilon_\infty + \sum_{k=1}^n \frac{A_n}{-E(\lambda)^2 + E_n^2 - i\Gamma_n E(\lambda)} . \quad (4.8)$$

where ϵ_∞ , A_n , E_n and Γ_n are the permittivity at infinite frequency, amplitude of oscillators, center energy and broadening of each oscillator, respectively. The Lorentz model allows us to simulate the optical constants of the ITO over both the transparent and absorbing spectral range while maintaining Kramers-Kronig (K-K) consistency between the real and imaginary parts of the index of refraction. Setting the center energy to zero turns the Lorentz model into the Drude model which describes the free carrier absorption edge in the infrared region.

First, ITO manufactured by Abrisa[®] was characterized. The thickness, n and κ were fitted using ellipsometric data measured at 55°, 60°, 65°, 70°, and 75°, as well as transmission data at normal incidence. Figure 4.1 shows n and κ with the transmission data in the inset. The projected transmission curve matches well with the experimental one.

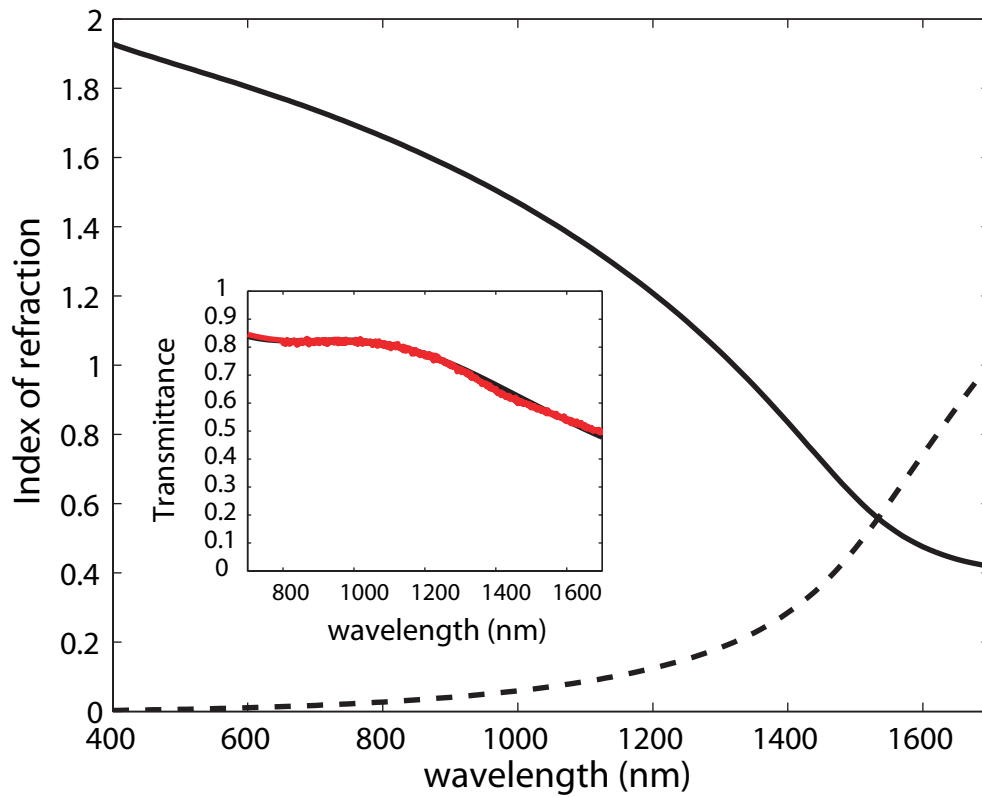


Figure 4.1: A representative optical property of ITO manufactured by Abrisa[®]. The inset shows the transmission data (red) at normal incidence. It is well matched with projected transmission curve (black).

For some cases, spectroscopic ellipsometry at a single angle of incidence is sufficient for the characterization of a sample, but in many cases the additional information from acquiring data such as ellipsometric data at several angles and transmission data is necessary to eliminate parameter correlations which otherwise prevent the finding of a unique solution for the variable parameters. In our case, four or five angles of incidence are chosen around the pseudo-Brewster angle to get ellipsometric data, and the transmission measurement at normal incidence is also made.

The optical properties of ITO are strongly dependent on the manufacturing process so there are wide variations in commercial ITO properties. For some cases, ITO can be difficult to characterize because it displays a complicated graded microstructure and the optical properties of ITO can vary widely with deposition conditions and post-deposition processing. For this reason, it is considered to be a well-defined multiple set of single layers (graded layer) rather than one layer. From an ellipsometry point of view, assuming a single uniform layer with fixed optical constants, even along with a small roughness layer, can be insufficient to obtain a good fit between the measured data and the modeled data. A graded layer model is normally required to properly describe this material.

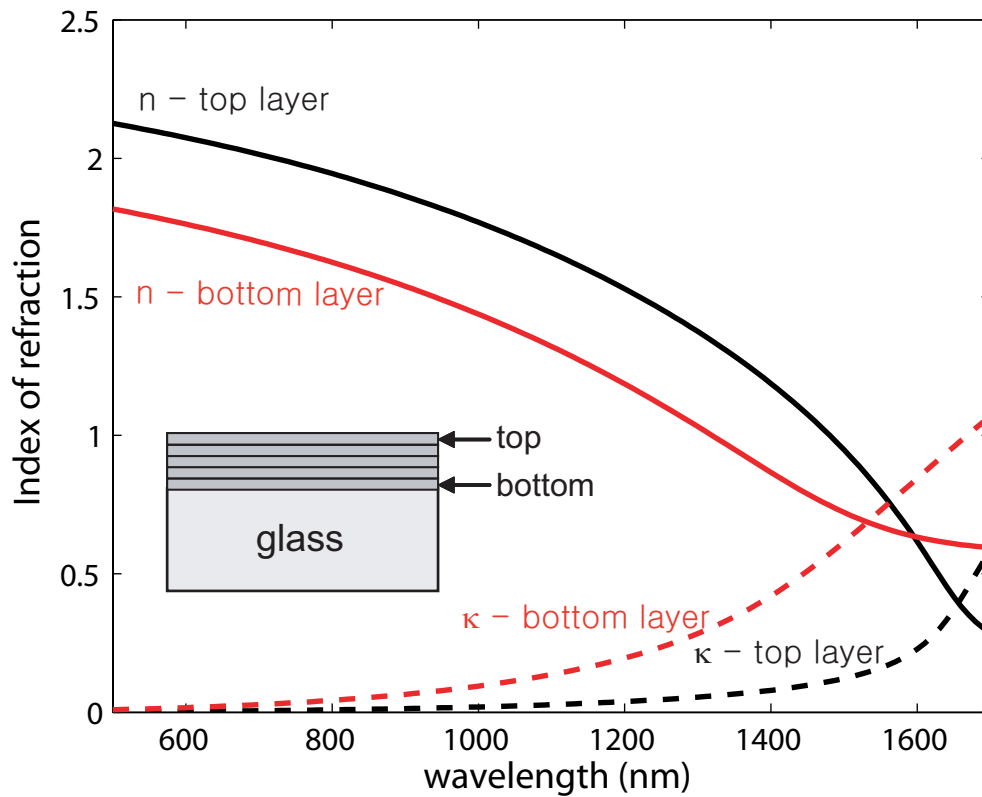


Figure 4.2: A representative optical property of ITO manufactured by Thin Film DevicesTM. A graded layer model was used to obtain a complex refractive index. The n and κ of top and bottom layers are shown.

A representative ITO/glass substrate manufactured by Thin Film Devices™ (TFD) was characterized. In this characterization, the index grading of the film is assumed to have 5 layers with the same depth and each layer has a constant index of refraction at each wavelength. Figure 4.2 shows the complex index of refraction of the top and bottom layers, $n + i\kappa$, in the range of 500-1700 nm wavelength. You can see the large difference between the two curves, denoting that the film properties along the deposition direction are not uniform. Figure 4.3 shows complex graded indices of refraction for five layers at a wavelength of 1310 nm. The closer the layer is to the air/ITO interface, the less conductive (more transparent) it is.

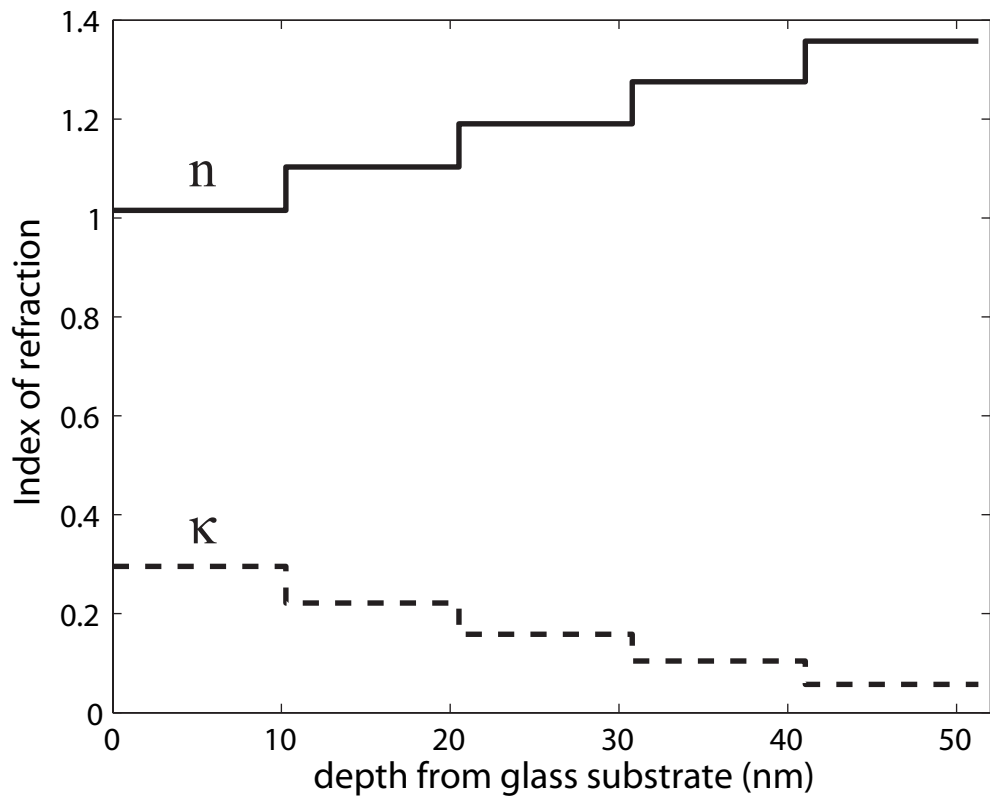


Figure 4.3: Graded indices of refraction at 1310 nm. The solid line is the real part n and the dotted one the imaginary part κ of the complex index of refraction.

The fitted complex index of refraction is used to calculate the transmittance using Fresnel's equation and then compared to the transmission data, as shown in Fig. 4.4. Note that the interference effect from multiple reflections in the glass substrate is ignored because the coherence length of the light used in this instrument is too small compared to the glass thickness to have an interference effect. For example, the bandwidth of the light is around 50 nm, so the coherence length is expected to be $\sim 20 \mu\text{m}$ at the wavelength of 1000 nm using [68]

$$l_c = c\tau_c = \frac{c}{\Delta f} = \frac{\lambda^2}{\Delta\lambda}, \quad (4.9)$$

where l_c is the coherent length, c the speed of light, Δf the spectral line width, and $\Delta\lambda$ the bandwidth.

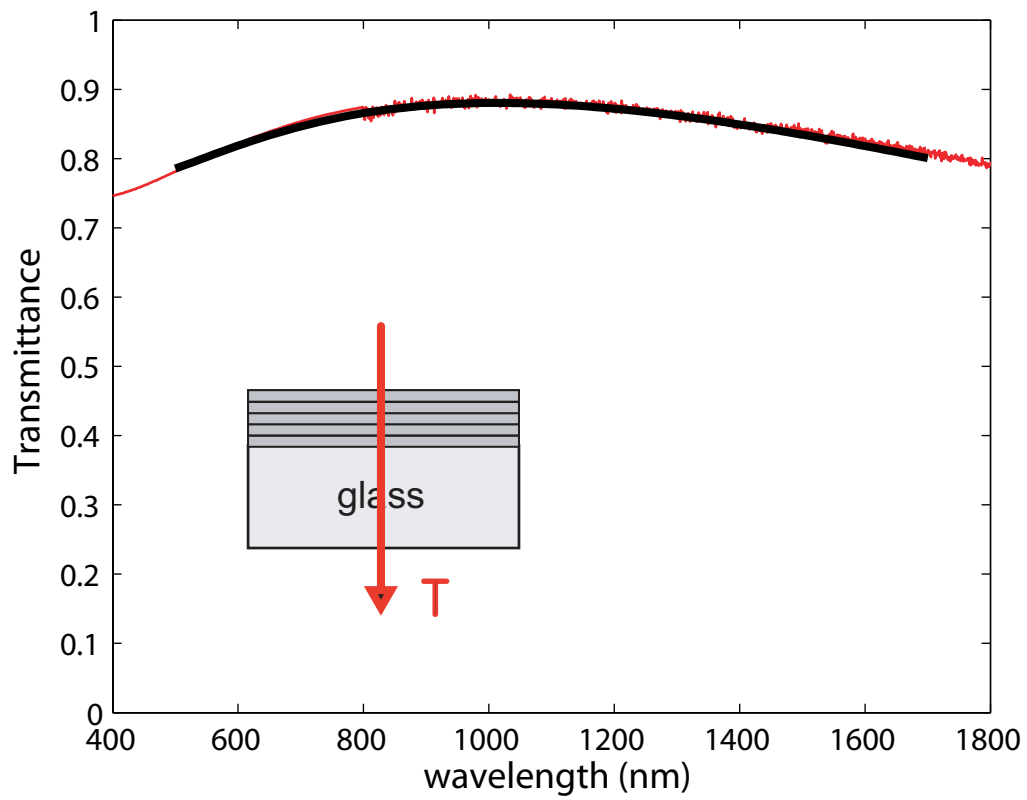


Figure 4.4: Transmittance at normal incidence. The Red line was obtained by UV-VIS spectroscopic scan by Varian[®] and the black one is a projected transmittance.

We also characterized ZnO samples provided by Northwestern University using a single layer model as described in Eq. 4.8. However, the Drude and Lorentz model didn't work well. Typically, these TCO films have much less conductivity (50-150 S/cm) than ITO. Therefore, they do not have a strong Drude response in the near-IR (NIR) spectrum, unlike ITO as shown in Fig. 4.5. In other words, ZnO does not have enough free-carrier absorption to be represented by a Drude model. For this reason, it is primarily transparent over the entire measured spectral range and displays a high sheet resistance. We used two or three Gaussians to describe the UV absorption spectra instead of a Drude model. The Gaussian model is given as

$$\text{Im}[\epsilon(E)] = A \exp^{-\left(\frac{E-E_c}{B}\right)^2} + A \exp^{-\left(\frac{E+E_c}{B}\right)^2}, \quad (4.10)$$

where E is energy, E_c center energy, and B the broadening of the Gaussian. The real part of the dielectric function is generated K-K consistent.

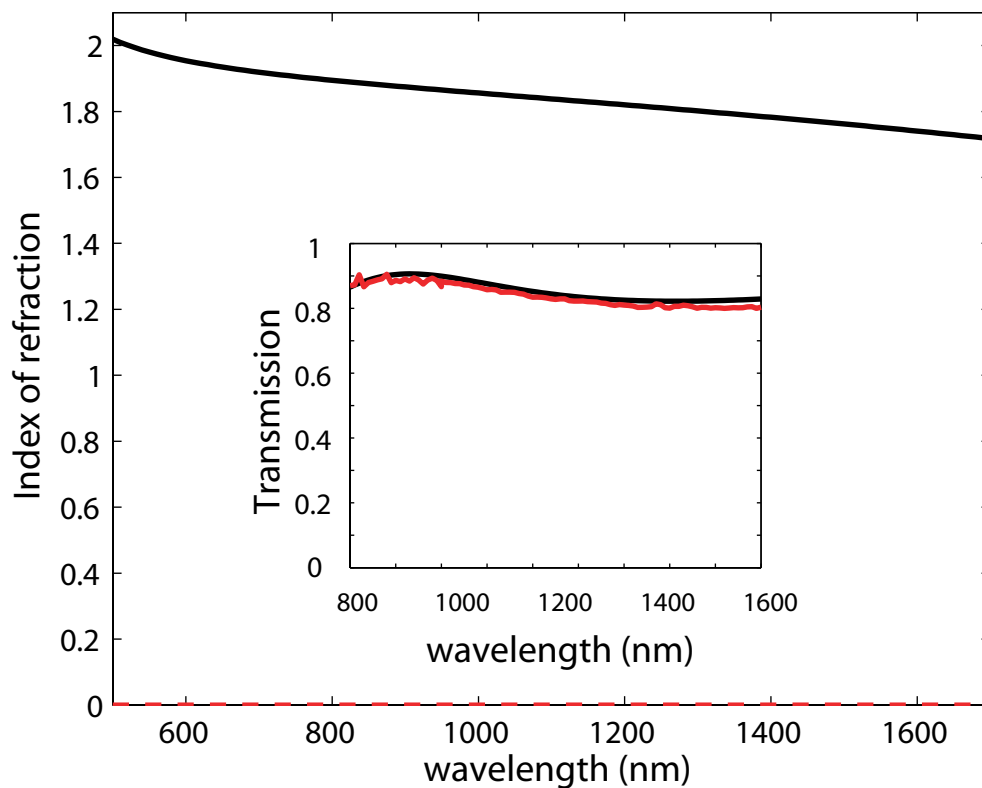


Figure 4.5: Optical property ($n + i\kappa$) of a ZnO measured by spectroscopic ellipsometry. Black solid and red dotted lines are the real and imaginary parts of the complex refractive index, respectively. Inset shows UV-VIS-NIR transmission spectrum. Black and red lines are projected and experimental transmission, respectively.

As we described before, it is always better to add transmission data to your ellipsometric data to get improved measurement and insure an unique answer. When the spectroscopic ellipsometric fit does not match transmission, it says that something is wrong with the model. For this case, we require the model to fit both data simultaneously. A graded layer model often satisfies these requirements.

4.3 Experimental setup

4.3.1 Electrode contact poling setup

Figure 4.6 shows a picture of the electrode contact poling setup. We used an FP90 control processor (Mettler Toledo, Inc.) to communicate with the hot stage, FP82HT (Mettler Toledo, Inc.). The hot stage is enclosed with the box where nitrogen gas is filled. A small amount of the inner gas is extracted to measure the amount of oxygen by the oxygen sensor, Series 3000 trace oxygen analyzer (Alpha Omega Instruments®). Poling is performed after the amount of oxygen is less than ~ 200 ppm to avoid oxidation of the sample. The current temperature of the hot stage is taken from the FP90 control processor through RS232C serial port. The 237 high voltage source measure unit (Keithley, Inc) was used to apply the voltage to the sample.

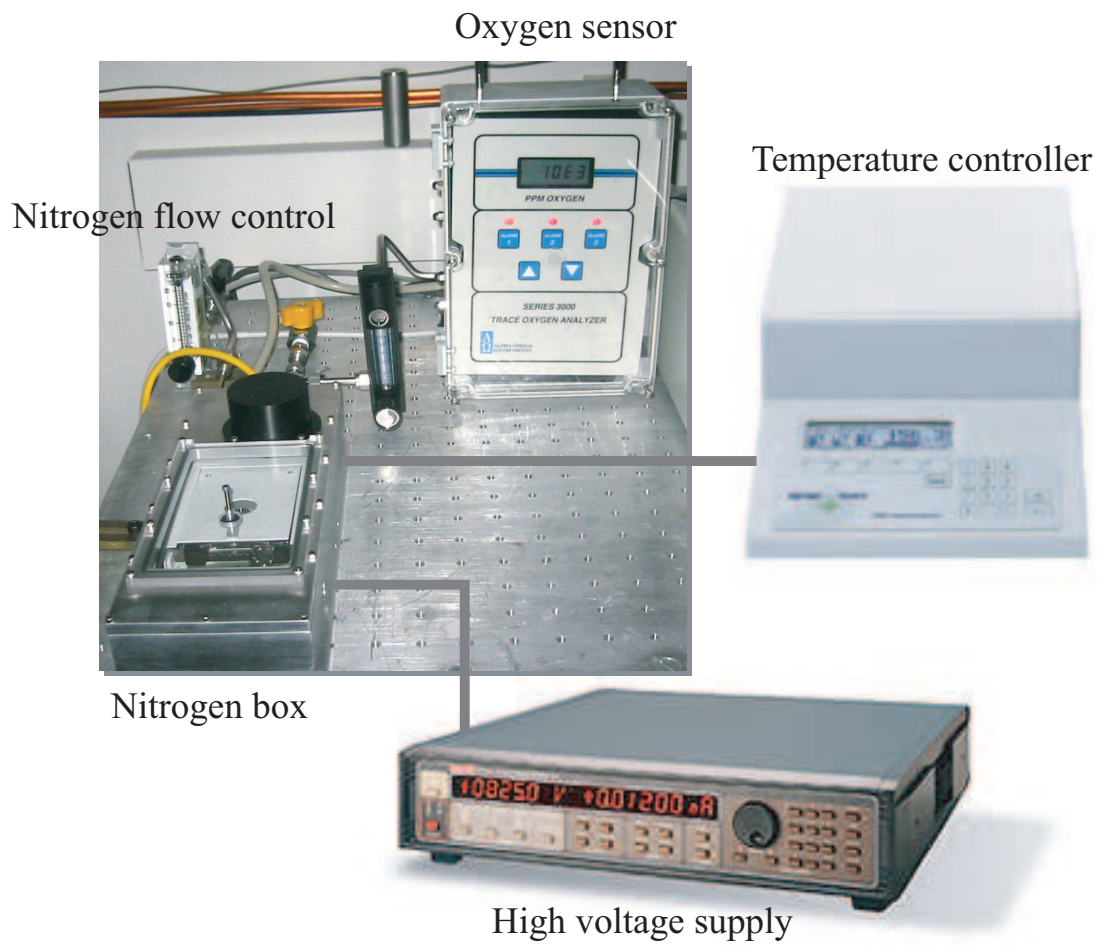
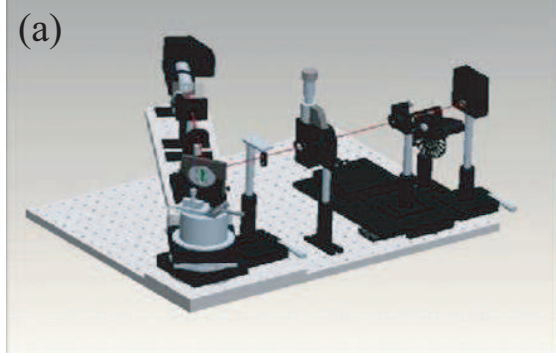


Figure 4.6: Electrode contact poling setup.



Multi-angle Teng-Man setup



Metricon 2010 Prism Coupler

Figure 4.7: (a) Schematic of multi-angle Teng-Man setup and (b) commercial MetriconTM prism coupler 2010.

4.3.2 Teng-Man and ATR setup

Figure 4.7(a) shows a picture of the Teng-Man experimental setup. There are two arms, one of which contains the sample holder and is automatically controlled by a Newport Motion controller MM3000 to make a desired angle of incidence. The sample is firmly held by a vacuum chuck to maintain the given angle of incidence. Initially, a lens was used to focus the incident light, but this required another in the other arm because the light diverged too fast. Currently, the ~ 0.3 mm wide aperture is being used to make the beam width narrow. After the reflection off the sample, a slit less than 0.5 mm is needed to block the unwanted light. A Soleil-Babinet compensator SBC-IR (Thorlabs), two 9807 linear polarizers (Thorlabs), SR540 optical chopper (Stanford Research Systems) and large area photodetector (New Focus, Inc) are used in this setup.

We used a MetriconTM 2010 Prism Coupler as shown in Fig. 4.7(b). It has been a well-known measuring instrument for index of refraction, thickness, and propagation loss of thin films. We modified it in order to perform the ATR measurement.

Using this instrument relieved a lot of labor in building an ATR setup for EO measurement. The instrument has a built-in capacitor to filter out 60/120 Hz power line noise and a built-in OP amp to amplify the signal from the detector. When an AC signal is applied to the sample, the modulated reflectivity R_m should not be affected by these two components, so we clipped the lead of the capacitor to avoid the 60/120 Hz filtering. The appropriate frequency was determined to be 20-40 Hz or 100-250 Hz so that the built-in OP amp does not affect the measurement.

Because of such a low frequency, the sampling rate of the modulated intensity should be lower than the frequency. The modulated data is read by the 7265 DSP digital lock-in amplifier (Signal Recovery, Inc) every second and is recorded through a General Purpose Interface Bus (GPIB) interface.

4.4 EO measurements

4.4.1 AJ302

The sample AJ302 consists of a pure mixture of two chromophores rather than a standard nonlinear polymer system such as the guest-host and side-chain polymer, synthesized by Alex Jen's group at the University of Washington. Electrode contact poling was performed to orient the chromophores. The atmosphere inside the experimental poling setup was filled with an overpressure of nitrogen gas to avoid oxidation during the poling process. The sample was heated to a temperature near the glass transition temperature ($T_g \sim 80^\circ\text{C}$) and then a DC electric field was gradually applied to the the film up to $\sim 70\text{ MV/m}$, after which the sample was cooled down to room temperature maintaining the applied electric field.

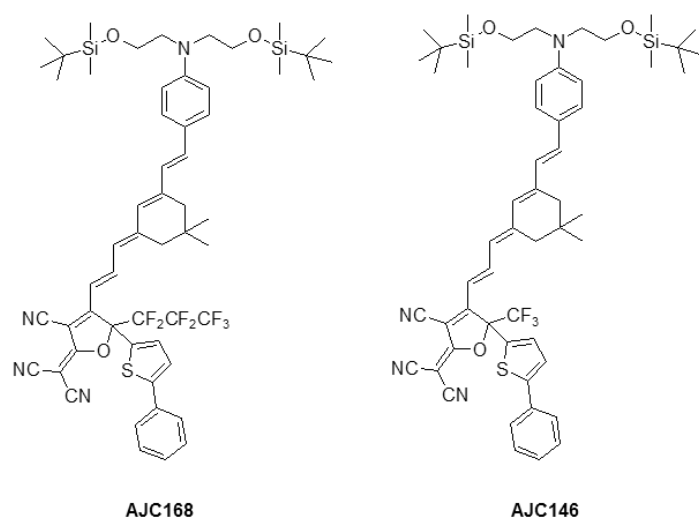


Figure 4.8: Molecular structures of AJC168 and AJC146.

The Teng-Man setup is equipped with a rotational arm where the $1.3\ \mu\text{m}$ laser source, 45° polarizer and lens are located in order to measure the incident angle dependence. The focused beam is reflected at the sample in the center of the rotational arm, and then passed through a 0.5 mm wide slit so that unwanted beams can be blocked. The beam collimated by another lens passes through the SBC and analyzer and reaches the detector. The beam is chopped at 1 kHz by an optical chopper to allow measurement of I_{dc} with a lock-in amplifier, which is also used to measure the modulated intensity I_m when the sinusoidally alternating voltage is applied to the sample.

In our experiment, the full profiles of $I_{dc}(\Omega)$ and $I_m(V, \Omega)$ were measured, and then $\delta\Psi_{sp}$ as well as A , B , δA , δB , and Ψ_{sp} were extracted by curve fitting to Eqs. 2.9 and 2.15. The linear EO coefficient was calculated by using the simple expression in Eq. 2.33 on the condition that the ratio of r_{33} to r_{13} is assumed to be 3. We made measurements on two sample structures fabricated from the organic glass AJ302 that consisted of 50%-AJC168 and 50%-AJC146 as shown in Fig. 4.8 [5]. Using the simple model, r_{33} values of 306 pm/V and 297 pm/V were measured. The polar order induced by electrode contact poling decays slowly to its equilibrium state after the external electric field is off. Compared to measurements made 1-4 hours after poling, the EO coefficient calculated by simple expression relaxed to a value about 15% lower in a period of one week and thereafter remained relatively stable at room temperature.

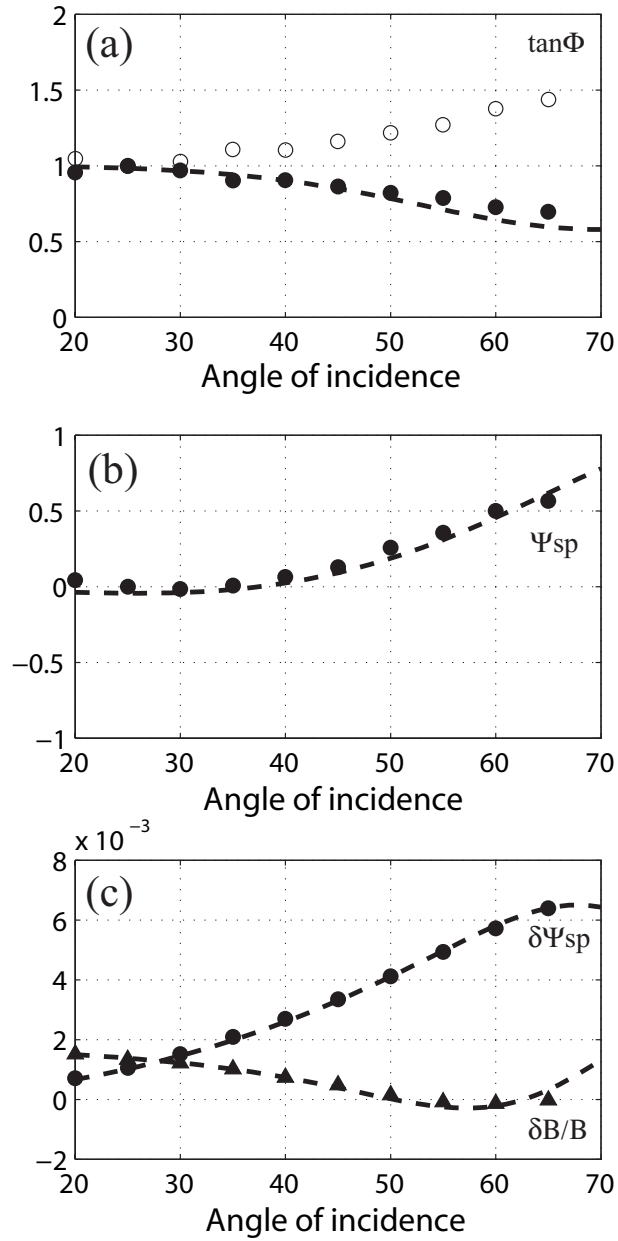


Figure 4.9: Fits (dashed lines) to the rigorous model of $\delta \Psi_{sp}$, $\delta B/B$, $\tan \Phi$, and Ψ_{sp} extracted by curve fitting to Eqs. 2.9 and 2.15. In (a), both possible values of $\tan \Phi$ resulting from A/B using Eq. 2.14 are shown.

A better estimation of the EO coefficient can be obtained by numerical methods, which requires knowing more detailed information about the multilayered structure of the sample, such as the refractive index and thickness of the individual layers. To perform the numerical analysis, $I_{dc}(\Omega)$ and $I_m(\Omega, V)$ are measured as a function of Ω at 10 angles of incidence from 20° to 65° and the data set of A , B , Ψ_{sp} , δA , δB , and $\delta\Psi_{sp}$ are extracted by curve fitting to Eqs. 2.9 and 2.15. The $\tan\Phi$ can be extracted from the ratio A/B in Eq. 2.14, but there are two possible values at each incident angle because this equation is quadratic in $\tan\Phi$. From a separate measurement of $\tan\Phi$, we confirmed that $\tan\Phi < 1$ for this sample. Projected $\tan\Phi$ and Ψ_{sp} reflect the goodness of the fit as shown in Fig. 4.9(a,b). The index of refraction of ITO was obtained from the ellipsometric measurement of Abrisa[®] ITO. The index of refraction of Au was obtained from Refs. [88, 89, 90]. From the fit of $\delta\Psi_{sp}$ and $\delta B/B$ as shown in Fig. 4.9(c), the rigorous model gave a lower r_{33} (~ 150 pm/V) than the one (235 pm/V) obtained using the simple model at a 45° angle of incidence, because the multilayered structure of the sample produces a positive error correction term, resulting in an overestimation of the EO coefficient.

The poled refractive indices are expected to be anisotropic, but we have not measured them for these samples. We used anisotropic refractive indices n_o and n_e , 1.69 and 1.72, respectively, based on an unpoled refractive index of AJ302 film on silicon measured by a MetriconTM. Because the TM index in a polymer film generally increases upon poling, and the TE index decreases by half the amount of

the TM increase, we put [27]

$$n_o = n^{unpoled} - \delta, \quad n_e = n^{unpoled} + 2\delta, \quad (4.11)$$

where $n^{unpoled}$ is unpoled index of refraction. The ratio of r_{13} to r_{33} was calculated based on

$$\gamma = \frac{\chi_{113}}{\chi_{333}} \left(\frac{n_e}{n_o} \right)^4, \quad (4.12)$$

where χ_{113}/χ_{333} is assumed to be 1/3 [23, 27]. The fit of $\delta B/B$ in Fig. 4.9(c) was very sensitive to the thickness of the polymer film. The fitted value of s_{33} was 3 pm/V.

4.4.2 AJ404L

A poled Teng-Man sample consisting of the crosslinked polymer AJ404L synthesized by Alex Jen's group at the University of Washington was analyzed. The indices of refraction of a different unpoled thin film of AJ404L were measured by the prism coupling technique using a MetriconTM. Measured unpoled values of ordinary and extraordinary indices of refraction were 1.75 and 1.74 at 1310 nm and 1.71 and 1.70 at 1550 nm, respectively. The MetriconTM can also measure optical loss using an optical fiber scanning over the waveguided streak. Unfortunately, we were not able to get good data to measure the loss at 1310 nm, but at 1550 nm the slab waveguided optical loss was in the range of 1.6-1.8 dB/cm. Two lasers with wavelengths of 1310 nm and 1550 nm (LaserMax[®]) were used to perform the rigorous analysis, which requires full information of the multilayered structure such as thickness and

index of refraction for the TCO (ITO in AJ404L) and film layers.

Figure 4.10 shows the complex index of refraction of six ITO samples obtained by VASETM. The real part of the refractive index at 1310 nm and 1550 nm for these samples was in the range 0.98-1.06 and 0.43-0.55 and the imaginary part was in the range 0.16-0.22 and 0.52-0.65, respectively. By a profilometer, the thickness of the ITO in Teng-Man sample AJ404L was measured to be ~ 130 nm and the thickness of the polymer film was in the range 1.15-1.3 μm .

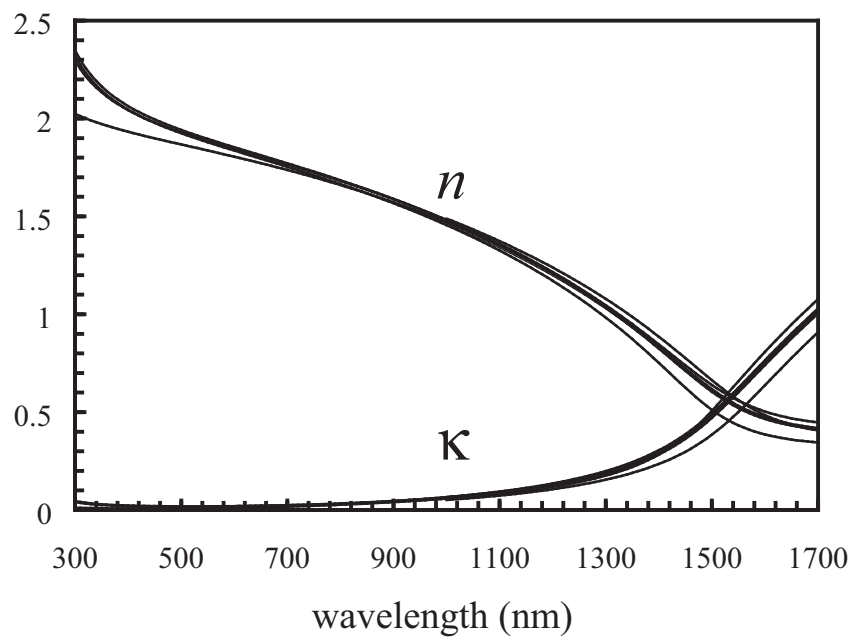


Figure 4.10: Complex index of refraction of six ITO's on glass substrate measured by ellipsometric technique.

Teng-Man measurements were performed at 7 angles of incidence between 30° and 60° for a wavelength of 1310 nm and at 9 angles of incidence over that same range for a wavelength of 1550 nm. Instead of a lens, a small aperture with a width of ~ 0.3 mm was used to make the beam width of the incident light small. A slit with a width of ~ 0.25 mm placed just after the sample was used to efficiently block the reflection off the glass and also block multiple reflections between the glass/air interface and the gold electrode.

Figure 4.11 shows fits using the rigorous model to the multi-angle data for $\delta\Psi_{sp}$, $\delta B/B$ as well as Ψ_{sp} and $\tan\Phi$. These fits were performed using the least squares fitting technique described in Section 2.2.4 while simultaneously fitting Ψ_{sp} and $\tan\Phi$. The ability to fit all data sets indicates that the analysis is consistent at two different wavelengths using the ranges of refractive index and thickness discussed above. The tweaked value of δ for the birefringence was ~ 0.015 - 0.025 based on Eq. 4.11 to generate poled indices. The fitted results for r_{33} were in the range 200-220 pm/V at 1310 nm and 120-140 pm/V at 1550 nm, respectively; the ranges reflect the uncertainties in the actual film thickness, indices, and refractive index of the ITO.

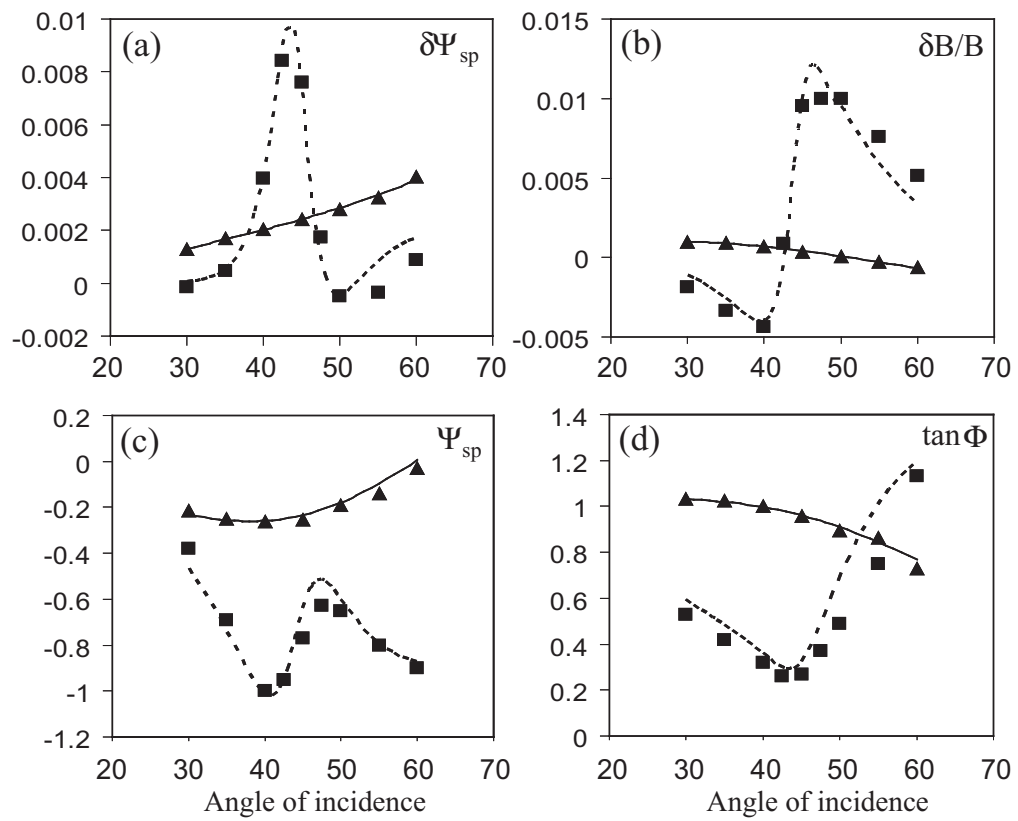


Figure 4.11: Experimental data (triangle, square) of (a), (b), (c), and (d) show good agreement with numerical fits (solid, dashed) at 1310 nm and 1550 nm, respectively.

Figure 4.12 shows the value of r_{33} at different angles of incidence calculated by the simple Teng-Man analysis assuming that the ratio of $r_{13}/r_{33} = 1/3$. We note that the simple model values of r_{33} at 1310 nm were around 300-350 pm/V and much larger variations with angle of incidence are observed at 1550 nm . This behavior is due to a FP effect in the ITO-film-Au resonator structure, i.e., the increase of reflection of ITO at 1550 nm enhances the multiple reflections inside the resonator. This results in a large variation of r_{33} with angles of incidence when the simple Teng-Man model is used. The value of r_{33} at 1310 nm was ~ 318 pm/V averaged over 7 angles of incidence, while r_{33} at 1550 nm was ~ 324 pm/V averaged over 9 angles of incidence.

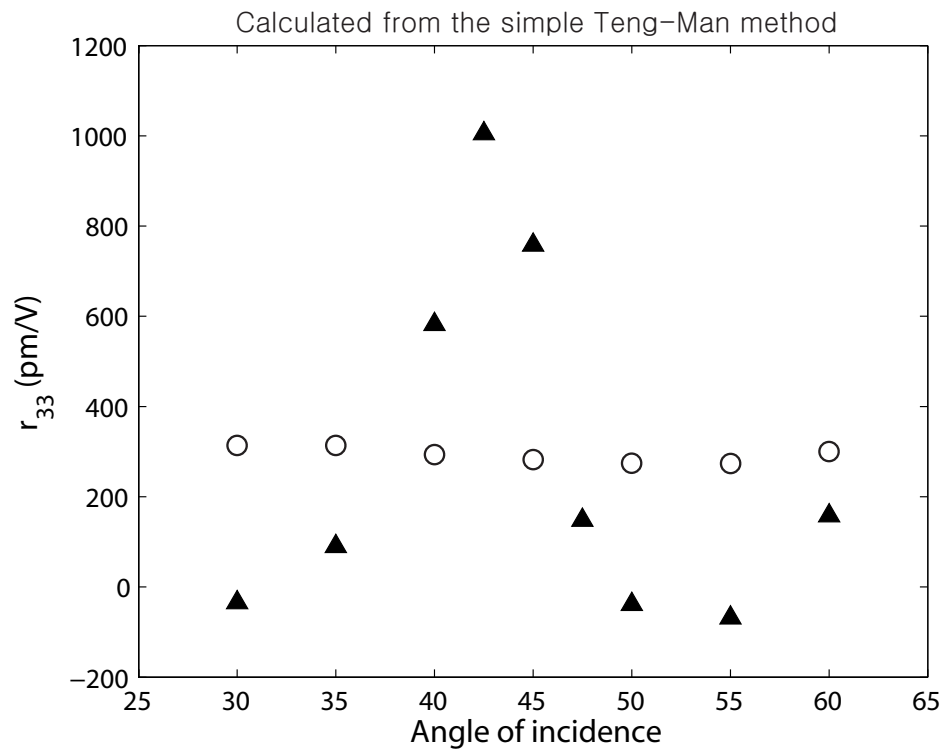


Figure 4.12: The r_{33} calculated by simple Teng-Man analysis at each angle of incidence at 1310 nm (open circle) and 1550 nm (triangle).

Figure 4.13 shows a plot of the dispersion in the EO coefficient. The solid circles represent the two r_{33} values obtained by the rigorous analysis and the solid line was generated assuming a two-level model when the molecular second-order susceptibility is dominated by the change in dipole moment between the ground and first excited electronic states. The electro-optic molecular hyperpolarizability along the z -axis is then given as [23]

$$\beta_{zzz}(-\omega; \omega, 0) = \frac{\beta_0 \omega_0^2 (3\omega_0^2 - \omega^2)}{3 (\omega_0^2 - \omega^2)^2}, \quad (4.13)$$

where β_0 is the zero frequency value of β and a constant related to the transition dipole moments and ω_0 is the angular frequency of the first excited state. The λ_0 of the film is estimated to be around $0.86 \mu\text{m}$ by UV-VIS-NIR absorption measurement using a Cary 5000 spectrophotometer.

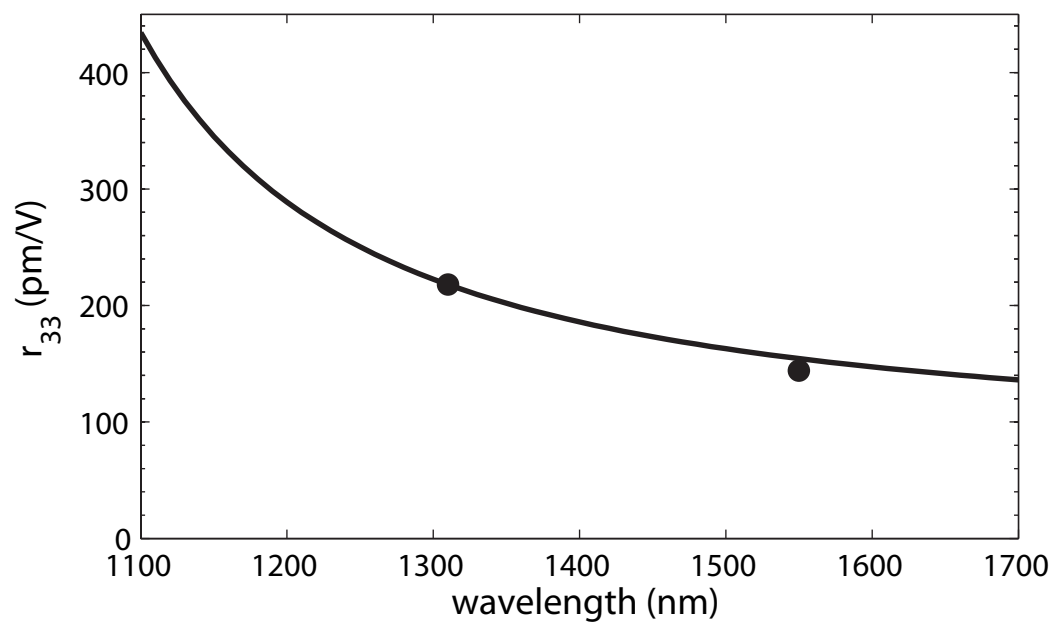


Figure 4.13: Dispersion characteristics of r_{33} versus wavelength. Triangles are r_{33} calculated by the rigorous analysis at 1310 nm and 1550 nm and solid line is obtained by a two-level model.

4.4.3 AJLS102

A poled AJLS102/PMMA NLO film was analyzed. The NLO film was spin-coated on TFD ITO/glass substrate and was poled at Lumera, Inc. A laser with a wavelength of 1550 nm (LaserMax[®]) was used to perform ATR measurement along with the rigorous Teng-Man analysis. A 4 mm-diameter round Au electrode was on the NLO film for allowing the applied voltage. Each analysis requires full information of the multilayered structure such as thickness and index of refraction for the NLO film layer and the ITO.

Ellipsometric measurement was made using a VASE spectroscopic ellipsometer (J. A. Woollam Co.) to obtain the complex index of refraction of a blank ITO/glass substrate. Figure 4.14 shows the complex index of refraction, n and k profile with transmission spectrum. The real part of the refractive index at 1550 nm for these samples was in the range 0.82-0.84 and the imaginary part was in the range 0.36-0.38. The simultaneous analysis of ellipsometric and transmission data was used to yield more reliable results. By a separate measurement using a profilometer, the thickness of the ITO in the Teng-Man sample was estimated to be ~ 45 nm.

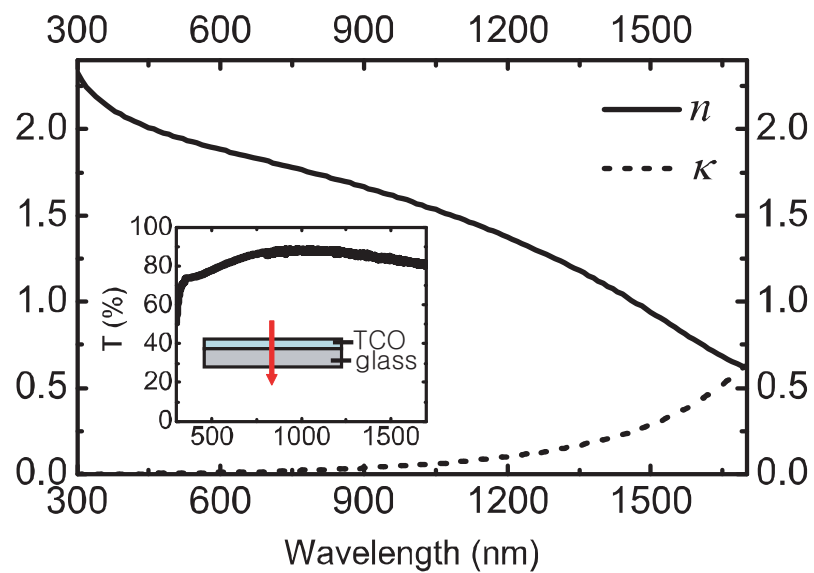


Figure 4.14: Optical property ($n + i\kappa$) of an ITO (Thin Film Device™) measured by spectroscopic ellipsometry. Inset shows UV-VIS-NIR transmission spectrum.

Using a gold etchant ($\text{KI/I}_2/\text{H}_2\text{O} = 4:1:40$), the Au electrode on the top of the NLO film was removed without sacrificing the film quality. The waveguide modes of the poled thin film were measured by a prism coupling technique using a MetriconTM 2010 Prism Coupler. The anisotropic indices of refraction and the thickness of the poled thin film were calculated from a pair of waveguide modes by using the four-layer waveguide model described earlier. Estimated ordinary and extraordinary indices of refraction were 1.65 and 1.71 at 1550 nm and the film thickness was $2.3 \mu\text{m}$ instead of $2 \mu\text{m}$ obtained from three-layer waveguide (air/film/glass) model.

As shown in Fig. 4.15, we measured the full R_m versus N with an applied voltage as well as R_{dc} in TE and TM modes, after verifying the applied voltage V to be in the linear regime in order to validate Taylor expansion to the first order. Using the four-layer waveguide model, r_{13} and r_{33} were estimated to be 28 and 83 pm/V compared to 26 and 76 pm/V from the three-layer waveguide model.

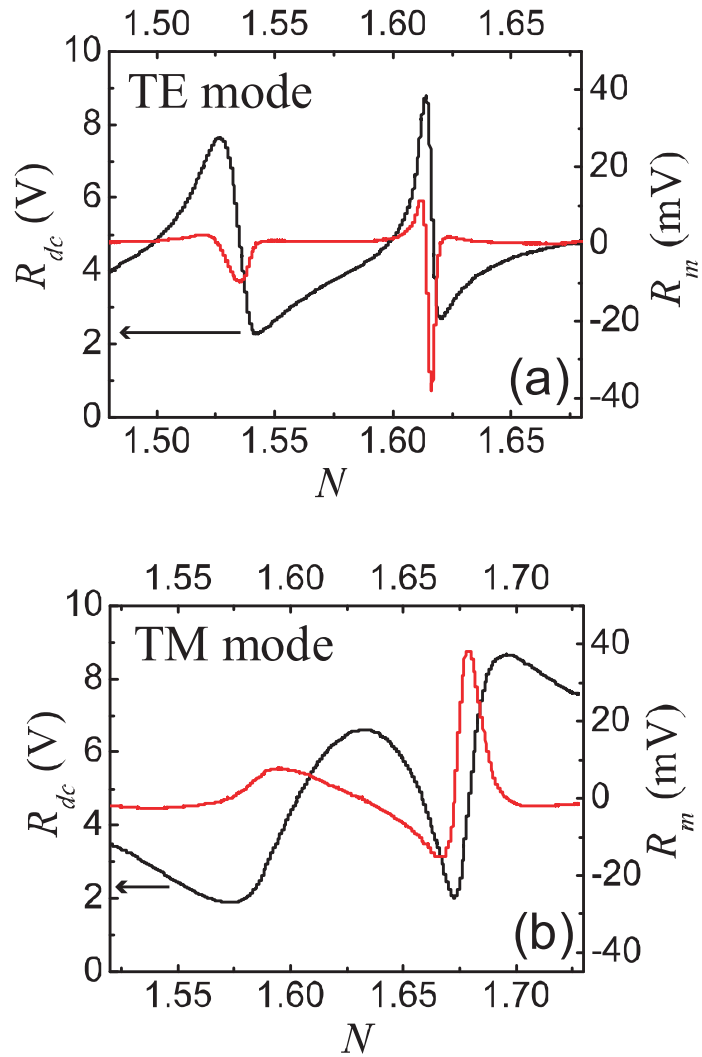


Figure 4.15: R_{dc} (black) and R_m (red) versus N at 1550 nm in (a) TE and (b) TM modes. The peak voltage 1 Volt with an AC frequency of 200 Hz was applied to the NLO film to get the modulated signal R_m .

The Teng-Man measurement was performed before the Au electrode was removed for the ATR measurement. The Au electrode was thicker than ~ 70 nm, so the thickness of the Au layer can be ignored because of no reflection at the Au/air interface. The index of refraction of Au was obtained from Ref. [89, 90]. To perform the rigorous Teng-Man analysis [82], the optical bias curve and the modulation intensity are measured as a function of Ω introduced by SBC at discretely varying angle of incidence ranging from 40° to 60° and the data set of $\delta\Psi_{sp}$ and $\delta B/B$ are extracted by curve fitting at each angle of incidence as shown in Fig. 4.16(a). The ratio of r_{13} to r_{33} obtained from the ATR method was used to fit $\delta\Psi_{sp}$ and $\delta B/B$ in the rigorous Teng-Man analysis.

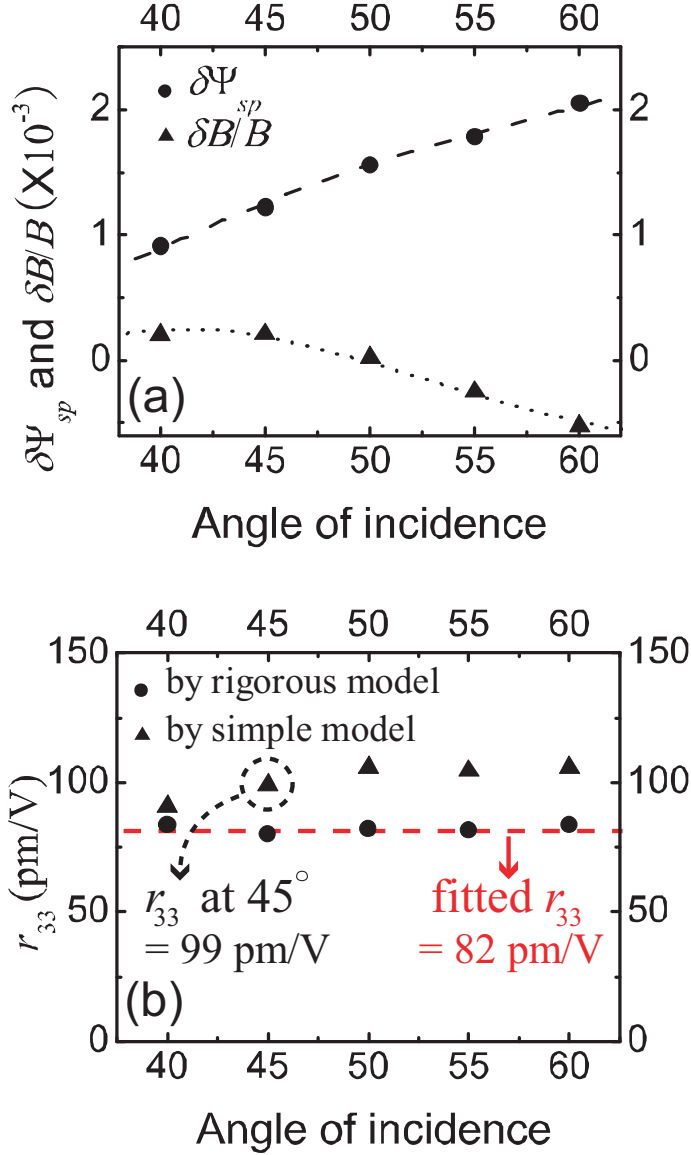


Figure 4.16: (a) Measured $\delta\Psi_{sp}$ and $\delta B/B$ versus angle of incidence. Dashed and short dash lines are numerical fit to $\delta\Psi_{sp}$ and $\delta B/B$. (b) EO coefficients r_{33} calculated by the simple model (triangle) and the rigorous model (circle) at discrete angle of incidence. The r_{33} by the rigorous model at each angle are well aligned with fitted r_{33} .

As shown in Fig. 4.16(b), the rigorous model gave a smaller r_{33} (82 pm/V) than the one (99 pm/V) obtained using the simple model at a 45° angle of incidence, because the multilayered structure of the sample produces a positive error resulting in an overestimation of the EO coefficient ($\sim 20\%$ overestimated) from the simple Teng-Man method.

Figure 4.17 shows the estimate of error from the simple Teng-Man method generated from a Java Teng-Man error estimator program discussed in Section B.2. The error at the film thickness $d_f = 2.26 \mu\text{m}$ is estimated to be 20%, which is much the same as the one we calculated from the Teng-Man experiment. As summarized in Table 4.1, the result from ATR based on the four-layer waveguide model shows a good agreement with that from the rigorous Teng-Man analysis. Figure 4.17 shows the estimate of error from the simple Teng-Man method for this case.

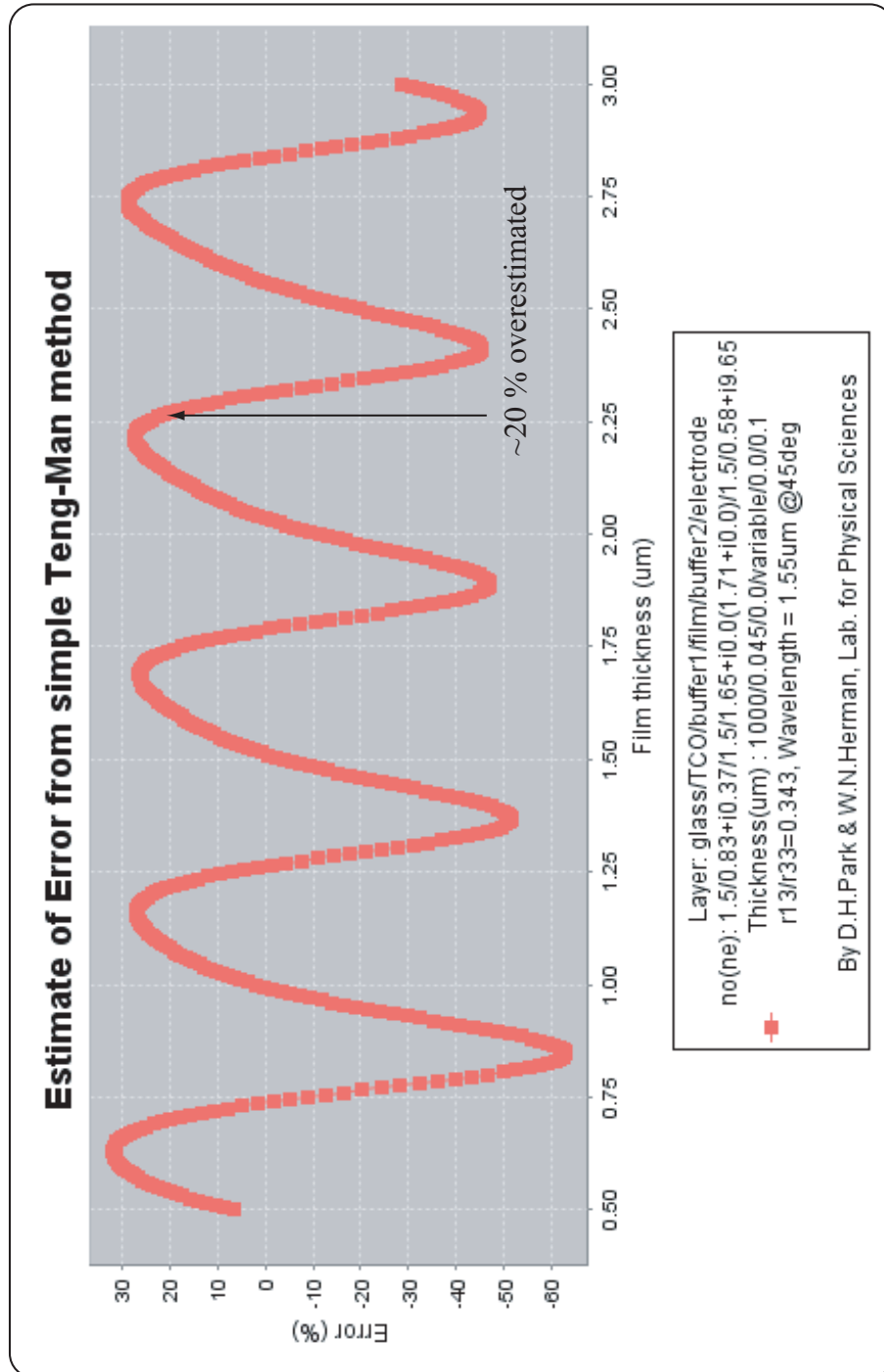


Figure 4.17: The estimate of error from the simple Teng-Man analysis generated using Java Teng-Man estimator.

Table 4.1: Summary of EO coefficients of AJLS102 NLO film.

	r_{13} (pm/V)	r_{33} (pm/V)	d_f (μm)
ATR by 3-layer	27	80	2.1
ATR by 4-layer	28	83	2.3
Simple Teng-Man	33	99	-
Rigorous Teng-Man	28	82	2.3

4.4.4 AJ-TTE-II

A poled Teng-Man sample containing AJ-TTE-II synthesized by Alex Jen's group was measured. Unfortunately, r_{33} can not be measured using the ATR method, because the refractive indices of the NLO film ($n_o = 1.95$ and $n_e = 2.18$) are too high to measure r_{33} with the current prism (prim index = 2.13 at 1310 nm). Only r_{13} was measured and was plugged into the fitting program for the rigorous Teng-Man analysis. Measured $\delta\Psi_{sp}$ and $\delta B/B$ were fitted as shown in Fig. 4.18(a). The tweaked value of γ for the ratio of r_{13} to r_{33} was ~ 0.34 to get $r_{33} = 350$ pm/V. The extinction coefficient of the NLO film is estimated to be ~ 0.01 to get the best fit. Figure 4.18(b) shows the r_{33} 's by the simple model and the rigorous model. The r_{33} 's by the rigorous model at all angles of incidence are consistent, while the ones by the simple model are not. The simple model r_{33} is 470 pm/V at a 45° angle of incidence, which is $\sim 34\%$ overestimated. The rigorous model s_{33} is estimated to be 30 pm/V.

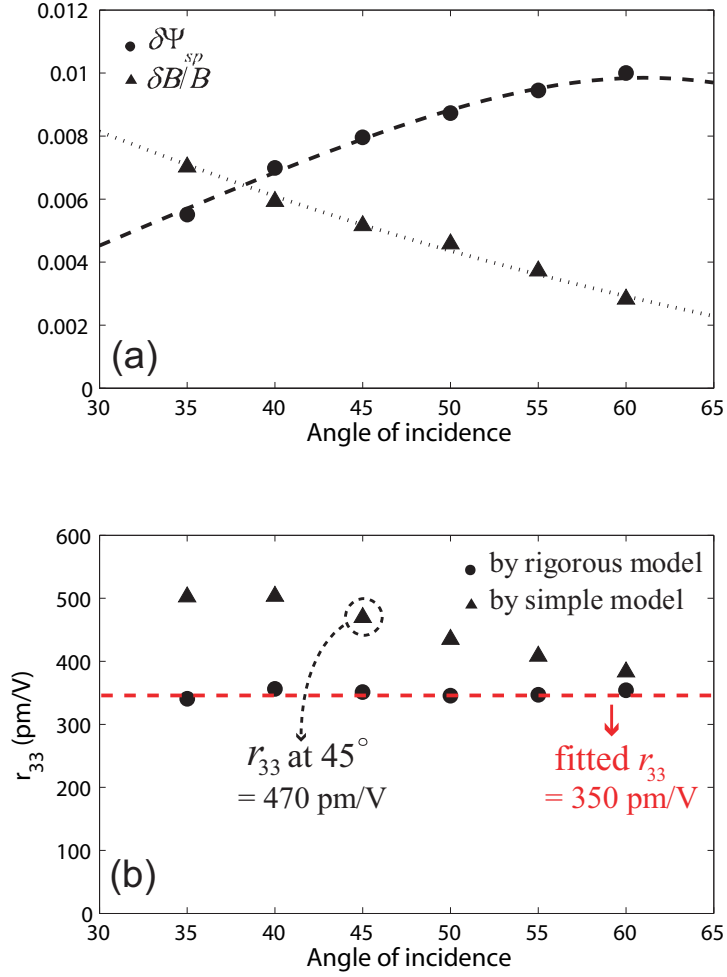


Figure 4.18: (a) Measured $\delta\Psi_{sp}$ and $\delta B/B$ versus angle of incidence. Dashed and short dash lines are numerical fit to $\delta\Psi_{sp}$ and $\delta B/B$. (b) EO coefficients r_{33} calculated by the simple model (triangle) and the rigorous model (circle) at discrete angle of incidence. The r_{33} 's by the rigorous model at each angle are well aligned with fitted r_{33} .

CONCLUSIONS

5.1 Summary

First, we have briefly reviewed the basic principles of second-order nonlinearity of poled NLO films. We have studied the relation between the chromophore orientation and second-order nonlinearity based on the oriented gas model.

Second, we have presented new mathematical expressions for analyzing Teng-Man data in both transparent and absorptive films that take into account the optical properties of the TCO layer. The formulas presented were derived using a rigorous model that includes the effect of multiple reflections inside the multilayered structure at any angle of incidence. In addition, a new expression has been derived for the electrochromic effect in the simple model. A curve fitting procedure has been described for the full profiles of angle dependent I_{dc} and I_m to extract more accurate complex EO coefficient values from the experimental data. Based on a linear least squares fitting, this method is expected to facilitate the use of a rigorous model to obtain reliable EO coefficients for poled Teng-Man samples. In order to use the rigorous model, however, it is necessary to know detailed information about the sample because simultaneously fitting multiple parameters does not give a unique fit. We have shown that the relative error from using the simple model can exhibit cyclic, asymptotic, and irregular behaviors depending on the operating wavelength as the thickness of the polymer film increases. The error extremes can be reduced

by choosing an operating wavelength where the absorption of the polymer and TCO are small simultaneously, not by decreasing the thickness of the polymer film on the order of a wavelength or less. We also note that the complex quadratic EO coefficient can be measured by detecting the signal at twice the fundamental frequency or by applying a DC offset to the polymer film with a sinusoidal bias as discussed in Ref. [55]. Our formulas can easily be modified to include these effects. We also expect that our analysis can be applied to the interferometric types of measurement to estimate the relative error introduced by the TCO layer.

In addition, we have investigated the suitability of using thick LiNbO_3 crystal to validate a Teng-Man setup for measuring EO coefficients of poled thin films. We used our new mathematical expressions for the rigorous analysis of Teng-Man data that we discussed earlier. We found that if the light reflected once through the sample is detected and other spurious reflections are blocked, thick crystals such as z -cut LiNbO_3 can be analyzed using the simple model because the thickness is large enough to avoid multiple reflections. Consequently, the EO measurement of thick z -cut LiNbO_3 can be used to verify that the Teng-Man simple model is valid, but it is not appropriate for validating thin film measurements.

Generally, if no reflections are blocked, the reflectance depends on the beam waist. Reflections from a tightly focused beam can produce an reflectance discrepancy between the plane wave analysis and Gaussian beam analysis. When the beam waist is large compared to the thickness in order to be able to apply plane wave analysis, rapid reflectance fluctuations occur with angle of incidence in the case of thick samples.

Third, we have discussed the advantages and accuracy of the ATR method for EO measurement of a poled NLO film containing a TCO layer. We have shown that the NLO film indices of refraction estimated by using the three-layer waveg-

uide model are quite reliable but the estimation of the film thickness is not. The closed-form expressions of $\partial N/\partial n$'s were presented for the three-layer waveguide model. They were used to show a large difference with $\partial N/\partial n$'s from the four-layer waveguide model. The ATR method based on the three-layer waveguide model can introduce a considerable error in r_{33} when the film has only one guided mode. So multimode films are recommended for more accurate analysis. The error can be reduced by using the four-layer waveguide model containing a TCO layer because it gives a reasonable estimate of the film indices, thickness and $\partial N/\partial n$'s. We note that the relative error in r_{33} from a single-mode film is larger than that from a multimode film and decreases asymptotically as the film thickness increases, whereas the error from the simple Teng-Man method shows a large cyclic variation. We have found that as the film is thinner and the mode used in the calculation goes higher, the assumption of the slight shift in reflectivity curve (R_{dc}) under a bias is more incorrect.

Lastly, we have presented the experimental results. The ellipsometric measurement of TCO such as ITO and ZnO was discussed for the determination of the optical properties. It is shown that a Lorentz and/or Drude model is suitable for ITO, while a Gaussian model is better for ZnO. For some cases, TCO can be difficult to characterize because the optical properties can vary widely with deposition conditions and post-deposition processing. A graded layer often satisfies these requirements. Selected poled NLO polymers were analyzed by a rigorous Teng-Man analysis and/or ATR method. We have showed that the result from the ATR method based on a multilayer structure containing a TCO layer shows good agreement with that from the rigorous Teng-Man analysis. A very high EO coefficient ($r_{33} = 350$ pm/V) has been measured for AJ-TTE-II at 1310 nm. Table 5.1 shows the summary of EO coefficients of the NLO films that we have discussed. We also

Table 5.1: Summary of EO coefficients of four NLO films and LiNbO₃ at 1310 nm.

	r_{33} (pm/V)	n_e	$n_e^3 r_{33}$ (pm/V)
AJ302	150	1.72	763
AJ404L	210	1.8	1225
AJLS102 ¹	83	1.71	415
AJ-TTE-II	350	2.2	3727
LiNbO ₃	30	2.15	298

¹AJLS102 was measured at 1550 nm.

listed the value of $n_e^3 r_{33}$ because it is a meaningful parameter in determining the change of the refractive index. Notably, the EO coefficient of AJ-TTE-II was ~ 12 times higher than the best inorganic crystal LiNbO₃.

5.2 Research directions

So far, we have focused on the measurement of the LEO effect of poled polymer thin films. Other research areas as an extension of the work presented in this thesis are discussed below.

The quadratic EO effect is one of the third-order nonlinear phenomena called DC Kerr effect, $\chi^{(3)}(-\omega; 0, 0, \omega)$. Using Teng-Man method, it can be characterized by detecting the signal at twice the fundamental frequency or by applying a DC offset to the polymer film with a sinusoidal bias. However, our formulas should be modified to include these effects. The piezoelectric effect produces useful applications such as sensors, actuators, motors and so on. When the NLO film has three or more guided modes, piezoelectric effects can be characterized using ATR method, but we have not presented an experimental result.

As we pointed out earlier, it is difficult to characterize the LEO effect from thick films ($>$ a few tens microns). The reason is that $\delta\Psi_{sp}$ fluctuates fast with increasing film thickness in Teng-Man method. In addition, the guided modes in ATR are too dense to identify each individual mode. Above all, a very high voltage supply is needed to get a measurable change of the refractive index.

A large second-order nonlinearity opens possibilities for low voltage operation in various polymer optoelectronic devices such as MZ EO modulator, phase-shifter, resonator, mode converter, and so on. In addition to large nonlinearity, NLO polymer should satisfy high intrinsic temporal stability and low optical loss etc., for device quality. There has been considerable progress in MZ EO modulator development in the last few decades, but research is still ongoing.

You don't have to be a fantastic hero to do certain things – to compete. You can be just an ordinary chap, sufficiently motivated to reach challenging goals.

- Edmund Hillary

APPENDIX A

$\delta\beta$ AND H FUNCTIONS IN TENG-MAN METHOD

A.1 Variation of the propagation constants inside the NLO film

Here, we present detailed expressions for the variation of the s - and p -wave propagation constants. From Snell's law we have

$$\tilde{n}_s \sin \tilde{\theta}_s = \tilde{n}_p \sin \tilde{\theta}_p = \sin \theta \equiv N, \quad (\text{A.1})$$

where $\tilde{n}_s = \tilde{n}_o$ and

$$\frac{1}{\tilde{n}_p^2} = \frac{\cos^2 \tilde{\theta}_p}{\tilde{n}_o^2} + \frac{\sin^2 \tilde{\theta}_p}{\tilde{n}_e^2}. \quad (\text{A.2})$$

Using N , which is of course constant at a given angle of incidence, we can write the propagation constants in the forms

$$\beta_s = k_o \sqrt{\tilde{n}_o^2 - N^2} \quad (\text{A.3})$$

and

$$\beta_p = k_o \frac{\tilde{n}_o}{\tilde{n}_e} \sqrt{\tilde{n}_e^2 - N^2}. \quad (\text{A.4})$$

An advantage of expressing the β 's in terms of N is that we do not have to explicitly deal with changes in the internal angles θ_s and θ_p as the refractive index changes - they are automatically accounted for in this representation. The variations of $\beta_{s,p}$

induced by the applied voltage are given by

$$\delta\beta_s = \frac{k_o \tilde{n}_o}{\sqrt{\tilde{n}_o^2 - N^2}} \delta\tilde{n}_o \quad (\text{A.5})$$

and

$$\delta\beta_p = \frac{k_o}{\tilde{n}_e} \sqrt{\tilde{n}_e^2 - N^2} \delta\tilde{n}_o + \frac{k_o \tilde{n}_o N^2}{\tilde{n}_e^2 \sqrt{\tilde{n}_e^2 - N^2}} \delta\tilde{n}_e. \quad (\text{A.6})$$

Outside the absorption band, we can make the approximations discussed in Section 2.2.1 to obtain

$$\delta\beta_s \approx \frac{k_o n_o}{\sqrt{n_o^2 - N^2}} (\delta n_o + i\delta\kappa_o) \quad (\text{A.7})$$

and

$$\delta\beta_p \approx \frac{k_o}{n_e} \sqrt{n_e^2 - N^2} (\delta n_o + i\delta\kappa_o) + \frac{k_o n_o N^2}{n_e^2 \sqrt{n_e^2 - N^2}} (\delta n_e + i\delta\kappa_e). \quad (\text{A.8})$$

A.2 H functions in the rigorous model

In this appendix, we derive detailed expressions for the functions H_r and H_s that appear in Eq. 2.20 and describe the linear dependence of $\delta\tilde{B}/\tilde{B}$ on r_{33} and s_{33} for the rigorous expression of reflectance. Also, because many software analysis packages can handle complex numbers efficiently, we retain the complex expressions for $\delta\tilde{n}_o$ and $\delta\tilde{n}_e$ as described in Eq. 2.1.

Performing the operations described in Eq. 2.20, we have

$$H_r = -\frac{V}{2d_4} \left[\frac{\gamma}{r_s} \frac{\partial r_s}{\partial \tilde{n}_o} \tilde{n}_o^3 + \gamma \left(\frac{1}{r_p} \frac{\partial r_p}{\partial \tilde{n}_o} \tilde{n}_o^3 \right)^* + \left(\frac{1}{r_p} \frac{\partial r_p}{\partial \tilde{n}_e} \tilde{n}_e^3 \right)^* \right] \quad (\text{A.9})$$

and

$$H_s = -\frac{V}{2d_4} \left[\frac{\gamma}{r_s} \frac{\partial r_s}{\partial \tilde{n}_o} \tilde{n}_o^3 - \gamma \left(\frac{1}{r_p} \frac{\partial r_p}{\partial \tilde{n}_o} \tilde{n}_o^3 \right)^* - \left(\frac{1}{r_p} \frac{\partial r_p}{\partial \tilde{n}_e} \tilde{n}_e^3 \right)^* \right]. \quad (\text{A.10})$$

Next, we derive detailed expressions for the derivatives in Eqs. A.9 and A.10 using the rigorous reflection coefficients r_s and r_p . Expanding Eq. 2.35, we see that

the required derivatives in Eqs. A.9 and A.10 are off the form

$$\frac{1}{r} \frac{\partial r}{\partial \tilde{n}_{o,e}} = \frac{1}{r} \frac{\partial r}{\partial \hat{r}_{34}} \left(\frac{\partial \hat{r}_{34}}{\partial r_{34}} \frac{\partial r_{34}}{\partial \tilde{n}_{o,e}} + \frac{\partial \hat{r}_{34}}{\partial \hat{r}_{45}} \frac{\partial \hat{r}_{45}}{\partial r_{45}} \frac{\partial r_{45}}{\partial \tilde{n}_{o,e}} + \frac{\partial h \hat{r}_{34}}{\partial \beta_4} \frac{\partial \beta_4}{\partial \tilde{n}_{o,e}} \right), \quad (\text{A.11})$$

where we have omitted the s, p designations to prevent the notation from becoming unduly cumbersome. The three derivatives with respect to \tilde{n}_o and \tilde{n}_e are given by

$$\frac{1}{r_s} \frac{\partial r_s}{\partial \tilde{n}_o} = \frac{f_{234}^s}{r_s} \left(g_{345}^s \frac{\partial r_{34}^s}{\partial \tilde{n}_o} + f_{345}^s g_{456}^s \frac{\partial r_{45}^s}{\partial \tilde{n}_o} + 2id_4 \hat{r}_{45}^s f_{345}^s \frac{\partial \beta_{s4}}{\partial \tilde{n}_o} \right), \quad (\text{A.12})$$

$$\frac{1}{r_p} \frac{\partial r_p}{\partial \tilde{n}_o} = \frac{f_{234}^p}{r_p} \left(g_{345}^p \frac{\partial r_{34}^p}{\partial \tilde{n}_o} + f_{345}^p g_{456}^p \frac{\partial r_{45}^p}{\partial \tilde{n}_o} + 2id_4 \hat{r}_{45}^p f_{345}^p \frac{\partial \beta_{p4}}{\partial \tilde{n}_o} \right), \quad (\text{A.13})$$

and

$$f \frac{1}{r_p} \frac{\partial r_p}{\partial \tilde{n}_e} = \frac{f_{234}^p}{r_p} \left(g_{345}^p \frac{\partial r_{34}^p}{\partial \tilde{n}_e} + f_{345}^p g_{456}^p \frac{\partial r_{45}^p}{\partial \tilde{n}_e} + 2id_4 \hat{r}_{45}^p f_{345}^p \frac{\partial \beta_{p4}}{\partial \tilde{n}_e} \right), \quad (\text{A.14})$$

where the f 's and g 's are defined by

$$f_{ijk}^q = \frac{[1 - (r_{ij}^q)^2] \exp(2i\beta_{qj}d_j)}{[1 + r_{ij}^q \hat{r}_{jk}^q \exp(2i\beta_{qj}d_j)]^2}, \quad g_{ijk}^q = \frac{[1 - (r_{jk}^q)^2] \exp(4i\beta_{qj}d_j)}{[1 + r_{ij}^q \hat{r}_{jk}^q \exp(2i\beta_{qj}d_j)]^2} \quad (\text{A.15})$$

with $q = s, p$. The remaining derivatives in Eqs. A.12-A.14 are given by

$$\frac{\partial r_{34}^s}{\partial \tilde{n}_o} = \frac{-2\tilde{n}_o Z_3^s (Z_4^s)^3}{(Z_3^s + Z_4^s)^2}, \quad \frac{\partial r_{34}^p}{\partial \tilde{n}_o} = \frac{-2Z_3^p Z_4^p}{\tilde{n}_o (Z_3^p + Z_4^p)^2}, \quad \frac{\partial r_{34}^p}{\partial \tilde{n}_e} = \frac{2Z_3^p N^2}{\tilde{n}_o^2 \tilde{n}_e^3 Z_4^p (Z_3^p + Z_4^p)^2}, \quad (\text{A.16})$$

$$\frac{\partial r_{45}^s}{\partial \tilde{n}_o} = \frac{2\tilde{n}_o (Z_4^s)^3 Z_5^s}{(Z_4^s + Z_5^s)^2}, \quad \frac{\partial r_{45}^p}{\partial \tilde{n}_o} = \frac{2Z_4^p Z_5^p}{\tilde{n}_o (Z_4^p + Z_5^p)^2}, \quad \frac{\partial r_{45}^p}{\partial \tilde{n}_e} = \frac{-2Z_5^p N^2}{\tilde{n}_o^2 \tilde{n}_e^3 Z_4^p (Z_4^p + Z_5^p)^2}, \quad (\text{A.17})$$

and

$$\frac{\partial \beta_{s4}}{\partial \tilde{n}_o} = k_o Z_4^s \tilde{n}_o, \quad \frac{\partial \beta_{p4}}{\partial \tilde{n}_o} = k_o Z_4^p \tilde{n}_o, \quad \frac{\partial \beta_{p4}}{\partial \tilde{n}_e} = k_o \frac{1}{Z_4^p} \frac{N^2}{\tilde{n}_e^3}. \quad (\text{A.18})$$

Here, the wave impedance Z 's are defined in Eq. 2.37. For writing a computer program, it is straightforward to start with the definition of the wave impedance

Z 's in Eq. 2.37 and substitute from Eq. A.18 sequentially back to Eqs. A.9 and A.10 using also the definition of the total reflection coefficients r_s and r_p from Eq. 2.35. However, it is in general unduly cumbersome to express the functions H_r and H_s in Eqs. A.9 and A.10 as explicit functions of the linear parameters (complex refractive index and thickness) of the multilayer sample structure.

APPENDIX B

ERROR ESTIMATOR

B.1 Teng-Man error estimator in MATLABTM

We present the MATLABTM codes for the estimate of error from the simple Teng-Man method as defined in Eq. 2.47. These include 7 functions and 1 main code as an example. The main code allows you to handle a Teng-Man sample containing buffer layers at both sides of the thin film.

TE reflectance at single layer

```
% function for reflectance of s-polarized light at two different medium
% out=rs(n1,n2,N)
% n1, n2 : ordinary refractive indices at medium 1 and 2
% N : index*sine of angle of incidence
function out=rs(n1,n2,N)
out=(1/sqrt(n2^2-N^2)-1/sqrt(n1^2-N^2))/(1/sqrt(n2^2-N^2)+1/sqrt(n1^2-N^2));
```

TM reflectance at single layer

```
% function for reflectance of p-polarized light at two different medium
% out=rp(n1o,n1e,n2o,n2e,N)
% n1o, n1e : ordinary and extraordinary refractive indices at medium 1
% n2o, n2e : ordinary and extraordinary refractive indices at medium 2
function out=rp(n1o,n1e,n2o,n2e,N)
out=(sqrt(1-(N/n2e)^2)/n2o-sqrt(1-(N/n1e)^2)/n1o)/(sqrt(1-(N/n2e)^2)
/n2o+sqrt(1-(N/n1e)^2)/n1o);
```

TE reflectance at multilayer

```
% function for reflectance of s-polarized light at multilayered medium
% nd is the matrix containing index and thickness information
% if it has 8 layers,
% nd=[ no1, ne1, 0; no2, ne2, d2; ... ; no6, ne6, d6; ... ;no8, ne8, 0];
%      ..>ordinary index @ 2 layer ..> thickness of 6 layer
% no, ne : ordinary and extraordinary refractive indices
% d : thickness (micrometer)
```

```

% wl : wavelength (micrometer)
% N : index*sine of angle of incidence
function out=rsm(nd,wl,N)
row=size(nd,1);
in=row-1;
y=rs(nd(in,1),nd(in+1,1),N);
for in=row-2:-1:1
    x=rs(nd(in,1),nd(in+1,1),N);
    z=exp(2i*bs(wl,nd(in+1,1),N)*nd(in+1,3));
    y=(x+y*z)./(1+x*y*z);
end;
out=y;

```

TM reflectance at multilayer

```

% function for reflectance of p-polarized light at multilayered medium
% function out=rpm(nd,wl,N)
% nd is the matrix containing index and thickness information
% if it has 8 layers,
% nd=[ no1, ne1, 0; no2, ne2, d2; ... ; no6, ne6, d6; ... ;no8, ne8, 0];
%           :..>ordinary index @ 2 layer :..> thickness of 6 layer
% parameters as defined in rsm
function out=rpm(nd,wl,N)
row=size(nd,1);
in=row-1;
y=rp(nd(in,1),nd(in,2),nd(in+1,1),nd(in+1,2),N);
for in=row-2:-1:1
    x=rp(nd(in,1),nd(in,2),nd(in+1,1),nd(in+1,2),N);
    z=exp(2i*bp(wl,nd(in+1,1),nd(in+1,2),N)*nd(in+1,3));
    y=(x+y*z)/(1+x*y*z);
end
out=y;

```

TE propagation constant

```

% function for propagation constant of s wave
% out=bs(wl,n,N)
% n : ordinary refractive index
function out=bs(wl,n,N)
out=2*pi*sqrt(n^2-N^2)/wl;

```

TM propagation constant

```

% function for propagation constant of p wave
% out=bp(wl,no,ne,N)
% no, ne : ordinary and extraordinary refractive indices
function out=bp(wl,no,ne,N)
out=2*pi*no*sqrt(1-(N/ne)^2)/wl;

```

Error from the simple Teng-Man model

```

% function to find error of r33 from simple model
% in multilayered structure with buffer.
% function out=error(nd,wl,N,r33,s33,a)
% input argument
% nd : index and thickness matrix
% wl : wavelength (micron)
% N : sine of incident angle
% a : r13/r33
function out=error_r33(nd,wl,N,r33,s33,a)
r13=a*r33;
s13=a*s33;
V=1; % applied peak voltage

dno=-0.5*nd(4,1)^3*(r13+i*s13)*V/nd(4,3);
dne=-0.5*nd(4,2)^3*(r33+i*s33)*V/nd(4,3);
nd_V=nd+[0,0,0;0,0,0;0,0,0;dno,dne,0;0,0,0;0,0,0;0,0,0];

Bt=rsm(nd,wl,N)*conj(rpm(nd,wl,N)); % B
dBt=rsm(nd_V,wl,N)*conj(rpm(nd_V,wl,N)); % dB
dBt_Bt=dBt/Bt; % dB/B

no=real(nd(4,1)); ne=real(nd(4,2));

% simple model EO coefficient
r33SM=wl*imag(dBt_Bt)/2/pi/V/(no*ne*N^2/sqrt(ne^2-N^2)+a*(no^3*sqrt(ne^2-N^2)
/ne-no^4/sqrt(no^2-N^2)));
out=(r33SM/r33 - 1)*100;

Main

% main code
clear all;
% Decide nFlag value to get the graph you want
% nFlag =1 : Plot error(%) vs. film layer
% nFlag =2 : Plot error(%) vs. buffer1 layer
% nFlag =3 : Plot error(%) vs. buffer2 layer
nFlag=input('Input nFlag number (1, 2, or 3) :');

% Specify indices and thicknesses at each layer
% [glass/TCO/buffer1/NLO film/buffer2/gold/air]
n2=1.5; % glass
n3=1.26+0.12i; d3=0.045; % TCO
n4=2.4; n4e=2.5; d4=0.1; % buffer1
n5o=1.7; d5=2; n5e=1.7; % NLO film
n6=1.5; n6e=1.5; d6=0; % buffer2
n7=0.42+8.12i; d7=0.1; % Au electrode
N=sin(45*pi/180); % sine of angle of incidence
wl=1.319; % wavelength (um)
r33=100e-6; % r33 (10^-6 m/V)
s33=0; % s33 (10^-6 m/V)
a=1/3; % ratio of r13 to r33

nd=[n2,n2,0;n3,n3,d3;n4,n4e,d4;n5o,n5e,d5;n6,n6e,d6;n7,n7,d7;1,1,0];

```

```

xd=0.5:0.01:3;
for xi=1:length(xd)
    if nFlag == 1
        nd(4,3)=xd(xi);
    elseif nFlag == 2
        nd(3,3)=xd(xi);
    elseif nFlag == 3
        nd(5,3)=xd(xi);
    end;
    % Error between simple model r33 and correct r33
    Err(xi)=error_r33(nd,wl,N,r33,s33,a);
end;

plot(xd,Err,'r-');
if nFlag == 1
    xlabel 'polymer thickness (\mum)';
elseif nFlag == 2
    xlabel 'buffer1 thickness (\mum)';
elseif nFlag == 3
    xlabel 'buffer2 thickness (\mum)';
end;
ylabel 'Error (%)';

```

B.2 Java Teng-Man error estimator

We have developed a stand-alone program¹ for the estimation of error resulting from the simple Teng-Man method in Java language to offer convenience to those who wish to estimate the error without any dependency on commercial numerical software such as MATLABTM and Mathematica. In addition, it runs on any OS (Operating System) as long as JVM² (Java Virtual Machine) is installed. This is simply conversion of MATLABTM codes to Java application. It allows inclusion of buffer layers between both TCO/film and film/electrode layers in the multilayer structure.

This was developed under Netbeans IDE³ (Integrated Development Environment) and used a free Java chart library called JFreechart⁴ for the GUI (Graphical User Interface).

¹For a free copy, email park.donghun@gmail.com or herman@lps.umd.edu.

²<http://www.java.com/>

³<http://www.netbeans.org/>

⁴<http://www.jfree.org/jfreechart/>

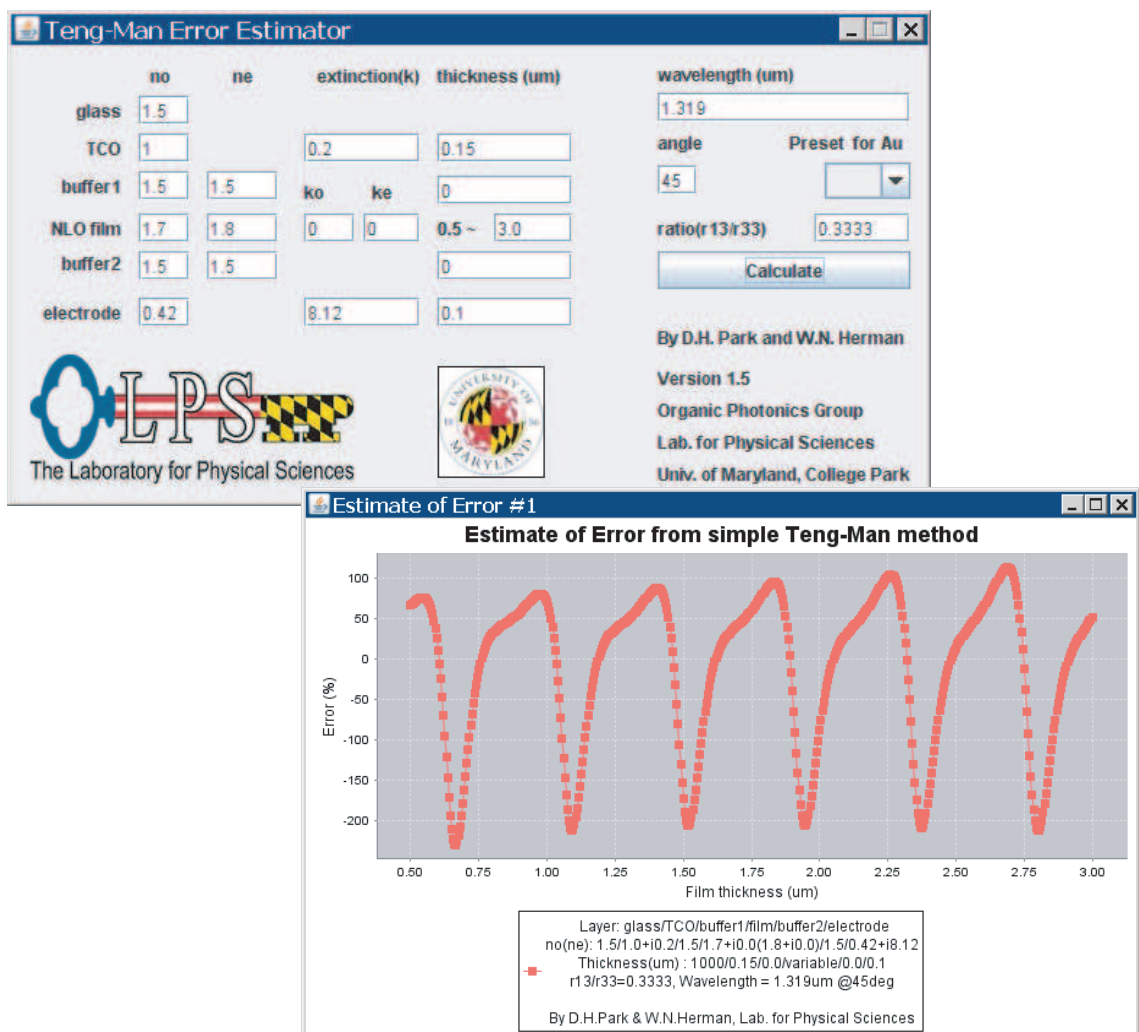


Figure B.1: Snap shot of Java Teng-Man error estimator.

Bibliography

- [1] G. A. Lindsay and K. D. Singer, Eds., *Polymers for Second-Order Nonlinear Optics*, acs symposium series 601 ed., 1995.
- [2] D. S. Chemla and J. Zyss, *Nonlinear optical properties of organic molecules and crystals*. Academic Press, 1987.
- [3] P. Prasad and D. Williams, *Nonlinear optical effects in molecules and polymers*. John Wiley and Sons, 1991.
- [4] F. Kajzar, K.-S. Lee, and A. K.-Y. Jen, "Polymeric materials and their orientation techniques for second-order nonlinear optics," *Advances in Polymer Science*, vol. 161, pp. 1–85, 2003.
- [5] T.-D. Kim, J.-W. Kang, J. Luo, S.-H. Jang, J.-W. Ka, N. Tucker, J. B. Benedict, L. R. Dalton, T. Gray, R. M. Overney, D. H. Park, W. N. Herman, and A. K.-Y. Jen, "Ultralarge and thermally stable electro-optic activities from supramolecular self-assembled molecular glasses," *Journal of American Chemical Society*, vol. 129, pp. 488 – 489, 2007.
- [6] M. Lee, H. E. Katz, C. Erben, D. M. Gill, P. Gopalan, J. D. Heber, and D. J. McGee, "Broadband modulation of light by using an electro-optic polymer," *Science*, vol. 298, pp. 1401–1403, 2002.
- [7] Y. Enami, C. T. DeRose, C. Loychik, D. Mathine, R. A. Norwood, J. Luo, A. K. Y. Jen, and N. Peyghambarian, "Low half-wave voltage and high electro-optic effect in hybrid polymer/sol-gel waveguide modulators," *Applied Physics Letters*, vol. 89, no. 14, p. 143506, 2006.
- [8] Y. Kim, "Novel organic polymeric and molecular thin-film devices for photonic applications," Ph.D. dissertation, University of Maryland, College Park, 2006.

- [9] L. Eldada and L. W. Shacklette, “Advances in polymer integrated optics,” *IEEE Journal of Selected Topics in Quantum Electronics*, vol. 6, pp. 54–68, 2000.
- [10] H. Ma, A. K.-Y. Jen, and L. Dalton, “Polymer-based optical waveguides: Materials, processing, and devices,” *Advanced Materials*, vol. 14, no. 19, pp. 1339–1365, 2002.
- [11] L. Dalton, “Nonlinear optical polymeric materials: From chromophore design to commercial applications,” *Advances in Polymer Science*, vol. 158, pp. 1–86, 2002.
- [12] G. R. Meredith, J. G. VanDusen, and D. J. Williams, “Optical and nonlinear optical characterization of molecularly doped thermotropic liquid crystalline polymers,” *Macromolecules*, vol. 15, pp. 1385–1389, 1982.
- [13] C. C. Teng and H. T. Man, “Simple reflection technique for measuring the electro-optic coefficient of poled polymers,” *Applied Physics Letters*, vol. 56, pp. 1734–1736, 1990.
- [14] J. S. Schildkraut, “Determination of the electro optic coefficient of a poled polymer film,” *Applied Optics*, vol. 29, pp. 2839–2841, 1990.
- [15] F. Michelotti, A. Belardini, M. C. Larciprete, M. Bertolotti, A. Rousseau, A. Ratsimihety, G. Schoer, and J. Mueller, “Measurement of the electro-optic properties of poled polymers at $\lambda = 1.55 \mu\text{m}$ by means of sandwich structures with zinc oxide transparent electrode,” *Applied Physics Letters*, vol. 83, pp. 4477–4479, 2003.
- [16] Y. Levy, M. Dumont, E. Chastaing, P. Robin, P.-A. Chollet, G. Gadret, and F. Kajzar, “Reflection method for electro-optical coefficient determination in

- stratified thin film structures,” *Molecular Crystals and Liquid Crystals Science and Technology Section B: Nonlinear Optics*, vol. 4, pp. 1–19, 1993.
- [17] P.-A. Chollet, G. Gadret, F. Kajzar, and P. Raimond, “Electro-optic coefficient determination in stratified organized molecular thin films: application to poled polymers,” *Thin Solid Films*, vol. 242, pp. 132–138, 1994.
- [18] Y. Shuto and M. Amano, “Reflection measurement technique of electro-optic coefficients in lithium niobate crystals and poled polymer films,” *Journal of Applied Physics*, vol. 77, pp. 4632–4638, 1995.
- [19] P. N. Butcher and D. Cotter, *The Elements of Nonlinear Optics*. Cambridge University Press, 1991.
- [20] R. W. Boyd, *Nonlinear Optics*. Academic Press, 2003.
- [21] I. P. Kaminow, *An Introduction to Electrooptic Devices*. Academic Press, Inc, 1974.
- [22] C. A. Eldering, A. Knoesen, and S. T. Kowel, “Use of Fabry-Perot devices for the characterization of polymeric electro-optic films,” *Journal of Applied Physics*, vol. 69, no. 6, pp. 3676–3686, 1991.
- [23] K. D. Singer, M. G. Kuzyk, and J. E. Sohn, “Second-order nonlinear-optical processes in orientationally ordered materials: relationship between molecular and macroscopic properties,” *Journal of Optical Society of America, B*, vol. 4, pp. 968–976, 1987.
- [24] A. W. Harper, S. Sun, L. R. Dalton, S. M. Garner, A. Chen, S. Kalluri, W. H. Steier, and B. H. Roinson, “Translating microscopic optical nonlinearity into macroscopic optical nonlinearity: the role of chromophore-chromophore elec-

- trostatic interactions,” *Journal of Optical Society of America, B*, vol. 15, no. 1, pp. 329–337, 1998.
- [25] C. P. J. M. van der Vorst and S. J. Picken, “Electric field poling of acceptor-donor molecules,” *Journal of the Optical Society of America B*, vol. 7, no. 3, p. 320, 1990.
- [26] F. Ghebremichael, M. G. Kuzyk, and H. S. Lackritz, “Nonlinear optics and polymer physics,” *Progress in Polymer Science*, vol. 22, p. 1147, 1997.
- [27] J. W. Wu, “Birefringent and electro-optic effects in poled polymer films: steady-state and transient properties,” *Journal of the Optical Society of America B*, vol. 8, no. 1, p. 142, 1991.
- [28] D. J. Williams, “Organic polymeric and non-polymeric materials with large optical nonlinearities,” *Angewandte Chemie International Edition*, vol. 23, no. 9, pp. 690–703, 1984.
- [29] F. Ghebremichael, M. G. Kuzyk, K. D. Singer, and J. H. Andrews, “Relationship between the second-order microscopic and macroscopic nonlinear optical susceptibilities of poled dye-doped polymers,” *Journal of the Optical Society of America B*, vol. 15, no. 8, p. 2294, 1998.
- [30] S. Bauer, “Poled polymers for sensors and photonic applications,” *Journal of Applied Physics*, vol. 80, pp. 5531–5558, 1996.
- [31] D. M. Burland, R. D. Miller, and C. A. Walsh, “Second-order nonlinearity in poled-polymer systems,” *Chemical Reviews*, vol. 94, pp. 31–75, 1994.
- [32] S. Yilmaz, S. Bauer, and R. Gerhard-Multhaupt, “Photothermal poling of nonlinear optical polymer films,” *Applied Physics Letters*, vol. 64, no. 21, p. 2770, 1994.

- [33] B. Gross, R. Gerhard-Multhaupt, A. Berraisoul, and G. M. Sessler, "Electron-beam poling of piezoelectric polymer electrets," *Journal of Applied Physics*, vol. 62, no. 4, p. 1429, 1987.
- [34] H.-C. Song, M.-C. Oh, S.-W. Ahn, W. H. Steier, H. R. Fetterman, and C. Zhang, "Flexible low-voltage electro-optic polymer modulators," *Applied Physics Letters*, vol. 82, no. 25, p. 4432, 2003.
- [35] A. Chen, V. Chuyanov, H. Zhang, S. Garner, S.-S. Lee, W. H. Steier, J. Chen, F. Wang, J. Zhu, M. He, Y. Ra, S. S. H. Mao, A. W. Harper, L. R. Dalton, and H. R. Fetterman, "DC biased electro-optic polymer waveguide modulators with low half-wave voltage and high thermal stability," *Optical Engineering*, vol. 38, no. 12, p. 2000, 1999.
- [36] R. Song, A. Yick, and W. H. Steier, "Conductivity-dependency-free in-plane poling for Mach-Zehnder modulator with highly conductive electro-optic polymer," *Applied Physics Letters*, vol. 90, no. 19, p. 191103, 2007.
- [37] J. J. Ju, J. Kim, J. Y. Do, M.-s. Kim, S. K. Park, S. Park, and M.-H. Lee, "Second-harmonic generation in periodically poled nonlinear polymer waveguides," *Optics Letters*, vol. 29, no. 1, p. 89, 2004.
- [38] M.-C. Oh, S.-S. Lee, and S.-Y. Shin, "Simulation of polarization converter formed by poling-induced polymer waveguides," *Quantum Electronics, IEEE Journal of*, vol. 31, no. 9, p. 1698, 1995, 0018-9197.
- [39] V. Van, W. N. Herman, and P.-T. Ho, "Linearized microring-loaded Mach-Zehnder modulator with RF gain," *Journal of Lightwave Technology*, vol. 24, no. 4, p. 1850, 2006.
- [40] B. E. A. Saleh and M. C. Teich, *Fundamentals of Photonics*. John Wiley and Sons, Inc, 1991.

- [41] Y. Shi, C. Zhang, H. Zhang, J. H. Bechtel, L. R. Dalton, B. H. Robinson, and W. H. Steier, “Low (sub-1-volt) halfwave voltage polymeric electro-optic modulators achieved by controlling chromophore shape,” *Science*, vol. 288, no. 5463, pp. 119–122, 2000.
- [42] R. A. Norwood, M. G. Kuzyk, and R. A. Keosian, “Electro-optic tensor ratio determination of side-chain copolymers with electro-optic interferometry,” *Journal of Applied Physics*, vol. 75, pp. 1869–1874, 1994.
- [43] Y.-P. Wang, J.-P. Chen, X.-W. Li, J.-X. Hong, X.-H. Zhang, J.-H. Zhou, and A.-L. Ye, “Measuring eletro-optic coefficients of poled polymers using fiber-optic Mach-Zehnder interferometer,” *Applied Physics Letters*, vol. 85, pp. 5102–5103, 2004.
- [44] M. J. Shin, H. R. Cho, S. H. Han, and J. W. Wu, “Analysis of Mach-Zehnder interferometry measurement of the pockels coefficients in a poled polymer film with a reflection configuration,” *Journal of Applied Physics*, vol. 83, pp. 1848–1853, 1998.
- [45] H. Uchiki and T. Kobayashi, “New determination method of electro-optic constants and relevant nonlinear susceptibilities and its application to doped polymer,” *Journal of Applied Physics*, vol. 64, pp. 2625–2629, 1988.
- [46] S. Herminghaus, B. A. Smith, and J. D. Swalen, “Electro-optic coefficients in electric-field-poled polymer waveguides,” *Journal of Optical Society of America, B*, vol. 8, pp. 2311–2317, 1991.
- [47] D. Morichre, P.-A. Chollet, W. Fleming, M. Jurich, B. A. Smith, and J. D. Swalen, “Electro-optic effects in two tolane side-chain nonlinear-optical polymers: comparison between measured coefficients and second-harmonic generation,” *Journal of Optical Society of America, B*, vol. 10, pp. 1894–1900, 1993.

- [48] A. Chen, V. Chuyanov, S. Garner, W. H. Steier, and L. R. Dalton, “Modified attenuated total reflection for the fast and routine electro-optic measurement of nonlinear optical polymer thin films,” *Organic Thin Films for Photonics Applications, OSA meeting*, vol. 14, pp. 158–160, 1997.
- [49] Y. Jiang, Z. Cao, Q. Shen, X. Dou, Y. Chen, and Y. Ozaki, “Improved attenuated-total-reflection technique for measuring the electro-optic coefficients of nonlinear optical polymers,” *Journal of the Optical Society of America B*, vol. 17, no. 5, p. 805, 2000.
- [50] W. H. G. Horsthuis and G. J. M. Krijnen, “Simple measuring method for electro-optic coefficients in poled polymer waveguides,” *Applied Physics Letters*, vol. 55, no. 7, p. 616, 1989.
- [51] L. M. Hayden, G. F. Sauter, F. R. Ore, P. L. Pasillas, J. M. Hoover, G. A. Lindsay, and R. A. Henry, “Second-order nonlinear optical measurements in guest-host and side-chain polymers,” vol. 68, pp. 456–465, 1990.
- [52] S. Kalluri, S. Garner, M. Ziari, W. H. Steier, Y. Shi, and L. R. Dalton, “Simple two-slit interference electro-optic coefficients measurement technique and efficient coplanar electrode poling of polymer thin films,” *Applied Physics Letters*, vol. 69, pp. 275–277, 1996.
- [53] K. Clays and J. S. Schildkraut, “Dispersion of the complex electro-optic coefficient and electrochromic effects in poled polymer films,” *Journal of Optical Society of America, B*, vol. 9, pp. 2274–2282, 1992.
- [54] P. M. Lundquist, M. Jurich, J.-F. Wang, H. Zhou, T. J. Marks, and G. K. Wong, “Electro-optic characterization of poled-polymer films in transmission,” *Applied Physics Letters*, vol. 69, pp. 901–903, 1996.

- [55] F. Michelotti, G. Nicolao, F. Tesi, and M. Bertolotti, “On the measurement of the electro-optic properties of poled side-chain copolymer films with a modified Teng-Man technique,” *Chemical Physics*, vol. 245, pp. 311–325, 1999.
- [56] L. Wang, Y. Yang, T. J. Marks, Z. Liu, and S.-T. Ho, “Near-infrared transparent electrodes for precision Teng-Man electro-optic measurements: In_2O_3 thin-film electrodes with tunable near-infrared transparency,” *Applied Physics Letters*, vol. 87, pp. 161107–1–3, 2005.
- [57] G. Khanarian, J. Sounik, D. Allen, S. F. Shu, C. Walton, H. Goldberg, and J. B. Stamatoff, “Electro-optic characterization of nonlinear-optical guest-host films and polymers,” *Journal of Optical Society of America, B*, vol. 13, pp. 1927–1934, 1996.
- [58] S. H. Han and J. W. Wu, “Single-beam polarization interferometry measurement of the linear electro-optic effect in poled polymer films with a reflection configuration,” *Journal of Optical Society of America, B*, vol. 14, pp. 1131–1137, 1997.
- [59] F. Wang, E. Furman, and G. Haertling, “Electro-optic measurements of thin-film materials by means of reflection differential ellipsometry,” *Journal of Applied Physics*, vol. 78, pp. 9–15, 1995.
- [60] D. Guo, R. Lin, and W. Wang, “Gaussian-optics-based optical modeling and characterization of a Fabry-Perot microcavity for sensing applications,” *Journal of Optical Society of America, A*, vol. 22, pp. 1577–1588, 2005.
- [61] M. Born and E. Wolf, *Principles of Optics*, 7th ed. Cambridge University Press, 1999.
- [62] S. Ramo, J. R. Whinnery, and T. V. Duzer, *Fields and Waves in Communication Electronics*. John Wiley and Sons, 1965.

- [63] M. T. Heath, *Scientific Computing*, 2nd ed. McGraw Hill, 2002.
- [64] R. A. Synowicki, "Spectroscopic ellipsometry characterization of indium tin oxide film microstructure and optical constants," *Thin Solid Films*, vol. 313-314, pp. 394–397, 1998.
- [65] A. M. Sinyukov and L. M. Hayden, "Generation and detection of terahertz radiation with multilayered electro-optic polymer films," *Optics Letters*, vol. 27, no. 1, p. 55, 2002.
- [66] D. H. Park, C. H. Lee, and W. N. Herman, "Suitability of using thick LiNbO₃ to validate reflection method electro-optic measurements of thin films," *Organic Thin Film Symposium, ACS National Meeting*, 2006.
- [67] S. D. Smith, "Design of multilayer filters by considering two effective interfaces," *Journal of Optical Society of America*, vol. 48, no. 1, pp. 43–50, 1958.
- [68] P. Yeh, *Optical Waves in Layered Media*. John Wiley and Sons, 1988.
- [69] D. Marcuse, *Theory of Dielectric Optical Waveguides*, 2nd ed. Academic Press, Inc, 1991.
- [70] C. Pollock and M. Lipson, *Integrated Photonics*, 1st ed. Springer, 2003.
- [71] Y. Uematsu, T. Ozeki, and Y. Unno, "Efficient power coupling between an MH LED and a taper-ended multimode fiber," *Quantum Electronics, IEEE Journal of*, vol. 15, no. 2, p. 86, 1979.
- [72] Y. Leng, V. Yun, G. Hutchinson, M. Du, C. H. Lee, W. N. Herman, and J. Goldhar, "Direct laser fabrication of optical polymer waveguides and bragg grating couplers," *Organic Thin Film Symposium, OSA Annual Meeting*, vol. MT114, 2003.

- [73] Y. Leng, V. Yun, L. Lucas, W. N. Herman, and J. Goldhar, “Dispensed polymer waveguides and laser-fabricated couplers for optical interconnects on printed circuit boards,” *Applied Optics*, vol. 46, no. 4, p. 602, 2007.
- [74] P. K. Tien and R. Ulrich, “Theory of prism-film coupler and thin-film light guides,” *Journal of the Optical Society of America*, vol. 60, no. 10, p. 1325, 1970.
- [75] P. K. Tien, “Light waves in thin films and integrated optics,” *Applied Optics*, vol. 10, pp. 2395–2413, 1971.
- [76] R. Ulrich and R. Torge, “Measurement of thin film parameters with a prism coupler,” *Applied Optics*, vol. 12, pp. 2901–2908, 1973.
- [77] V. Dentan, Y. Levy, M. Dumont, P. Robin, and E. Chastaing, “Electrooptic properties of a ferroelectric polymer studied by attenuated total reflection,” *Optics Communications*, vol. 69, pp. 379–383, 1989.
- [78] D. H. Park, C. H. Lee, and W. N. Herman, “Accuracy of the ATR method for electro-optic measurement of poled polymer thin films in multilayer structures,” *Organic Thin Film Symposium, OSA National Meeting*, 2007.
- [79] A. Yariv, *Quantum Electronics*, 3rd ed. John Wiley and Sons, 1988.
- [80] D. H. Park, J. W. Kang, J. D. Luo, T. D. Kim, A. K.-Y. Jen, C. H. Lee, and W. N. Herman, “Nonlinear ellipsometric analysis of poled organic glasses having very large electro-optic coefficients,” *SPIE*, vol. 5935, 2005.
- [81] D. H. Park, C. H. Lee, W. N. Herman, J. W. Kang, J. D. Luo, T. D. Kim, and A. K.-Y. Jen, “Nonlinear ellipsometric analysis of the electro-optic effect in poled organic glasses,” *Frontiers in Optics*, 2005.

- [82] D. H. Park, C. H. Lee, and W. N. Herman, “Analysis of multiple reflection effects in reflective measurements of electro-optic coefficients of poled polymers in multilayer structures,” *Optics Express*, vol. 14, pp. 8866–8884, 2006.
- [83] G. P. Crawford, *Chapter 5, Flexible Flat Panel Displays*. John Wiley and Sons, 2005.
- [84] P. P. Edwards, A. Porch, M. O. Jones, D. Morgan, and R. M. Perks, “Basic materials physics of transparent conducting oxides,” *Dalton Transactions*, pp. 2995–3002, 2004.
- [85] P. Y. Yu and M. Cardona, *Fundamentals of Semiconductors*, 3rd ed. Springer, 2001.
- [86] C. Kittel, *Introduction to Solid State Physics*, 7th ed. John Wiley and Sons, 1996.
- [87] *WVASE32[®] Manual*. J. A. Woollam, Inc.
- [88] P. B. Johnson and R. W. Christy, “Optical constants of the noble metals,” *Physical Review B*, vol. 6, pp. 4370–4379, 1972.
- [89] M. A. Ordal, L. L. Long, R. J. Bell, S. E. Bell, R. R. Bell, J. Alexander, R. W., and C. A. Ward, “Optical properties of the metals Al, Co, Cu, Au, Fe, Pb, Ni, Pd, Pt, Ag, Ti, and W in the infrared and far infrared,” *Applied Optics*, vol. 22, pp. 1099–1119, 1983.
- [90] A. D. Rakic, A. B. Djurisic, J. M. Elazar, and M. L. Majewski, “Optical properties of metallic films for vertical-cavity optoelectronic devices,” *Applied Optics*, vol. 37, pp. 5271–5283, 1998.